INSTITUTO SUPERIOR DE ENGENHARIA DE LISBOA

Departamento de Engenharia Mecânica

Technical analysis of an electrolyzer coupled with high concentration photovoltaic solar system

IVO GONÇALO DA SILVA PINA
(Licenciado em Engenharia Mecânica)

Dissertação para obtenção do grau de Mestre em Engenharia Mecânica

Orientadores:
Doutor Nelson Pereira Caetano Marques
Doutor Luis Filipe Rodrigues Castanheira

Júri:
Presidente: Doutor Gonçalo Nuno de Oliveira Duarte
Vogais:
Doutor Diogo Miguel Franco dos Santos
Doutor Luis Filipe Rodrigues Castanheira
Doutor Jorge Filipe Oliveira de Mendonça e Costa

Janeiro de 2024

INSTITUTO SUPERIOR DE ENGENHARIA DE LISBOA

Departamento de Engenharia Mecânica

Technical analysis of an electrolyzer coupled with high concentration photovoltaic solar system

IVO GONÇALO DA SILVA PINA
(Licenciado em Engenharia Mecânica)

Dissertação para obtenção do grau de Mestre em Engenharia Mecânica

Orientadores:
Doutor Nelson Pereira Caetano Marques
Doutor Luis Filipe Rodrigues Castanheira

Júri:
Presidente: Doutor Gonçalo Nuno de Oliveira Duarte
Vogais:
Doutor Diogo Miguel Franco dos Santos
Doutor Luis Filipe Rodrigues Castanheira
Doutor Jorge Filipe Oliveira de Mendonça e Costa

Janeiro de 2024

Acknowledgment

I would like to express my sincere gratitude to all the people who made this final master's thesis possible.

Firstly, my profound thanks to Professor Nelson Marques for providing me with this unique opportunity to intern in such an innovative company, with a topic of great scientific importance. I will be eternally grateful to him for trusting in me, for all the teachings provided at every stage of thesis development, as well as for all the dedication and support given from the first to the last day.

To the company that welcomed me, I appreciate the trust placed in me to achieve the proposed objectives, and I am grateful for having met so many fantastic people from whom I learned a lot. A very special thanks to the electrochemical team: Ana Priscila Ferreira, Marcela Reyes, and Luis Castanheira, who lived with me the day-to-day of this scientific work and played a predominant role in the thesis, being my main source of knowledge. Without them, this work would not have been possible.

A particular thanks to Luis Castanheira for all the dedication and attention he devoted to this project, and for all the teachings he provided. I am deeply grateful for all the support and opportunities given, and it was his vision and structured analysis that allowed this project to reach its maximum potential.

I want to thank my almost doctor girlfriend for all the patience she had to accompany me on this tumultuous journey of writing the thesis, as well as for helping me overcome the obstacles that appeared along the way.

A heartfelt thanks to my mother and sister who were forced to witness closely all the phases of my life. To them, as well as to Dornelas and my nomadic cousin, warm thanks for being a family that is consistently there during the most crucial moments.

I would also like to thank all the professors at ISEL whom I had the fortune to meet during these 5 years of study. It was truly an institution that helped me immensely, and I would like to extend a special thanks to professors Alda Carvalho, Gonçalo Duarte, and Cláudia Casaca for the opportunities they provided me and for the essential help they gave to my academic and personal growth.

Abstract

This final master's thesis emerges from the need to understand and study an electrolyzer coupled with a high-concentration photovoltaic solar system, designed, and produced by a Portuguese company. This innovative electrolyzer allows the electrochemical process of water electrolysis, in which water molecules are decomposed into hydrogen in the cathodic chamber and oxygen in the anodic chamber. To achieve the proposed objective, various in-situ instrumentation techniques were applied to the electrolyzer, along with CFD simulations of the flow-field, which is responsible for the homogenous distribution of water within the electrolyzer.

The thesis is primarily divided into five chapters. The first chapter introduces the technology to establish a general understanding of how the electrolyzer operates and its relationship with adjacent systems. The second chapter encompasses all documentation related to in-situ electrochemical instrumentation, describing the methodologies and precautions taken, as well as presenting and discussing the results obtained. The third chapter outlines the methodologies, results, and discussions related to in-situ instrumentation of the electrolyzer using thermocouple insertion techniques within the anodic chamber of the electrolyzer for temperature profile characterization in each electrochemical cell. In the fourth chapter, the methodologies followed for the CFD simulation of the electrolyzer's anodic flow-field are described, along with the presentation and discussion of the results. In the fifth and final chapter, a comprehensive conclusion is presented regarding the significance of this work in enhancing the understanding of this innovative electrolyzer. The overall objectives of this work have been successfully achieved, as it has produced results that allow for a better understanding of the electrolyzer operation and identify areas where the performance can be enhanced.

Keywords

Green Hydrogen; PEM Electrolyzer; Electrochemical In-Situ Instrumentation; Temperature In-Situ Instrumentation; CFD Water distribution geometry

Resumo

Este trabalho final de mestrado surge de a necessidade compreender e estudar um eletrolisador acoplado a um sistema solar fotovoltaico de alta concentração, desenhado e produzido por uma empresa portuguesa especializada em produção de hidrogénio verde. Através deste eletrolisador inovador é possível realizar o processo eletroquímico de eletrólise, no qual a molécula de água é decomposta em hidrogénio na câmara catódica e oxigénio na câmara anódica. Para realizar o objetivo proposto foram aplicadas diferentes técnicas de instrumentações in-situ do eletrolisador e simulação CFD do componente responsável pela distribuição homogénea da água do eletrolisador. O trabalho está essencialmente dividido em cinco capítulos. O primeiro capítulo introduz a tecnologia inerente para estabelecer uma compreensão geral de como o eletrolisador funciona e da relação com todos os sistemas adjacentes. O segundo capítulo abrange toda a documentação relacionada à instrumentação eletroquímica in-situ realizada, descrevendo as metodologias e precauções tomadas, bem como é apresentado e discutido os resultados obtidos. O terceiro capítulo apresenta as metodologias, resultados e discussões relacionadas com a instrumentação in-situ do eletrolisador criada utilizando técnicas de inserção de termopares dentro da câmara anódica do eletrolisador de forma a ser possível caracterizar os perfis de temperatura em cada uma das células eletroquímica. No quarto capítulo, são descritas as metodologias definidas e criadas para a simulação CFD flow-field anódico do eletrolisador, juntamente com a apresentação e discussão dos resultados. No quinto e último capítulo, é apresentada uma conclusão abrangente sobre a importância deste trabalho em aprimorar a compreensão deste eletrolisador inovador. Os objetivos do trabalho foram alcançados com sucesso, pois foi possível compreender melhor, e mais profundamente, o funcionamento do eletrolisador e, consequentemente, identificaram-se diversas áreas de melhoraria para um aumento do seu desempenho.

Palavras-chave

Hidrogénio Verde; Eletrolisador PEM; Instrumentação Eletroquímica in-situ; Instrumentação Temperatura in-situ; CFD distribuição da água

Resumo estendido

A consciencialização sobre o aquecimento global e a disponibilidade finita de recursos não renováveis tem levado a uma crescente preocupação global por fontes de energia mais limpas e sustentáveis. O hidrogénio tem um futuro muito promissor, e é essencial que as tecnologias de produção de hidrogénio verde se concentrem na pesquisa e no desenvolvimento de técnicas que permitam uma compreensão mais profunda do seu funcionamento real. Este trabalho final de mestrado surge dessa ambição, com o objetivo de compreender e estudar um eletrolisador acoplado a um sistema solar fotovoltaico de alta concentração, desenhado e produzido por uma empresa portuguesa. Através deste inovador eletrolisador que possui quatro células eletroquímicas, é possível realizar o processo de eletrólise, no qual a molécula de água é decomposta em hidrogénio na câmara catódica e oxigénio na câmara anódica. Este projeto surge com o desejo de contribuir ativamente para o aprimoramento deste produto altamente inovador, através da criação de diferentes técnicas de instrumentações in-situ do eletrolisador e simulação CFD do componente responsável pela distribuição homogénea da água na câmara anódica nas quatro células eletroquímicas.

Primeiramente foram criados metodologias e procedimentos, de forma a ser possível a criação de protótipos aplicando uma instrumentação in-situ utilizando sondas eletroquímicas para medir e obter valores em tempo real de potencial eletroquímico das camadas interiores do eletrolisador no seu normal funcionamento. Desta forma, é possível uma compreensão mais profunda do funcionamento real das células eletroquímicas, e com isto fornecer à empresa informações importantes sobre possíveis áreas de melhoria do eletrolisador. Também foram criados metodologias e procedimentos para a conceção de protótipos que incorporassem uma instrumentação in-situ utilizando sensores de temperatura. Para isso foram utilizados termopares tipo K capazes de ler em tempo real a temperatura do fluido bifásico (água líquida e oxigénio gasoso) em cada uma das células na câmara anódica e verificar o funcionamento real dentro do eletrolisador. Por último foram aplicados conhecimentos de simulação CFD para avaliar a distribuição de água no flow-field anódico do eletrolisador, com o objetivo de identificar se o design da geometria projetada distribui eficientemente a água às células eletroquímicas. Portanto, este trabalho final de mestrado está essencialmente dividido em cinco capítulos. O primeiro capítulo introduz a tecnologia da empresa para estabelecer uma compreensão geral de como o eletrolisador funciona bem como os seus sistemas adjacentes. O segundo capítulo abrange

toda a documentação relacionada à instrumentação eletroquímica in-situ realizada, descrevendo as metodologias e precauções tomadas, bem como é apresentado e discutido os resultados obtidos. O terceiro capítulo apresenta as metodologias, resultados e discussões relacionadas à instrumentação in-situ do eletrolisador utilizando técnicas de inserção de termopares dentro da câmara anódica do eletrolisador para uma caracterização dos perfis de temperatura em cada célula eletroquímica. No quarto capítulo, descreve as metodologias definidas e criadas para a simulação CFD do flow-field anódico do eletrolisador, juntamente com a apresentação e discussão dos resultados. No quinto e último capítulo, é apresentada uma conclusão abrangente sobre a importância deste trabalho em aprimorar a compreensão deste eletrolisador inovador.

Através da implementação da instrumentação eletroquímica in-situ, os objetivos propostos foram alcançados com sucesso. O objetivo principal de criar e aplicar as metodologias e procedimentos necessários para desenvolver os protótipos apresentados foi alcançado, sendo que os resultados foram validados garantindo confiança e certeza de que a instrumentação realizada não afeta o funcionamento normal do eletrolisador. Isso proporcionou uma melhor compreensão e caracterização do funcionamento do eletrolisador, destacando a importância deste tipo de instrumentação. Essencialmente foi possível decompor os potenciais da célula eletroquímica 1 nas diferentes contribuições de cada camada do núcleo eletroquímico. Além disso, ao fazer referência a artigos científicos que também utilizaram a mesma técnica de instrumentação, foi confirmado que os resultados estão alinhados com a literatura existente e comprovadas as equações apresentadas. Como resultado, é importante destacar que a influência da reação eletroquímica na câmara catódica aumenta com densidades de corrente mais altos, e o aumento ou diminuição da temperatura tem um impacto significativo nos valores de tensão do eletrolisador. Foi descoberto um comportamento irregular nos potenciais eletroquímicos da sonda posicionada no GDL, o que justifica uma investigação mais detalhada para melhorar esse componente e identificar áreas de melhoria. Como trabalho futuro, seria de interesse científico realizar análises semelhantes usando diferentes materiais nas várias camadas, e avaliar os impactos positivos ou negativos dessas mudanças. Outra sugestão seria aplicar esta mesma instrumentação a outras células eletroquímicas para analisar seu comportamento e identificar tendências no eletrolisador.

A instrumentação de sensores de temperatura in-situ proporcionou um ponto de partida muito favorável para a realização deste tipo de instrumentação, sendo que foram

analisadas e discutidas duas técnicas diferentes. A instrumentação em que foram aproveitados os interstícios no design do eletrolisador para a inserção das sondas criou um desequilíbrio na sua operação normal de funcionamento, afetando a compressão dos componentes do núcleo eletroquímico, evidenciado pelos resultados obtidos. Criar um orifício no flow-field permitiu um melhor controlo do problema de compressão no núcleo eletroquímico, e garantiu resultados mais confiáveis. Para trabalho futuro é sugerido encontrar uma maneira de comprimir o eletrolisador enquanto acomoda as inserções dos sensores de temperatura, algo que pode ser melhorado. Nesse tipo de instrumentação, apenas alguns protótipos foram criados, o que impossibilitou ter maior confiança sobre os resultados obtidos.

Através da simulação CFD do flow-field anódico foi alcançada uma compreensão geral da distribuição do caudal da água, o que serve como ponto de partida para uma melhor compreensão deste componente, essencial para o funcionamento adequado do eletrolisador. Primeiramente, ao analisar o flow-field completo no regime laminar nas condições normais de caudal mássico de operação, ficou evidente que existe uma distribuição heterogénea na simulação que representa o comportamento real do eletrolisador quando não existem reações eletroquímicas a acontecer. Através dos resultados obtidos é evidente que podem ser feitas melhorias no design do flow-field, uma vez que é demonstrado que as células 1 e 4 apresentam um caudal mássico médio mais alto do que as células 2 e 3. Uma vez que o eletrolisador opera aplicando a mesma corrente elétrica a cada uma das células, assumindo que as condições são iguais em todas as quatro células, essa distribuição heterogénea pode levar a diferentes condições de operação em cada uma delas, o que pode diminuir o desempenho do mesmo. Portanto, é sugerido como trabalho futuro testar e analisar diferentes geometrias de flow-field para garantir uma melhor distribuição em cada uma das células eletroquímicas. Foi também importante compreender a distribuição da água em cada uma das câmaras individualmente para quantificar a influência da simetria do componente na distribuição do caudal de água. O resultado da simulação aplicando um maior caudal de entrada revelou que existe uma variação de caudal mássico médio bastante significativa entre os canais da célula eletroquímica 4, o que pode influenciar negativamente o funcionamento do eletrolisador quando este está sujeito a maiores velocidades de entrada da água. Como trabalhos futuros, é sugerido continuar o desenvolvimento deste estudo para simular o funcionamento real do flow-field e aprimorá-lo com designs alternativos. Para isso, a

variação da temperatura da água no regime laminar pode ser avaliada para quantificar a temperatura em cada um dos canais e, consequentemente, da célula eletroquímica. Esta simulação será de grande interesse, uma vez que o eletrolisador normalmente opera a temperaturas próximas de 60°C, e é possível que variações na temperatura da água durante o funcionamento possam influenciar a distribuição do caudal da água, potencialmente causando uma distribuição desigual das células eletroquímicas. Outra sugestão é analisar o fluido bifásico (água líquida + oxigénio) formado em cada uma das células eletroquímicas.

Os objetivos globais deste trabalho foram alcançados com sucesso, pois produziram resultados que aprimoram a compreensão do funcionamento do eletrolisador desenhado e industrializado pela empresa portuguesa e, consequentemente, identificam áreas a melhorar no seu desempenho.

List of Abbreviations and Symbols

PEM	Proton Exchange Membrane
CFD	Computational Fluid Dynamics
EU	European Union
CPV	Concentrated Photovoltaics
UPP	Unipolar Plate
CCM	Catalyst Coated Membrane
PTL	Porous Transport Layer
GDL	Gas Diffusion Layer
HER	Hydrogen Evolution Reaction
OER	Oxygen Evolution Reaction
PC	Polarization Curve
CV	Cyclic Voltammetry
OCV	Open Circuit Voltage
Re	Reynolds Number

Index

List of Figures

List of Tables

List of Equations

1. Introduction

1.1. Motivation

Hydrogen has a very promising future, and it is essential for green hydrogen production technologies to focus on developing techniques that enable a better understanding of their actual operation. This project emerges from this ambition, aiming to understand and study an electrolyzer coupled with a high-concentration photovoltaic solar system, with the desire to actively contribute to the enhancement of this highly innovative product.

1.2. Objectives

Increase the understanding and analysis of the electrolyzer, particularly under design conditions. Utilize *in-situ* instrumentation to measure and gain a better understanding of the operation of the electrochemical cells, offering insights about potential areas for improvement. Additionally, employ CFD simulation to assess the water distribution within the anodic flow-field, aiming to determine whether the geometry used effectively distributes water to the electrochemical cells.

1.3. Structure

This master thesis is essentially divided into five chapters. The first chapter introduces the technology to establish a general understanding of how the electrolyzer and its incorporating systems work. The second chapter encompasses all the documentation related to in-situ electrochemical instrumentation done, covering methodologies, precautions taken, as well as presenting and discussing the results obtained. The third chapter outlines the methodologies, results, and discussions related to the instrumentation of electrolyzers using temperature in-situ probes techniques for a more detailed characterization of temperature profiles in each electrochemical cell. In the fourth chapter, methodologies for CFD simulation of the anode flow-field of the electrolyzer are presented, along with the presentation and discussion of the simulation results. In the fifth and final chapter, a comprehensive conclusion is presented regarding the significance of this work in increasing the understanding of this innovative electrolyzer.

2. Case study

This project originates from a partnership with a Portuguese company specializing in the development of a compact and small-scale electrolyzer. The distinguishing feature is the modularity of the electrolysis device, which, being a compact equipment, can be easily coupled with a continuous supply of renewable energy sources, including solar, wind, hydro, and others. This modularity makes the electrolyzer suitable for deployment anywhere in the world, enabling the decentralization of hydrogen production.

Through this innovative electrolyzer, it is possible to perform water electrolysis electrochemical process, where the water molecule is decomposed into hydrogen inside the cathodic chamber and oxygen inside the anodic chamber. In this report, we will explore its application when integrated with a high-concentration photovoltaic panel system, as schematic in the Figure 1.

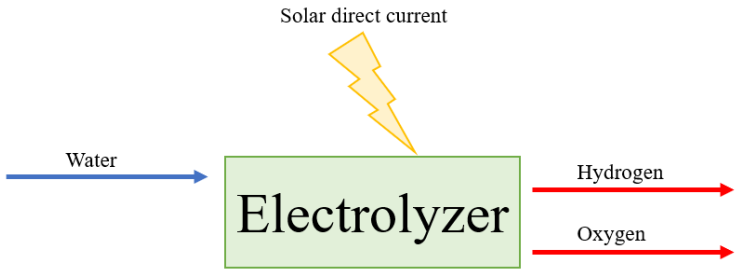

Figure 1 - Basic principle about the electrolyzer operation

In this chapter, we will provide a brief introduction to the utility of hydrogen in our near future and present and an overall framework of the technology, along with all the systems and physical principles involved.

2.1. Hydrogen Economy

The awareness of the global warming and the finite availability of non-renewable resources has led to a growing global concern for cleaner and more sustainable energy sources [1]. Hydrogen, being the most abundant element in the universe, has emerged as a viable alternative for a sustainable energy solution, once it has high energy content per unit of mass (which is more than triple that of typical liquid fuels such as gasoline and diesel) [2].

Studying, analyzing, and understanding the advantages and disadvantages that hydrogen can offer in energy transportation are of utmost importance, as it could offer numerous benefits in reducing carbon emissions, diversifying energy sources, and making the energy landscape more compact and varied. A recent illustration of this is Europe's reliance on Russian fossil fuels, which has prompted the European Union to intensify its endeavors to attain its climate neutrality target by 2050 [3]. The Commission introduced the Repower EU strategy in 2022 that aims to enhance the affordability, security, and sustainability of energy within the EU [3]. As part of this plan, the EU is committed to scaling up its production of renewable hydrogen by 2030, increasing the target from the previously proposed 10 megatons per year in the 2020 Hydrogen Strategy to a new goal of 20 megatons per year [3]. There is a significant effort and emphasis on green hydrogen production in Europe. Hydrogen can have various applications, including [1]:

- Versatile energy carrier.
- Mobility applications.
- Power generation.
- Storage of renewable energy.
- Fertilizers production.
- Petroleum refining processes.
- Chemical and petrochemical industries.

There are extensive research endeavors actively progressing to enhance sustainable hydrogen generation technologies. Presently, the most established and widely employed method involves hydrocarbon reforming [4]. The development of renewable hydrogen production technologies is a vital step moving forward into a truly sustainable human existence; the use of renewable resources for energy generation is pivotal [1]. So, it is crucial to focus on the study and analysis of hydrogen's applications as well as its production, aiming for a 100% green production process with minimal environmental impact and reduced use of finite and rare natural resources [5].

This investigation is vital to develop a cleaner, more sustainable, and energy-accessible future to next generations, focusing on the production of green hydrogen using electrolysis processes, more specifically the PEM (Proton Exchange Membrane) technology.

2.2. System Technology

In this chapter, the systems used for green hydrogen production will be described, along with their laboratory applications to facilitate the experiments conducted throughout the experiences done. The technology englobe various processes organized into singular systems, all centered around their innovative and singular electrolyzer. In summary we can categorize the processes into the following:

- Water supply
- Solar System
- Electrolyzer
- Oxygen + Water System
- Hydrogen System.

These systems are structured as depicted in the Figure 2. First the incoming water is treated, and the pumping system is designed to flow it through the electrolyzer. Here, utilizing the electrical energy generated by high-power solar panels and heating the water through the thermal energy harnessed by this system, the electrolysis of water occurs. During this process, the water molecule is decomposed into hydrogen and oxygen.

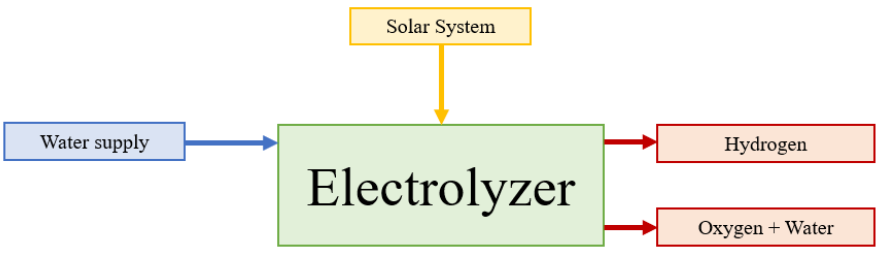

Figure 2 - Schematic about the relation between the systems technology

2.2.1. Water supply

First, the water undergoes pre-filtration to remove larger impurities and solid particles. Then, it must undergo treatment to achieve an appropriate conductivity level for efficient electrolysis within the electrolyzer. To achieve this, it needs to pass through a reverse osmosis device aimed at decreasing the conductivity value, as shown in the Figure 3.

An osmosis device, specifically reverse osmosis, is a water filter that uses energy to move water through a semi-permeable material, removing impurities and unwanted ions from the water [6]. This process produces pure, clean water by separating impurities such as salt, minerals, bacteria, and viruses in the water. This process decreases the water's conductivity, a critical factor when supplying the electrolyzer to increase the efficiency and prevent issues related to corrosion and deterioration of its core components. Once it has passed through an osmosis device, to ensure the system's proper operation, it is necessary to maintain a constant flow of supply to the electrolyzer. This implies that the entire water pumping system must be well-designed and sized to ensure that there is no backflow in the piping and to maintain uniform pressure at the inlet of the electrolyzers.

Figure 3 - Water supply circuit

2.2.2. Solar System

The electrolyzers are attached to a high efficiency concentrated photovoltaic (CPV) panel using Fresnel lenses. As shown in the Figure 4, the Fresnel lenses focus the collected radiation onto a single point, where a high efficiency concentrated photovoltaic panel is located, generating electrical current using the solar radiation [7].

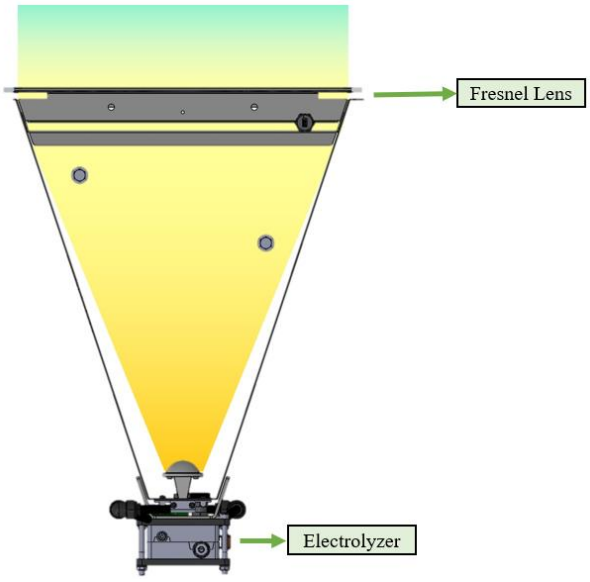

Figure 4 - CPV Solar System

These panels, in turn, are assembled to form a tracker (represented in the Figure 5) that, through a tracking sensor, follows solar radiation to generate electricity to supply the electrolyzers integrated into the system and heating the inlet water.

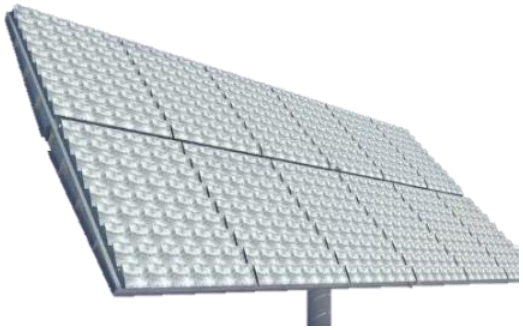

Figure 5 – Photo of the tracker

The thermal energy produced in this process is also utilized to heat pre-treated water from the water system, thereby increasing the efficiency of the electrolysis process. When combined with a high efficiency concentrated photovoltaic tracker, the electrolyzer can harness almost 100% of the sun's energy, both electrical and thermal, to enhance the efficiency of the electrochemical process and lower the levelized cost of green hydrogen.

For the experiments detailed in this report, a laboratory solar system was employed as a replacement for the actual company registered real solar system. This substitution allowed for better control of all variables involved. The direct current injection system and the water heating system were separated to enable more precise control of these two variables, independent of solar conditions once the prototypes were tested inside the laboratory. For heating the water, a direct current injection device was employed within a water heating system that allows for the use of the same heat exchangers used in the trackers to reach the desired water temperature, as shown in the Figure 6.

Figure 6 - Water heating system used in the laboratory.

To supply direct current to the electrolyzer terminals, a direct current source was employed. In some experiments, the source was TDK-Lambda, while in others, the Bio-Logic SAS VMP-3e Potentiostat was used, as shown in Figure 7.

Figure 7 - Power supply equipment

2.2.3. Oxygen chain System

As a result of the electrochemical reaction in the electrolysis, there is an excess of liquid water and gaseous oxygen at the outlet of the electrolyzer's anode chamber. It is crucial to develop a circuit capable of discarding this reaction product, which consists of a biphasic fluid. To achieve this, a circuit which separates the two-phase fluid was developed, to isolate the oxygen produced and transport the collected water to the water supply distribution system of the entire system, as show in Figure 8.

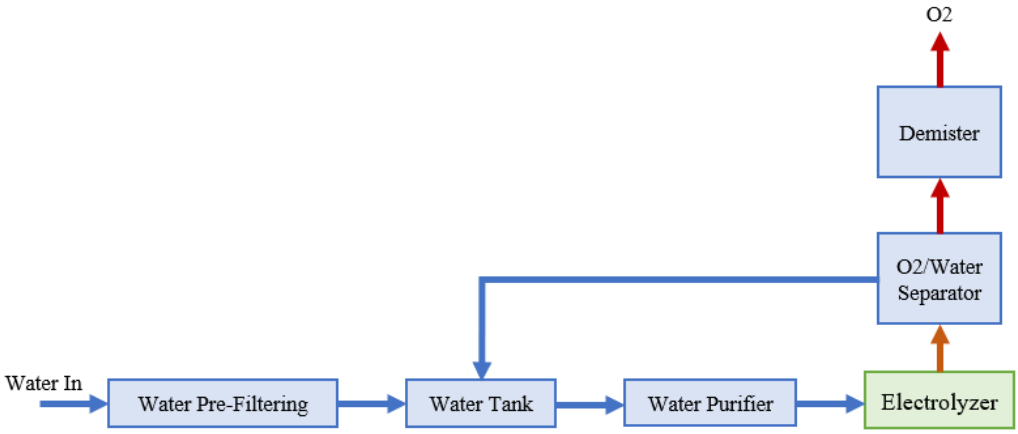

Figure 8 - Circuit of the oxygen chain

2.2.4. Hydrogen chain System

To collect the hydrogen produced from the electrochemical reaction of water electrolysis, a properly sized system is required to transport the output from the cathode chamber of the electrolyzer, which consists of hydrogen and small amounts of water. Here, a separator of hydrogen is used to isolate the hydrogen produced and return the excess water to the water supply system, as show in Figure 9. The hydrogen pipes are going to the hydrogen storage system, and it is pressurized to a defined project pressure to storage the hydrogen produced and be able to transport and use it in the various applications.

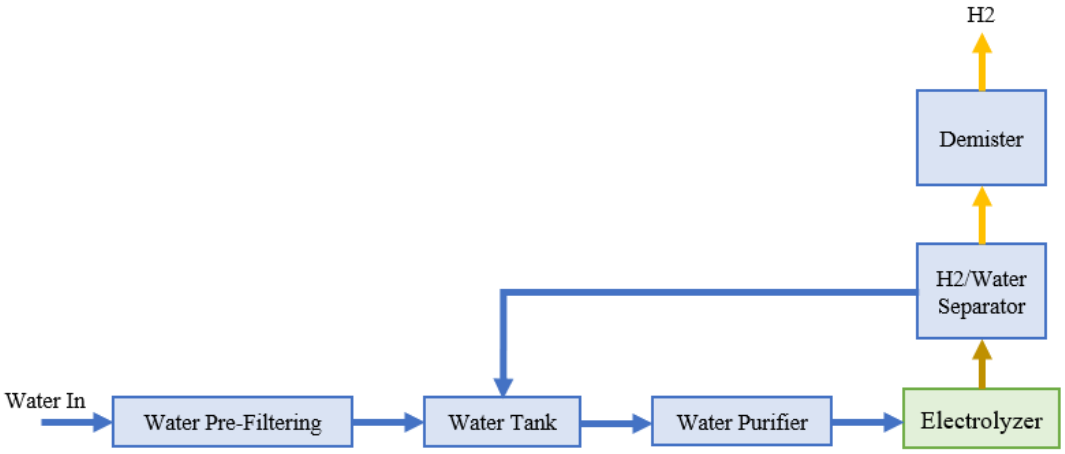

Figure 9 - Circuit of the Hydrogen chain

2.3. Electrolyzer

2.3.1. Characterization

The electrolyzer is the core technology to produce green hydrogen. This electrolyzer is an exceptionally compact and small device (Figure 10), which offers a characteristic modularity, allowing for versatile usage in various settings and locations.

Figure 10 - Photo of a standard electrolyzer

The primary purpose of the electrolyzer is to efficiently transform pre-treated water into hydrogen and oxygen through direct current. The PEM technology plays the pivotal role of permitting the passage of hydrogen ions between the anodic and cathodic chambers, that is possible to visualize in Figure 11.

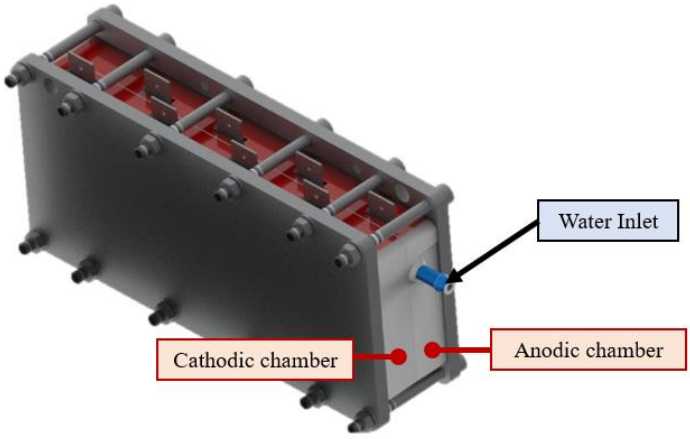

Figure 11 – Isometric view of the modeled electrolyzer

The electrolyzer features four electrochemical cells connected in series. The treated water enters the anodic chamber of the first cell with a typical flow rate of 20 mL/min. After the distribution of water among each of the 4 cells, it undergoes decomposition in the anodic chamber, resulting in the production of gaseous oxygen and excess liquid water at the anodic chamber. In the cathodic chamber, which comprises the opposite side of the protonic membrane, there is an outlet for hydrogen, while the produced gaseous hydrogen and the excess of liquid water exits the electrolyzer through the outlet of cell 4.

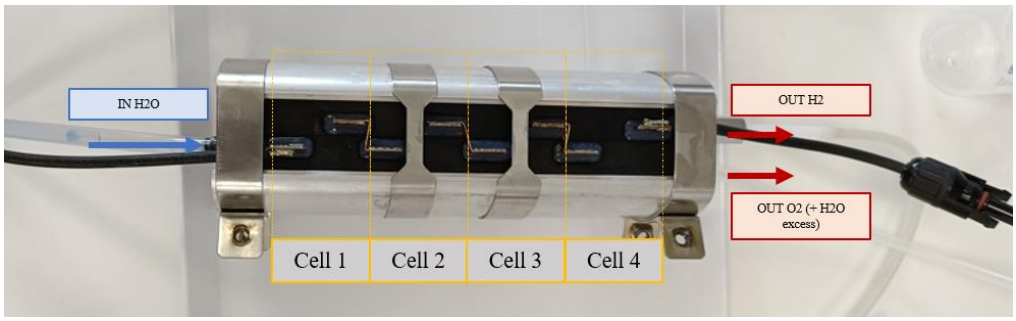

Figure 12 - Characterization of the electrolyzer

The electrolyzer features an electrical zigzag configuration connected in series, as shown in Figure 13. In this arrangement the positive pole of the electrical power supply is connected to the anodic electrode of the first cell, while the negative pole is linked to the cathodic electrode of the fourth cell. The electrical current supplied to cell 1, which initiates the water electrolysis process in this cell, is transferred to the anodic and cathodic electrodes of cell 2, and so forth, until it reaches the last cell of the electrolyzer - cell 4.

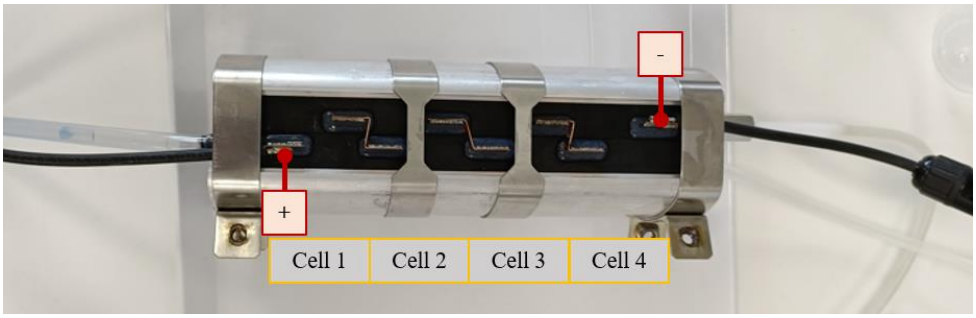

Figure 13 - Electric connections in the electrolyzer

Another highly significant aspect of the electrolyzer is the compression of its components. An assembly pressure of approximately 2 ton is employed to ensure a consistent pressure within the electrolyzer core. This ensures that each of the electrochemical cells operates under identical and ideal conditions for electrolysis. The process of an electrolyzer compression is presented in Figure 14.

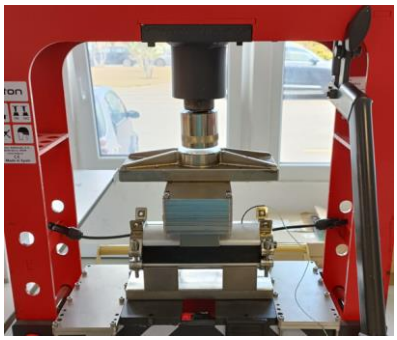

Figure 14 – Compression process of an electrolyzer

2.3.2. Components

The electrolyzer consist of a multi-material and multi-interfacial system that has several components. In this section, we will provide a detailed overview of each constituent part and its primary function in the operation of the electrolyzer.

The electrolyzer is almost symmetrical up to the electrochemical core, only differ in the material and design of the UPP (Unipolar Plate) and the different layers in the electrochemical core. Table 1 lists all the components, starting from the outermost component of one of the chambers and progressing to the heart of the electrolyzer and in the Figure 15 is represented the exploded view of the components in the anodic chamber.

Table 1 - Summary about the principals' components of the electrolyzer

Component	Material
Terminal Profile	Aluminum
Enclosure	C1200HF – 76701
Compression Pads	Metal plates - Inox Silicon pads - Silicone
Flow-Field	C1200HF – 76701
UPPs	Titanium*
Electrochemical core	-

* - Anode and Cathode have different coating

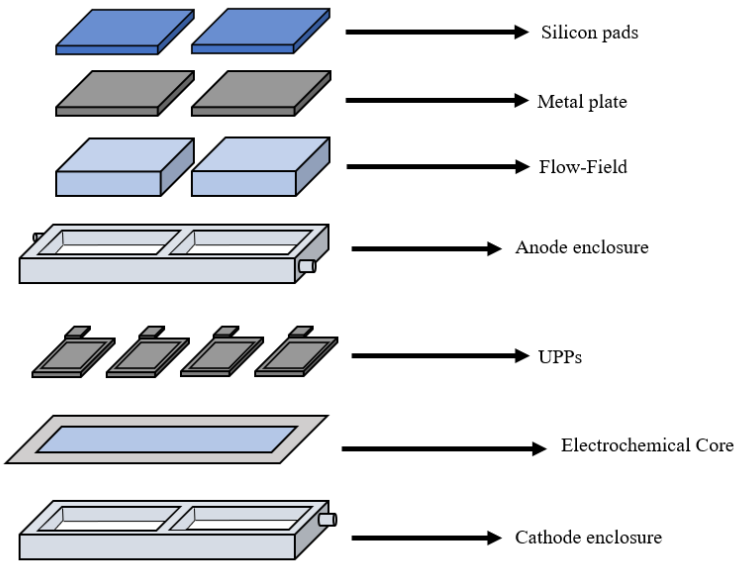

Figure 15 – Schematic about the components of the anodic chamber

Terminal Profile

The terminal profile is the outermost component of the electrolyzer, and it is composed of an aluminum alloy. Each electrolyzer consists of two terminal profile components that define the electrolyzers boundary with the external environment, both in the anodic and cathodic chambers, as represented in Figure 16. This component ensure that the rest of the constituents are compressed at the specified design pressure and ensure that the compression is uniform throughout the entire electrolyzer. To achieve this compression, four clamps are used to seal the electrolyzer and maintain the defined compression value.

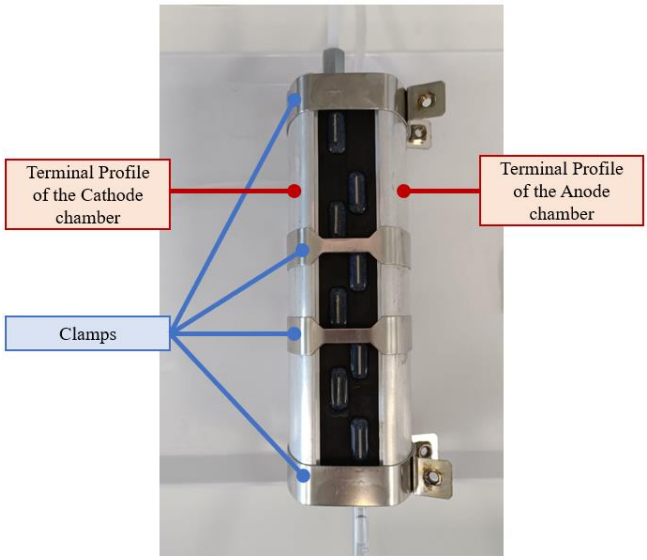

Figure 16 - Photo about the terminal profiles of the two chambers

Enclosure

The enclosure is made of a resin (C1200HF – 76701) designed and engineered to support the metal plate, silicon pads, flow-field, and the electrochemical core, ensuring that all components are in their correct positions. It also serves to separate the interior of the electrolyzer from the external environment, with both the anodic and cathodic chambers featuring a component of this type, shown in Figure 17. This component is responsible to assure tightness against water leaks and oxygen/hydrogen leaks and provide mechanical stability to the electrolyzer.

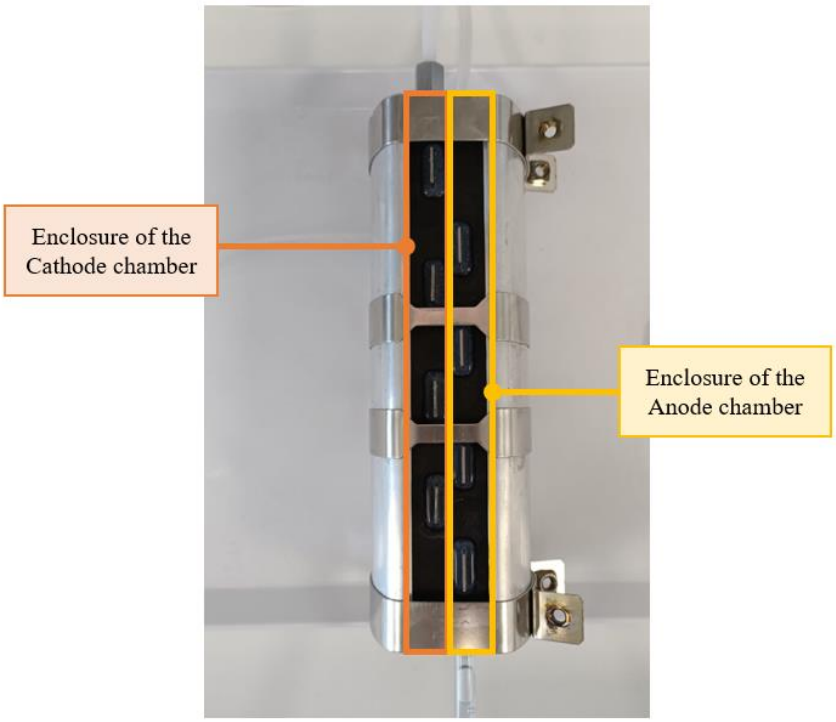

Figure 17 – Enclosures of the two chambers on a real electrolyzer

Compression Pads

Consists of two different materials stacked on top of each other: the metal plate (Inox) and the silicon pads. Each chamber, both anodic and cathodic, is constituted by two compression pads once this component is inserted into each one of the flow-field components. Together, they ensure a homogeneous distribution of compression force to guarantee that the electrochemical core of the electrolyzer is subjected to the same pressure conditions.

Flow-Field

Each chamber is constituted by two flow-fields (chamber 1 and chamber 2) connected in series to supply all the four cells, as exemplified in Figure 18 for the anodic side. The two chambers that constitutes the entire flow-field have two different chambers: one symmetric and other asymmetric.

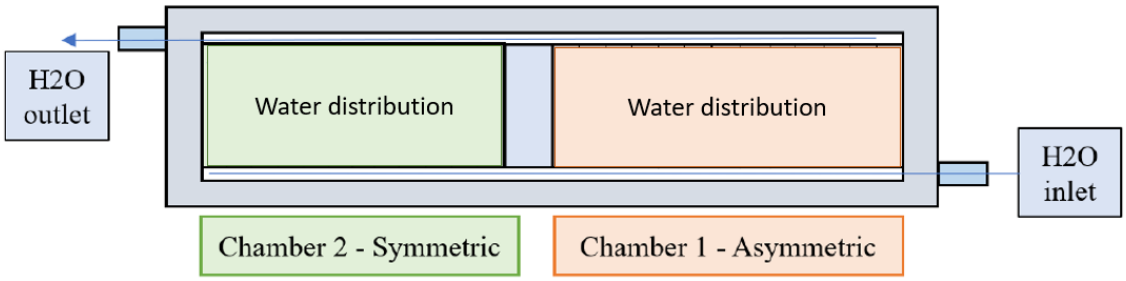

Figure 18 – Schematic about the anodic flow-field chambers

In the anodic chamber this component is responsible for a homogeneous distribution of water' supply to each one of the electrochemical cells and remove efficiently the resultant products of the water electrolysis reaction in this chamber: gaseous oxygen and excess of liquid water. In the cathodic chamber, it is responsible to remove efficiently the hydrogen produced. As demonstrated in Figure 19 for chamber 1 (asymmetric) in the anode side, the electrolyzer receives the water in a common channel, and then the water is distributed through channels that ascend to a common outlet channel. Ideally, the same water mass flow transits through each of the channels, ensuring a good distribution of water on each different electrochemical cell.

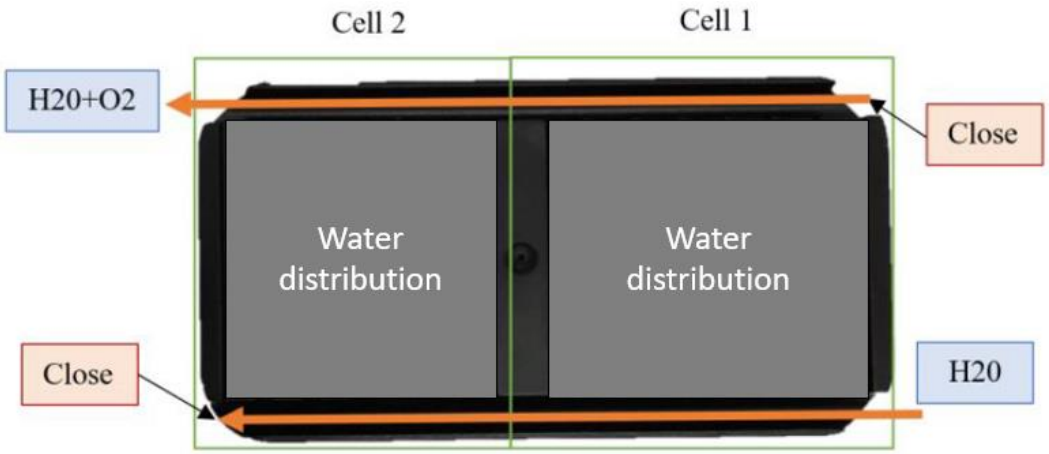

Figure 19 - Water distribution in chamber 1 of the anodic flow field

UPPs (Unipolar Plates)

This component has the main function to assure electrical conductivity from the anodic chamber to the cathodic chamber of an electrochemical cell. Each cell has one anode UPP and one cathode UPP that must be at a potential capable of decomposing the water molecule in the anodic chamber. The two UPPs of the same cell are subjected to different voltage values, and the result of the electrochemical reaction varies in both

chambers. Due the electrolysis electrochemical reaction the water suffers oxidation in the anodic chamber and the hydrogen ions are reduced in the cathodic chamber.

As a result, the anode UPP has a distinct geometry and coating compared to the cathode UPP. In the anodic chamber, the geometry is designed to guide water to the electrochemical core, conduct electrons to break down water molecules and then evacuate the produced gaseous oxygen. The anode UPP is composed of a titanium alloy with a platinum coating.

In the cathodic chamber, this component is designed to conduct electrons to the hydrogen ions and evacuate the hydrogen produced. It is made from a titanium alloy coated with gold. The Figure 20 illustrates the design and coating of the anode UPP and cathode UPP.

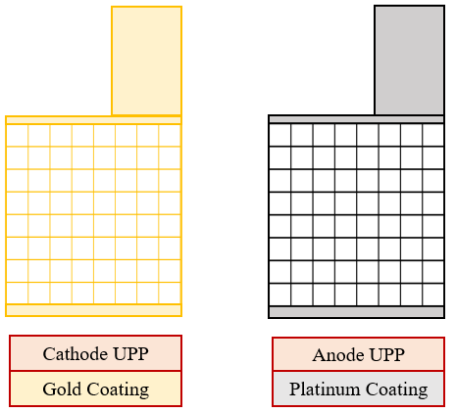

Figure 20 – Schematic about the cathode and anode UPPs and the respective coating

Electrochemical Core

This is the heart of the electrolyzer, and it is where water electrolysis takes place. Each cell consists of the electrochemical core described in Figure 21, where the reaction occurs. It is a multi-material and multi-interfacial system, and each layer must be selected with precision. The core consists of CCMs (Catalyst Coated Membranes), which serve the primary purpose of enabling the PEM electrolysis process and optimizing the electrochemical reaction as efficiently as possible. This CCM, in turn, is composed by:

- PEM – Proton Exchange Membrane
- Anode catalytic layer - iridium oxide
- Cathode catalytic layer - platinum/carbon

Subsequently, to enhance the efficient transport and evacuation of the products of the electrochemical reaction, there are two additional layers that compose the electrochemical core before reaching the UPPs:

- Anode: PTL (porous transport layer) that is constituted by titanium mesh.
- Cathode: GDL (gas diffusion layer) composed by carbon fibers.

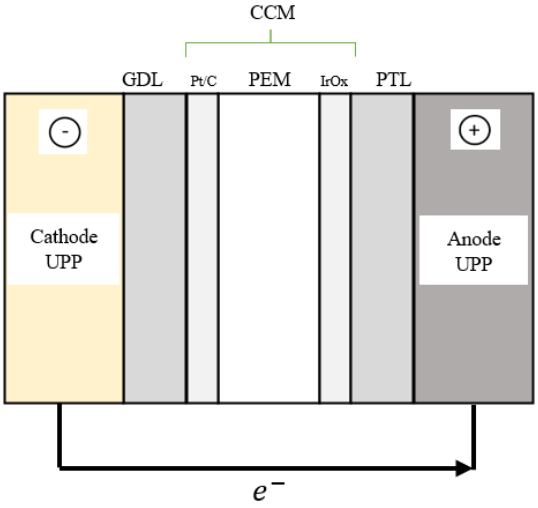

Figure 21 - Schematic about the electrochemical core of the electrolyzer

The details of each layer within the electrochemical core will be elaborated upon in subsection 2.3.3.3. providing additional insights into the electrochemical principles underpinning the technology employed in the electrolyzer.

2.3.3. Electrochemical fundamentals

In this subsection, a brief explanation and introduction to the technology used by the electrolyzer, along with the general equations that govern the PEM electrolysis technology and the state of art of this tech will be presented.

2.3.3.1. Water Electrolysis

Water electrolysis is an electrochemical process where electricity is utilized to divide water into hydrogen and oxygen. This method is one of the most straightforward ways to generate hydrogen and oxygen with zero pollution, and it has been known for over two centuries [8]. In standard conditions of temperature and pressure ($T_0 = 298K$,

$P_0 = 1\ bar$) the water can be dissociated into its elemental components (molecular hydrogen and oxygen) according to [9]:

$$H_2O\ (l) + \text{electricity} \rightarrow H_2(g) + \frac{1}{2}O_2(g) \quad (1)$$

The reaction is endothermic; therefore, the reaction is non-spontaneous, and the Gibbs free energy is positive. The Gibbs free energy is a thermodynamic potential that is used to determine the useful work that can be done in a thermodynamic system when the temperature and pressure are constant [8]. For other words, the Gibbs free energy determines the total capacity of the system to do work and, under constant pressure and temperature conditions with no work involved can be represented as [9]:

$$\Delta G = \Delta H - T\Delta S \quad (2)$$

Where,

- ΔH – variation of enthalpy
- T - temperature
- ΔS - variation of entropy
- ΔG - variation of free Gibbs energy

If the value is negative the reaction is spontaneous. In water electrolysis the Gibbs free number is positive, meaning the reaction is non-spontaneous and endothermic, thus the system increases enthalpy value absorbing heat from the environment [9]. The variation of the free Gibbs number can be written as the function of the concentrations of the species that participates in the chemical reaction, using the equation [10]:

$$\Delta G = \Delta G^0 + RT.\ln\left(\frac{a_M^m.a_N^n \ldots}{a_A^a.a_B^b \ldots}\right) \quad (3)$$

Where $a_M^m, a_N^n \ldots a_A^a.a_B^b$ are the species involved.

Certain species participating in the electrode reaction exist in solid or pure liquid states and it is typically considered a value of one. When it comes to gases, their activity is often represented by the partial pressure of the gases as expressed in the atmosphere [8]. Similarly, for ions in a dilute solution, their activity is commonly regarded as their

molar concentration. By substituting the reactions in the equation and dividing both sides of the equation by $-nF$, we obtain at the Nernst equation [10]:

$$E_{cell} = E^0 - \frac{RT}{nF} \ln \left(\frac{a_M^m . a_N^n \ldots}{a_A^a . a_B^b \ldots} \right) \quad (4)$$

Where,

- E_{cell} - cell potential [V]
- E^0 - standard cell potential at standard conditions (1,229 V [11])
- R - gas constant
- T - absolute temperature [K]
- n - number of moles of electrons exchanged in the electrochemical reaction.
- F - Faraday constant

The Nernst equation enables the determination of the cell potential in a water electrolysis cell when operating under non-standard conditions, accounting for the impact of variables of temperature and concentration [8]. This equation serves as a valuable tool for comprehending and forecasting the performance of water electrolysis systems in diverse situations.

So, it is necessary to suppress the equilibrium potential required for water splitting, results in the decomposition of water molecules. This process generates hydrogen gas through the hydrogen evolution reaction (HER) at the cathode and oxygen gas through the oxygen evolution reaction (OER) at the anode [11].

2.3.3.2.PEM Technology

State of Art

From a historical perspective, in 1950, the United States' space program introduced a solid polymer electrolyte as an innovative method for producing hydrogen and oxygen in zero-gravity environments [9]. The need for a device capable of functioning without any liquid electrolyte to prevent bubble formation led to significant advancements in this technology to maximize efficiency. A solid membrane infused with liquid electrolytes was developed, offering the advantage of operating with protons instead of hydroxide

ions, as seen in alkaline technology [9]. A significant step in this development occurred in 1960 with the synthesis of sulfonated tetrafluoroethylene which led to the creation of the *Nafion* brand [10].

In the 1960s, General Electric pioneered the development of the first solid polymer-based electrolyzer [5].This concept, conceived by Grubb, utilized a solid sulfonated polystyrene membrane. The first scientific publication on a PEM was authored by Russell et al. in 1973, using a PEM cell from General Electric. This publication already highlighted hydrogen's pivotal role in the future global energy landscape [12].

Principle

The structure and operation principle of a PEM electrolyzer involves the use of a polymer membrane that only allows the passage of protons. This leads to the decomposition of water at the anode, where electrochemical reactions occur, resulting in the formation of oxygen [5]. Simultaneously, at the cathode, hydrogen is generated. When pure water enters the electrolyzer cell and encounters the anode, the separation of hydrogen ions (H+, proton) and oxygen occurs in the catalytic layer of the anode. Oxygen remains on the anode chamber, while the hydrogen ion (H+) crosses the polymer membrane and, upon contacting the catalytic layer of the cathode, receives electrons, transforming into gaseous hydrogen [5]. The reaction will generate oxygen (from the anode region) and hydrogen (from the cathode region), with a portion of the energy supplied for electrolysis being converted into thermal energy. This occurs due to ohmic, concentration, and activation losses within the cell, leading to a temperature increase [1].

The global equation of the electrochemical reaction that happens inside the electrolyzer is represented in the equation where the ΔH_R parcel denotes the change in the reaction enthalpy for this endothermic reaction once the thermodynamic process result in an increase of the system enthalpy [13].

$$H_2O\ (l) + \Delta H_R \rightarrow H_2(g) + \frac{1}{2}O_2(g) \tag{5}$$

The two half-reactions that occurs in the anodic and cathodic chamber is given by [1]:

Anode: $H_2O \rightarrow 2H^+ + \frac{1}{2}O_2 + 2e^-$ (6)

Cathode: $2H^+ + 2e^- \rightarrow H_2$ (7)

Figure 22 a schematic on the principles of PEM technology as the different layers of the electrochemical core of a typical PEM reaction is presented.

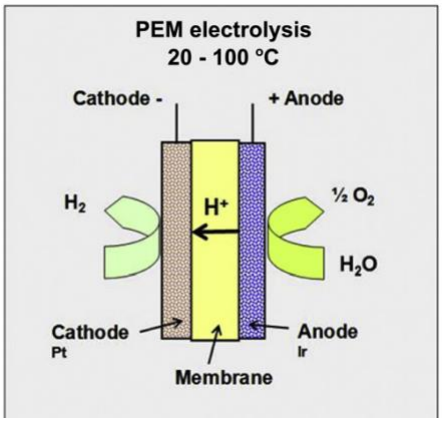

Figure 22 - Schematic of the operating principle of PEM water electrolysis cell *[12]*

For the decomposition of water, external energy is needed to split up the molecules to its components. The amount of energy required or the energy that is released by building up or breaking up a chemical bond is called the reaction enthalpy ΔH_R [8]. The explanation about this parcel is shown in the previously subchapter, and it is necessary a reversible voltage of 1.23V at standard conditions to break the water molecule [4]. So, it is fundamental to guarantee a potential greater than this potential to overcome the resistance present by the ohmic, electric, mass transport resistances, etc... due to the electrolyzer design. The compression of the components has a big impact on the overall resistance values as the water temperature inside the electrochemical core [8].

2.3.3.3.Electrochemical Core

As previously explained in the component's subsection, the electrochemical core serves as the heart of electrolyzer, where the electrochemical reaction takes place. Each cell is composed by the electrochemical core where the reaction happens. It is a multi-material and multi-interfacial system, and each layer must be carefully chosen to perform in the most efficiency way. Figure 23 represents the electrochemical core with the UPPs and flow-fields of each chamber.

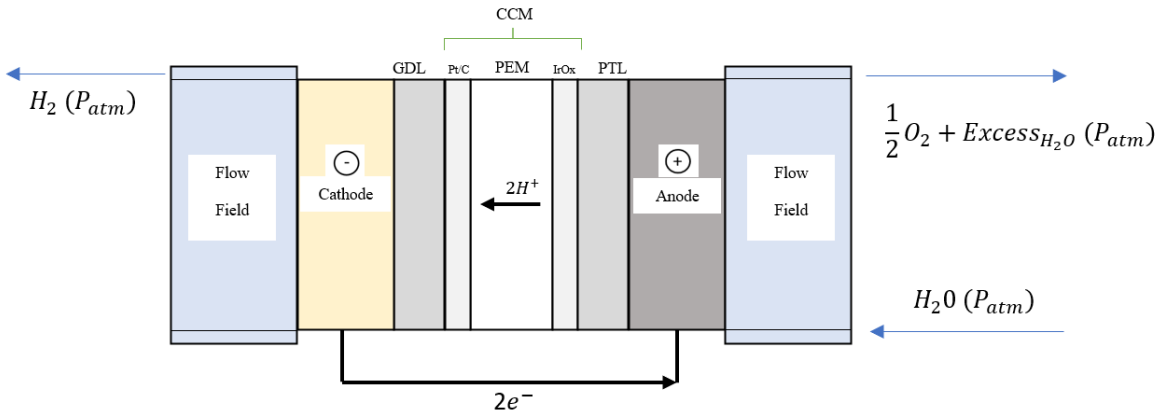

Figure 23 - Schematic about the principle of the electrochemical core of the electrolyzer.

It will be explained how the reaction unfolds inside the electrolyzer, starting from the introduction of water into the anodic flow field and concluding with the completion of the electrochemical reaction. Additionally, the materials used in each layer and the rationale behind their selection will be presented. To begin, water enters the anodic chamber through the anodic flow-field. Due to the specific geometry of the Anodic UPP and the PTL (most common referenced it as “mesh”), it reaches the catalytic layer of iridium oxide, where water electrolysis occurs due to the electrical potential to which the anodic UPP is subjected. The direct current is applied due the availability of the sun, as the water temperature. The hydrogen ions produced pass through the *Nafion* membrane to reach the catalytic layer of platinum/carbon, where the electrons combine with the hydrogen ions to form gaseous hydrogen. Finally, through the GDL, which consists of a carbon layer, the produced hydrogen gas is transported and guided through the designed interstices in the cathodic UPP, reaching the cathodic flow-field to facilitate the exit of the generated gas from the electrolyzer system.

3. Electrochemical in-situ Probe Instrumentation

In this chapter, the assembly methodologies applied to all experiences realized throughout the electrochemical instrumentation will be explained.

3.1. Application and Principles

The application of a reference electrode to the electrolyzer' first cell will be described in this chapter. This technique offers a real-time visualization of the electrochemical potential where the probe is positioned in a specific position, making it possible to observe the electrochemical potential in the specified layer [14]. As represented in Figure 24, an ionic bridge was created connecting a layer inside the electrochemical core of the cathode chamber in the electrolyzer' first cell and a solution of H_2SO_4 that has the reference electrode linked.

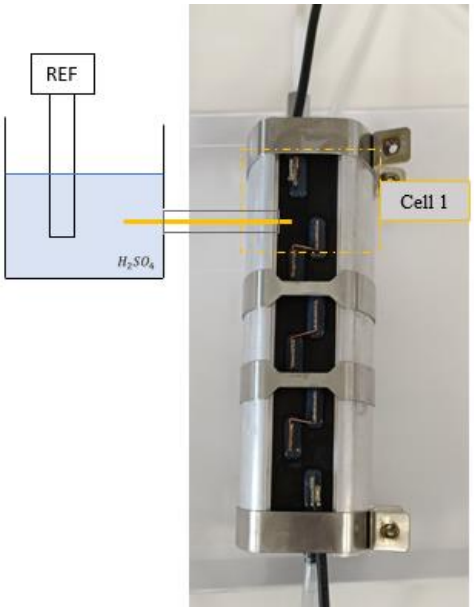

Figure 24 - Schematic about the instrumentation in-situ of the electrolyzer first cell.

To execute the planned experience, a *Nafion* tube was inserted inside a tube with an outer diameter of 1.95mm and an inner diameter of 1mm to ensure that the electrochemical probe maintains an ionic bridge to the defined terminal. This tube was inserted through the holes created through the electrolyzer components to establish contact with one of the four positions where the experiment occurred. The ability to visualize this measurement provides us with the capability to monitor the potential evolution within the electrolyzer, offering crucial insights into the degradation

mechanisms in both the cathodic and anodic chambers [14]. The main objective is to isolate the potential in a specific layer inside the cathode and anode chamber to identify areas for improvement the performance of the electrolyzer. Figure 25 represents a schematic of the probe position in the first cell of the first prototype done: at the catalyst layer of the cathode chamber constituted by Pt/C.

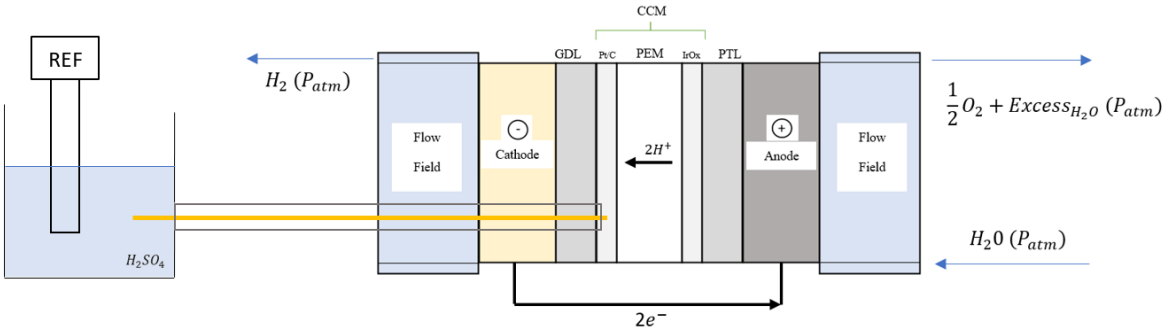

Figure 25 - Schematic about the position of the Pt/C Probe in the Cell 1.

The Bio-Logic SAS VMP-3e Potentiostat was used to obtain in-situ potential readings for each of the prototypes. The current injection system and water heating are detailed in the previous chapter since all experiments were conducted in a laboratory setting. Figure 26 represents the different probe positions that were instrumented. To achieve the desired instrumentation, numerous prototypes were developed, and various methodologies were created to meet the proposed objectives. In this chapter, we will describe all the steps taken during the experiments, including the presentation of validated experiments and the discussion of results related to this innovative instrumentation.

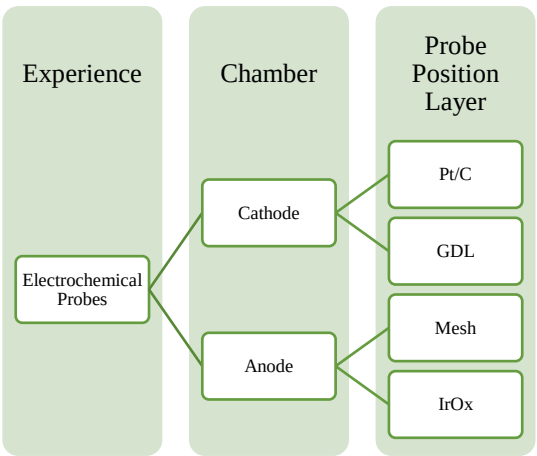

Figure 26 - Prototypes created through the experiments.

3.2. Probe Potential Equations

In this subchapter, the equations that explain the electrochemical potential decomposition will be presented. First, the global equations, and then the details for each electrode, attempting to decompose them for each of the electrochemical probes.

The measured full cell potentials can be decomposed in the reversible cell voltage given by the Nernst equation (U_{rev}), electronic resistances (R_{el}), membrane resistance (R_{mem}), proton resistances at the cathode and anode side ($R_{H^+}^{cl}$), activation losses (η_{act}), and mass transport losses (η_{mt}), as represented in the following equation [15]:

$$U_{cell} = U_{rev} + i\left(R_{el} + R_{mem} + R_{H^+}^{cl}\right) + \eta_{act} + \eta_{mt} \tag{8}$$

The total potential of one cell can be decomposed in the cathode and anode potential. The difference of both half-cell signals results in the full cell voltage measurement [15]:

$$U_{cell} = U_{anode} - U_{cathode} \tag{9}$$

The anode has a positive potential once the water is being oxidized and, in the cathode, the water is being reduced, which results in negative signal. The following figure represents the ionic potential evolution (green) and the electric potential evolution (blue) that occurs inside an electrochemical cell. Figure 27 is a self-made schematic applied to the electrochemical core according to the [15].

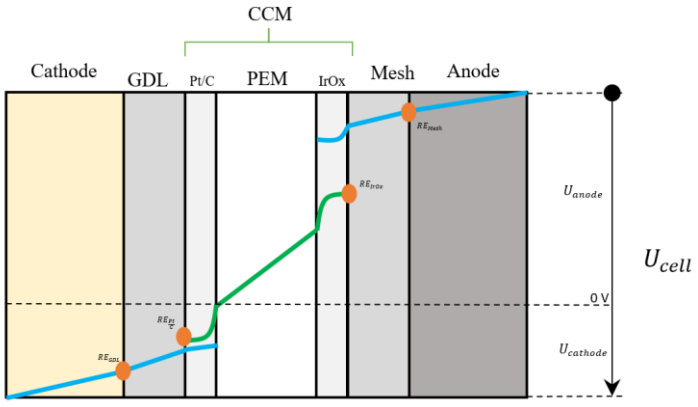

Figure 27 - Ionic and Potential evolution in the electrolyzer electrochemical core.

At the anode side, the measured anode potential is constituted by the Nernst potential (E^A), electric resistances across the UPP ($R_{el}^{Upp^A}$ *and* $R_{el}^{Upp/Mesh}$), Mesh

(R_{el}^{Mesh}) and IrOx layer and interfaces ($R_{el}^{Mesh/IrOx}$), mass transport losses (η_{mt}^{A}) and activation losses (η_{act}^{A}), as shown [15]:

$$E_{anode} = E^{A} + i\left(R_{el}^{Mesh/IrOx} + R_{el}^{Mesh} + R_{el}^{Upp^{A}} + R_{el}^{Upp/Mesh}\right) + \eta_{mt}^{A} + \eta_{act}^{A} \quad (10)$$

For a better understanding, Figure 28 provides a representation of the electron path in the anode chamber, illustrating each layer that the electron must cross before reaching the UPP, which is then connected to the cathodic UPP. The orange circles represent the position of the two probes inserted.

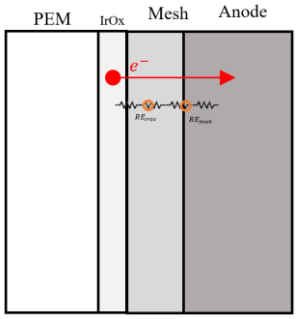

Figure 28 - Schematic about the electron path cross the anode electrochemical core of the electrolyzer.

At the cathode side, the measure cathode potential is constituted by the Nernst potential (E^{C}) and the electric resistances across the UPP ($R_{el}^{Upp^{C}}$ *and* $R_{el}^{Upp/GDL}$), GDL (R_{el}^{GDL}) and Pt/C layer and interfaces ($R_{el}^{\frac{Pt}{C}/GDL}$), mass transport losses (η_{mt}^{C}) and activation losses (η_{act}^{C}), as shown [15]. It is important to emphasize that in this discretization, the activation loss component has an opposite sign to the rest of the equation, which may be significant in the analysis of the results.

$$E_{cathode} = E^{C} - i\left(R_{el}^{\frac{Pt}{C}/GDL} + R_{el}^{GDL} + R_{el}^{Upp^{C}} + R_{el}^{Upp/GDL}\right) - \eta_{mt}^{C} + \eta_{act}^{C} \quad (11)$$

In Figure 29 the electron path is represented, starting from the cathodic UPP, and extending to the Pt/C catalyst layer. There, in conjunction with hydrogen ions, it forms the gaseous hydrogen in the electrolysis reaction. The orange circles show the probe positions in this chamber.

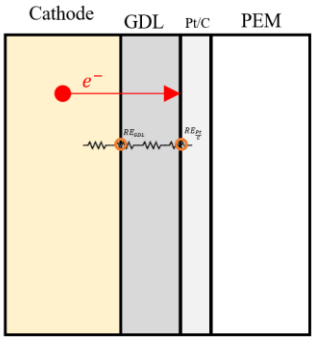

Figure 29 - Schematic about the electron path cross the cathode electrochemical core of the electrolyzer.

It is essential to attempt to decompose the voltages in each layer where an electrochemical probe will be instrumented. This understanding has a great significance for analyzing the data with scientific precision and gaining a better insight into the meaning of voltage differences between each distinct probe. This, in turn, will lead to a deeper understanding of the operation of electrochemical cell instrumented. The following equations described are based on the discretization of electrochemical probes reported by Buhre et al. [15] and Kang et al. [16]. However, since the system is slightly different, in this work, there was an assumption in deriving these equations.

The instrumentation of the probe positioned in the IrOx layer is influenced by the reversible voltage (E^A), the electrical resistance of the IrOx/Mesh interface ($R_{el}^{Mesh/IrOx}$), the electrical resistance of the mesh itself (R_{el}^{Mesh}), mass transport losses (η_{mt}^{A}), and activation losses (η_{act}^{A}), as shown in the equation:

$$E_{A-RE_{IrOx}} = E^A + i\left(R_{el}^{Mesh/IrOx} + R_{el}^{Mesh}\right) + \eta_{mt}^{A} + \eta_{act}^{A} \quad (12)$$

The instrumentation of the probe positioned in the Mesh layer is influenced by the reversible voltage (E^A), the electrical resistance of the IrOx/Mesh ($R_{el}^{Mesh/IrOx}$) and UPP/Mesh interfaces ($R_{el}^{Upp/Mesh}$), the electrical resistance of the mesh itself (R_{el}^{Mesh}) and anodic UPP ($R_{el}^{Upp^A}$), mass transport losses (η_{mt}^{A}), and activation losses (η_{act}^{A}), as shown in the equation 13. The electric resistance between the interfaces Mesh/IrOx (blue term) increase when temperature is higher and decrease when the current density is higher [16].

$$E_{A-RE_{Mesh}} = E^A + i\left(R_{el}^{Mesh/IrOx} + R_{el}^{Mesh} + R_{el}^{Upp^A} + R_{el}^{Upp/Mesh}\right) + \eta_{mt}^{A} + \eta_{act}^{A} \quad (13)$$

To finalize the analysis of the probes positioned in the anodic chamber, it is important to understand that, according to these equations, the difference between the two results represents the sum of the electrical resistances of the anodic UPP and the interface between the UPP and the mesh, as shown:

$$E_{A-RE_{Mesh}} - E_{A-RE_{IrOx}} = R_{el}^{Upp^A} + R_{el}^{Upp/Mesh} \quad (14)$$

Located in the cathode chamber, the instrumentation of the probe positioned in the Pt/C layer is influenced by the reversible voltage (E^C), the electrical resistance of the Pt/C/GDL ($R_{el}^{\frac{Pt}{C}/GDL}$) and UPP/GDL interface ($R_{el}^{Upp/GDL}$), the electrical resistance of the GDL (R_{el}^{GDL}), cathodic UPP ($R_{el}^{Upp^C}$), mass transport losses (η_{mt}^C), and activation losses (η_{act}^C), as shown in the equation 15. The electric resistance between the layer's Pt/C/GDL (yellow term) is constant under any circumstances [16].

$$E_{c-RE_{\frac{Pt}{C}}} = E^C - i\left(R_{el}^{\frac{Pt}{C}/GDL} + R_{el}^{GDL} + R_{el}^{Upp^C} + R_{el}^{Upp/GDL}\right) - \eta_{mt}^C + \eta_{act}^C \quad (15)$$

The instrumentation of the probe positioned in the GDL layer is influenced by the reversible voltage (E^C), the electrical resistance of the cathodic UPP/GDL interface ($R_{el}^{Upp/GDL}$), the electrical resistance of the cathodic UPP ($R_{el}^{Upp^C}$), mass transport losses (η_{mt}^C), and activation losses (η_{act}^C), as shown in the equation.

$$E_{c-RE_{GDL}} = E^C - i\left(R_{el}^{Upp^C} + R_{el}^{Upp/GDL}\right) - \eta_{mt}^C + \eta_{act}^C \quad (16)$$

In conclusion, the difference between the two measurements on these two probes are the resistance of the catalyst layer/ GDL interface (constituted by Pt/C and Carbon, respectively) and the resistance of the GDL, as shown. The variation of these two results must be given by the GDL term once the yellow one is always constant over current density, water temperature, and others.

$$E_{c-RE_{\frac{Pt}{C}}} - E_{c-RE_{GDL}} = R_{el}^{\frac{Pt}{C}/GDL} + R_{el}^{GDL} \quad (17)$$

3.3. Methodology

In this subsection, the entire experimental methodology followed in each of the conducted experiments will be described. To ensure the proper insertion of each electrochemical probe, methodologies were developed with the aim of anticipating potential issues and ensuring the most suitable procedures for this type of instrumentation. Each of the conducted experiments will be summarized and detailed, along with the validation procedures for each of the assembled prototypes. Recording and documenting each step of the methodology was crucial for obtaining reliable and accurate results, as well as for identifying opportunities for improvement in this type of instrumentation. In this subsection, the following procedures will be presented in chronological order of instrumentation:

1. Prediction of problems.
2. Drilling alignment.
3. Drilling procedure.
4. Assembly procedure.
5. Summary of electrochemical probe experiences.
6. Testing procedure.

The development of this subsection constituted a learning process in which procedures were systematically enhanced and refined. The outcomes of the learning process regarding the experimental procedures are detailed below, along with all relevant and significant observations that substantiated the methods employed.

3.3.1. Prediction of problems

Initially, an analysis of possible experimental issues related to the insertion of the electrochemical probe was carried out, along with the appropriate solutions to overcome each obstacle. This step marked the outset of the electrolyzer instrumentation, facilitating the foresight of challenges and enabling meticulous planning for each experiment. Possible issues that could arise during the instrumentation of the four prototypes corresponding to each position of the electrochemical probe were analyzed. It is crucial to note that there is a significant difference between placing the probe in the anodic chamber, where there is a substantial amount of water (and oxygen), and in the cathodic

chamber, where there is less water but a production of hydrogen – a very low-density gas that can easily escape through the electrochemical probe. The drilling alignment in the flow field should ideally:

- Be conducted within the channel where the fluid circulates, ensuring that the hole does not disturb the flow walls.
- Align with the chosen hole position on the UPP, both in the prototypes of the anodic and cathodic chambers.
- Avoid the region where the silicon pads pressure holes are supported.

The hole position in both the cathodic and anodic UPP should adhere to the conditions dictated by the flow-field geometry and be situated with minimal tolerance. This assure that the probe remains sealed after assembly, preventing any movement or displacement. Considering the probe's placement, it is essential to assure the absence of leaks, whether of water or hydrogen. To achieve this, it is necessary to assess the sealing capability of the silicon pads component, as its elastic properties can provide effective sealing. Leakage tests were conducted, along with notes on potential solutions for sealing the electrochemical probe within the electrolyzer. The Table 2 consolidates the potential issues that were analyzed, which could arise, along with the proposed solutions to mitigate each of these problems.

Table 2 - Potential issues and corresponding solutions in electrochemical probe instrumentation.

Anode and Cathode chamber	
Problem	**Solution**
Flow-Field geometry drill position	*SolidEdge* modeling
UPP geometry drill position	*SolidEdge* modeling
Silicon pads' tightness	Tightness test
Drill procedure	Experimental
Different gaps of holes in each material/pipe compression	Analyze the material differences
Flow-field crack because of hole	Material testing
Tube placement	Experimental
Placing the *Nafion* inside the inner tube	Experimental
Leaks of H_2O and H_2 (tightness);	Experimental and tightness test

Therefore, a multitude of concerns were addressed, and a range of tests were conducted to predict potential issues that might arise during the instrumentation of the electrochemical probe within the electrolyzer. This step held significant importance in

mitigating potential complications. By accurately projecting the drilling alignment, we ensured a precise and well-controlled instrumentation process.

3.3.2. Drill Alignment

In summary, during the experiments, two drilling paths were performed: one in the cathodic chamber and another in the anodic chamber of the cell 1. The positioning of the electrochemical probe's terminal in the same chamber was ensured during the assembly process by incorporating the necessary drilled components for each of the experiments.

To create the drilling paths, it was essential to analyze the materials within each layer of the electrolyzer to identify the optimal drilling route. This task was accomplished using *Siemens SolidEdge*, a 3D modeling software. Through assembling the various components, the most suitable drilling trajectory for each chamber was assessed. The components drilled are listed in the Table 3, from the inside of the electrolyzer to the outside.

Table 3 - Components drilled each chamber.

Components drilled	
Cathode Chamber	**Anode Chamber**
UPP	UPP
GDL	Mesh
Flow-Field	Flow-Field
Metal Plate	Metal Plate
Silicon Pads	Silicon Pads
Terminal Profile	Terminal Profile

Table 4 and Table 5 detail all the penetrated materials along with the size of the utilized drill.

Table 4 - Characteristics of each of the layers to be drilled in the anodic chamber.

Component	**Material**	**Drill [mm]**
Anode UPP*	Titanium	±2
Mesh	Titanium	
Flow-Field	C1200HF – 76701	
Metal Plate	Inox	
Silicon Pads	Silicone	
Terminal Profile	Aluminum	

* In the middle of the holes in the geometry

Table 5 - Characteristics of each of the layers to be drilled in the cathodic chamber.

Component	Material	Drill [mm]
Cathode UPP*	Titanium	±2
GDL	Carbon	
Flow-Field	C1200HF – 76701	
Metal Plate	Inox	
Silicon Pads	Silicone	
Terminal Profile	Aluminum	

* Widen the hole in the geometry

3.3.3. Drilling procedure

To ensure the perpendicularity of the drilling line, a drilling procedure was developed to anticipate potential experimental issues:

1. Indicate the anticipated dimensions on the terminal profile and proceed with drilling.
2. Apply the projected dimensions onto the Silicon pads and then proceed with drilling.
3. Utilize the hole in the Silicon pads to identify the drilling point on the subsequent components.
4. Repeat this process for the subsequent components: flow-field followed by Mesh (anode chamber) or GDL (cathode chamber) and UPPs.

3.3.4. Assembly procedure

The assembly procedure evolved with improvements throughout each of the experiments. After multiple assemblies and disassembles, it was understood that the steps outlined below ensured a higher assembly confidence and significantly enhanced the passage through validation tests, the step forward of this procedure. The same methodology was applied to assemble the electrochemical probe in both the anodic chamber and the cathodic chamber. However, in this description, only the assembly of the prototype in the cathodic chamber (Pt/C probe) will be provided (prototype shown in the Figure 30), considering that the exact same procedure was employed, with the only difference being the replacement of drilled components with new ones. The final and improved procedure is described below:

1. Begin with the anode chamber and attach the UPP.
2. Place the anode metal plates, silicon pads, and flow-field securing them to the enclosure, then insert the gasket.
3. Assemble the cathode section: start with UPP in the enclosure.
4. Align silicon pads, metal plate, flow-field, and UPP for Cell 1, passing the tube through the hole created (starting at the terminal profile).
5. Turn and position it over the anode, ensuring the tube touches the CCM (passing through the GDL orifice).
6. Thread the *Nafion* tube inside the main tube.
7. Seal the entire electrolyzer - compress and fasten with clamps according to the standards.

Note: All components were cleaned with 75% IPA (Isopropyl Alcohol) and gloves were used throughout the assembly process to prevent contamination of the components and material properties.

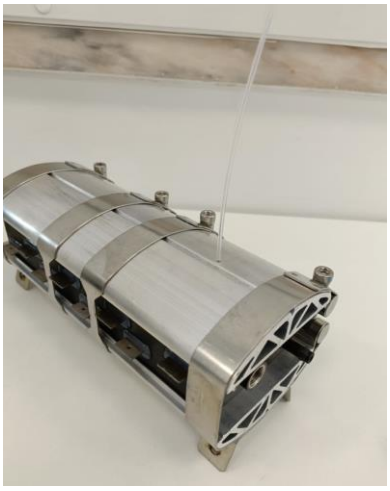

Figure 30 – Instrumented prototype of the probe positioned at the Pt/C layer.

3.3.5. Validations test procedures

Following each assembly of the instrumented electrolyzer, validation tests were conducted to ensure that the prototype was free from anomalies and provided reliable results suitable for analysis. The initial prototypes created were the ones that performed poorly in validation tests due to lack of experience in assembly and the use of outdated procedures during the early stages of instrumentation. As methodologies improved, there

was a significant reduction in prototypes failing these validation tests, underscoring the importance of conducting such analyses. This chapter outlines all the validation and calibration tests employed, along with the objectives and procedures of each test:

- Short circuit test
- Hole in PEM Membrane
- Bad assembly
- Reference Electrode Calibration

Short circuit test

The purpose of this validation test is to determine whether the electrodes of the electrolyzer electrochemical cells (UPP) are in short-circuit, either due to assembly errors or the influence of inserting the electrochemical probe. Short-circuit can occur in two different ways:

- The UPPs of each electrochemical cell in the same chamber are arranged in series, and if not assembled correctly, contact between them may lead to a short-circuit, as demonstrated in the following layout.
- If there is a hole in the PEM membrane, the UPPs of the same electrochemical cell can come into contact, causing a short-circuit due to component compression.

To detect short-circuits, an ohmmeter is employed, where the polarities are applied to the electrodes under examination (Figure 31). If conductivity exists between the polarities, it indicates the presence of a short-circuit, necessitating disassembly and reassembly of the prototype for correction.

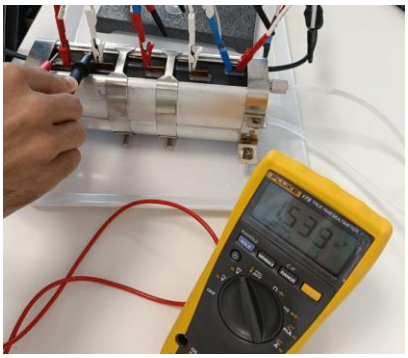

Figure 31 – Example of a dead-short test.

Leak test

In this test, we will ascertain whether there were any assembly issues with the electrolyzer or if the PEM membrane is punctured. It is crucial to ensure that the electrolyzer is properly assembled and that there are no factors influencing the results. For this purpose, it is essential to immerse the prototype in water. At the entrance of the anodic chamber of the electrolyzer, apply compressed air at 5 bar for 2 minutes, seal the outlet of the anodic chamber, and leave the outlet of the cathodic chamber open. The aim is to observe whether there is bubble formation in the immersed electrolyzer. There are two distinct indicators that the prototype might fail this test:

- If bubbles are observed at the cathodic chamber outlet of the electrolyzer, it indicates a leak in the PEM membrane, and as per procedure, the membrane undergoes the next validation test to confirm and inspect the membrane puncture.
- If bubbles are observed emerging from any of the interfaces of the electrolyzer, it signifies a deficiency of the assembly.

In some prototypes, for quicker detection after several hours of an electrolyzer operation, a leak test was conducted using nitrogen. In this validation test, nitrogen is introduced under pressure of 3 bar at the anodic chamber inlet of the electrolyzer for 2 minutes. The anodic chamber outlet is sealed, and a tube is placed at the cathodic chamber outlet. This tube is in contact with water, and if bubbles are observed, it indicates a punctured membrane.

This test served as an immediate method of verifying whether the PEM membrane had experienced a puncture. If a puncture in the membrane was detected in this test or in the previous one, the membrane was subjected to the subsequent test described.

Hole in PEM membrane

In this test, only the membranes that didn’t pass the previous test are examined to ensure that the bubbles observed in the prior test indeed originate from the membrane and not from a faulty prototype assembly. To perform this test, it was necessary to manufacture a component simulating the enclosure with the membrane but without the other components of the electrolyzer.

Reference electrode calibration

Ensuring the proper calibration of the reference electrode is highly critical to ensure the validity of the results obtained from each of the prototypes. In the experiments involving the electrochemical probe, a hydrogen reference electrode (shown in Figure 32) was consistently employed, while a known standard Silver/Silver Chloride (Ag/AgCl) reference electrode was used for calibration purposes. The Bio-Logic SAS VMP-3e Potentiostat was used to conduct the hydrogen calibration test.

Figure 32 - Hydrogen reference electrode used in the experiments.

For this reason, a calibration procedure was carried out to ensure that the hydrogen electrode is well calibrated. In the initial test conducted, the hydrogen electrode exhibited a voltage of 246mV, which notably differed from and was relatively distant from the reference voltage of the Silver/Silver Chloride electrode, that is 198 mV. Consequently, it was identified that the hydrogen electrode was not properly calibrated, prompting a recharging of the electrode. Following a 24-hour interval, a subsequent test was carried out, revealing that the hydrogen electrode now exhibited a reference voltage in alignment with that of the Silver/Silver Chloride electrode: 198 mV.

3.4. Summary of electrochemical probe experiences

Within this subsection, all prototypes developed and validated throughout the experiments are showcased. In chronological order of each experiment's execution, a summary of how the prototype experiments were conducted is provided. It is important to highlight that all the presented prototypes underwent validation and were approved following the described validation procedures, although there were several assemblies that did not pass and were subsequently reconstructed.

Figure 33 - Prototype with the probe positioned on the Pt/C layer under experiment.

Pt/C

The first prototype developed was the one with the probe positioned in the catalyst of the cathodic chamber, within the Pt/C layer. Since it was the initial instrumentation, it required more prototypes for result validation and methodology improvement. The decision to start with the instrumentation of this position of the electrochemical probe was based on two main reasons:

- The electrochemical result obtained from this probe served as validation that the instrumentation was well-executed, considering the consultation of the referenced articles and the specific features of the technology.
- There was a lower likelihood of water leakage in this chamber since it produces hydrogen and small amounts of water compared to the anodic chamber.

The Table 6 summarizes the prototypes created with the electrochemical probe positioned in this layer, along with the distinguishing characteristics of each prototype.

Table 6 - Summary of the prototypes created and validated for the in-situ instrumentation positioned on the Pt/C layer.

Pt/C Probe		
Number Montage	**Characteristic**	**Observation**
1	Dry *Nafion* tube	Without jumpers and Electrical connection terminal
2	*Nafion* tube wet in H_2SO_4 solution	
3	Influence of the electrochemical probe	
4	*Nafion* tube wet in H_2SO_4solution	With Jumpers and Electrical connection terminal

A total of 7 assemblies and disassembles were conducted to refine the created methodologies and ensure that the prototypes passed the tests. These prototypes served as validation for this type of instrumentation, and certain validation analyses were conducted exclusively using this type of instrumentation. For the execution of these prototypes, various analyses were conducted, including:

- Examination of the impact of wetting the *Nafion* tube with sulfuric acid.
- Assessment of the influence of jumpers and terminal electrical connections on the overall performance of the electrolyzer.
- Evaluation of the probe's effect on the overall performance of the electrolyzer.
- Examination of in-situ voltage and result analysis.
- Study of the temperature's influence.
- Investigation of the ON/OFF behavior.

GDL

Next, the prototypes were equipped with the electrochemical probe positioned in the GDL of the cathodic chamber. It was used the holes made in each layer of the electrolyzer during the Pt/C layer experiments, involving the alteration of the probe's position and the replacement of the GDL with one that was not perforated. The Table 7 summarize all the prototypes created and validated.

Table 7 - Summary of the prototypes created and validated for the in-situ instrumentation positioned on the GDL layer.

GDL Probe		
Number Montage	**Characteristic**	**Observation**
1	*Nafion* tube wet in H_2SO_4 solution	With Jumpers and Electrical connection terminal
2		
3		

A total of 6 assemblies and disassembles were performed in the creation of these three prototypes. Essentially there were assemblies with issues stemming from the assembly process, where the enclosure did not remain completely sealed to the electrolyzer, resulting in punctures in the *Nafion* membrane.

Mesh

Following the experiments carried out on the prototypes with the electrochemical probe placed in the cathodic chamber, we advanced to apply the instrumentation methodologies in the other two positions, specifically within the anodic chamber. We followed the same methodology as previously described but incorporated corrections based on the experience acquired from working with the cathodic chamber prototypes. Initially, the prototypes were equipped with the electrochemical probe positioned on the mesh layer, where the mesh layer itself was not perforated. The Table 8 summarizes the montages created and validated.

Table 8 - Summary of the prototypes created and validated for the in-situ instrumentation positioned on the mesh layer.

Mesh Probe		
Number Montage	**Characteristic**	**Observation**
1	*Nafion* tube wet in H_2SO_4 solution	With Jumpers and Electrical connection terminal
2		

A total of 3 assemblies and disassembles were performed to validate the obtained results.

IrOx

Following that, using the perforated components from the previous prototypes, the mesh layer was perforated, and the terminal of the electrochemical probe was positioned in the layer of iridium oxide. For result validation purposes, two prototypes were created

and thoroughly validated through the tests described in the previous chapter, as shown in the Table 9.

Table 9 - Summary of the prototypes created and validated for the in-situ instrumentation positioned on the IrOx layer.

IrOx Probe		
Number Montage	**Characteristic**	**Observation**
1	*Nafion* tube wet in H_2SO_4 solution	With Jumpers and Electrical connection terminal
2		

A total of 4 assemblies and disassembles were performed, primarily due to burrs resulting from the drilling of the mesh. These sharp points caused punctures in the membrane, compromising the entire electrolyzer' s operation. It is essential to ensure that the cutting method for the mesh follows the appropriate procedure to prevent potential membrane punctures. The instrumentation has shown that even a small burr can puncture the *Nafion* membrane.

The Table 10 provides a summary of the number of prototypes created and successfully validated in each position of the electrochemical probe.

Table 10 - Summary of the Prototypes created.

Probe Position	Number of Prototypes
Pt/C	4
GDL	3
Mesh	2
IrOx	2

In total, 20 prototypes were created, considering all the assemblies and disassembles conducted.

3.5. Tests procedure

In this chapter, the general testing procedures employed in each of the conducted experiments will be outlined. To ensure comparability among the results from these experiments, we chose to maintain a consistent testing methodology.

The electrochemical probe's potential was consistently monitored using the Bio-Logic SAS VMP-3e Potentiostat, which was operated using the EC-Lab software to

program properly the device. To inject current into the electrolyzer, the same Potentiostat was occasionally used, while in certain prototypes, the TDK-Lambda power source was employed.

The potential of each cell was monitored during each of the described stages using the Bio-Logic SAS VMP-3e Potentiostat, and in certain prototypes and tests, the Kolibrik CVM24P or the Agilent 34970A was employed, represented in Figure 34. These two devices underwent validation according to a developed procedure. In **Annex 1.**, it is possible to verify the validation of the measured potentials from both devices, confirming that the values measured throughout all experiments align with the expected.

Figure 34 – Equipment used to monitor the potentials.

The inlet and outlet temperatures of the anodic chamber, as well as the hydrogen temperature in the cathodic chamber, were monitored using custom instrumentation created with properly calibrated K-type thermocouples. In subsection 4.2.2., the calibration process and the establishment of the temperature reading circuit are detailed.

In the initial experiments, the prototypes were subjected to a high current density to activate the electrochemical cells to ensure that the obtained results align with the normal operation of the electrolyzers. Then the prototypes were subjected to a polarization curve experiment (explained in the **Annex 2.**) and then, were analyzed at the normal current operations: 4A and 8.6A. The same testing procedures were consistently followed each assembly and validation for every prototype. This fundamental methodology was established based, in general, on the following steps:

1. Start the water supply at 60ºC for 1 hour.
2. Run at 8.6A for 3 hours to activate the electrochemical cells.
3. Perform polarization curve.
4. Run at 8.6A for 2 hours and record potential values.
5. Run at 4A for 2 hours and record potential values.

3.6. Results and Discussion

3.6.1. Summary of the Experiences

The purpose of this subchapter is to summarize all the experiments conducted, which will be the subject of analysis and discussion. The application of the established testing methodologies allowed us to carry out numerous experiments, comparisons among electrochemical probes and validation between each prototype. In general, the comparisons and analyses to be discussed in the following subchapters are summarized:

1. Overall Influence of the Probe in-situ Instrumentation
2. Validation of the Prototypes
3. Decomposition of the Cell 1 Potentials
    a. Polarization Curves (PC)
    b. Operating Currents (4A and 8.6A)
4. On/Off
    a. With Water Flow
    b. Without Water Flow
5. Influence of the temperature
    a. Electrochemical Cells
    b. Electrochemical Probes
6. Cyclic Voltammetry (CV) of the Pt/C Probe

3.6.2. Overall Influence of the Probe in-situ Instrumentation

To analyze the results obtained from the experiments, it is important to ensure that this type of instrumentation does not have influence in the normal operation of the electrolyzer. To achieve this, two identical electrolyzers were compared, with all components having the same materials, except that one of them has the in-situ instrumentation added: the probe positioned in the catalytic layer of the cathodic chamber of the electrolyzer (Pt/C). Figure 35 shows a polarization curve test (see **Annex 2.** for clarification) with the water at 60°C conducted on both electrolyzers, with the total potential represented versus the current density.

It is possible to observe that both electrolyzers behave in a very similar manner, with no significative differences. This leads to the conclusion that the additional instrumentation does not affect the normal operation of the electrolyzer., and the results from the conducted tests can be considered reliable.

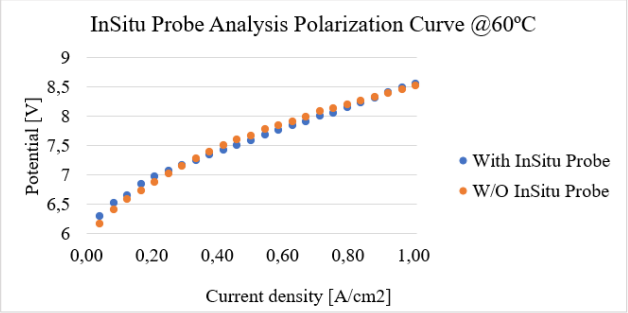

Figure 35 - Comparation between a standard electrolyzer and an instrumented one

3.6.3. Validation of the Prototypes

To confirm that the tests conducted on each of the different prototypes were subjected to the same operating conditions and it can be compared to each other, an analysis of the total cell 1 potential and the total electrolyzer potential was carried out for each prototype. The different prototypes were subjected to several cycles of assembly/disassembly, as a result, the components of each prototype were exposed to different operating hours before the experiment under analysis, which could potentially impact the results. In Figure 36, this analysis can be seen for a current of 4A, where it is evident that the total cell 1 potentials and total electrolyzer potentials are very similar in the different prototypes. The same comparison was made, but for an operating current of 8,6A, once again highlighting the consistency of the results. The Table 11 displays the maximum standard deviation in each of the experiments. Based on this analysis, we have the support that the results presented throughout the report can be compared with confidence since the electrolyzers are under the same operating conditions, with the highest standard deviation being only 5.81 mV.

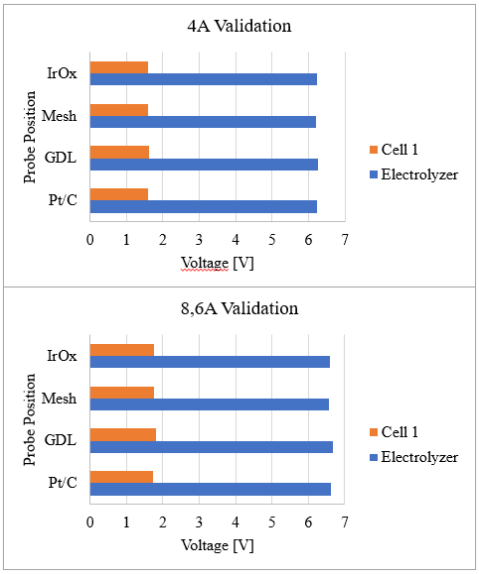

Figure 36 - Total electrolyzer potential and potential of the cell 1 each experiment at 4A and 8.6A

Table 11 – Potential total and Cell 1maximum standard deviation from the experiments at 4A and 8.6A

	Current [A]	Maximum Standard deviation [mV]
Electrolyzer	4	3.23
	8.6	5.81
Cell 1	4	2.42
	8.6	4.66

3.6.4. Decomposition of the Cell 1 Potentials

In this subchapter, the results of the in-situ electrochemical instrumentation of the electrolyzer will be presented and discussed. In the analysis, these results will be examined in the polarization curve test, followed by an assessment of the typical operating currents to understand the influence of each layer on the currents of greater interest in the project. In the polarization curve experiences, the current was increased by 0.5A every 2 minutes (see **Annex 2.** for clarification). To analyze the results, an average of the last minute of each current step was calculated to ensure that the potential had stabilized. The temperature of the water supply was 60 ºC, once it is the average operating temperature of the electrolyzer.

a) Polarization Curves

Through the conducted instrumentation, it is possible to decompose the potential of the electrochemical cell 1 into contributions from each of the layers where the probe is positioned. Figure 37 presents the polarization curve results for each of the prototypes and the obtained potential values for each layer. Although the tests were conducted under

the same conditions, slight differences existed in the total voltage of cell 1 (as shown previously), so we opted to present the results in relation to each of the experiments to ensure greater accuracy. The y-axis represents the measured potential, and the x-axis represents the current density relative to the area of cell 1 of the electrolyzer. Table 12 shows the slope of each curve, representing the slope value at each probe prototype and in the total cell curve each prototype.

Anodic Chamber – Probes Positioned in mesh and IrOx

There is evidence that these probes concentrate higher potential values in relation to the cathodic potential values and the total of cell 1. These results would be expected since this is where the electrolysis of water occurs, and potential is required to break this molecule. These results provide valuable insights regarding the real oxidation potential to which layer is exposed - from approximately 1.43V to 1.55V. These findings assist in conducting more accurate corrosion experiments (for example), allowing them to apply the appropriate potential under normal operating conditions and perform more precise experiments.

The differences between the results of the two anodic probes are not so significant, with the potential of the probe positioned on IrOx being slightly higher. This difference is due to the potential of the resistance caused by UPP and the UPP/Mesh interface (see subchapter 3.2), but it does not appear to be a significant difference. Because of that, there is evidence that the mesh has a slightly influence on the overall electrolyzer potential but there are no noticeable significant differences that could negatively impact the electrolyzer.

Comparing the increase of potential due to the increase of the current density of the two probes to the real slope of the total potential of cell 1 (represented in Table 12), the slope of the anodic probes does not significantly influence the total slope of the cell, indicating that this chamber does not have a big impact on the slope of the cell 1, unlike the cathode chamber.

Cathodic Chamber - Probes Positioned in Pt/C and GDL

In the cathodic probes, it is visible that they exhibit negative potentials, which is expected since there is a reduction process in this chamber, with the reduction of hydrogen ions (see subchapter 3.2).

In the Pt/C layer there is evidence that the current density varies from 0 to approximately 0.35 A/cm2, demonstrating that it is happening the reduction of hydrogen ions in this layer. It is possible to identify the reduction voltage value each current density applied to the electrolyzer, which gives important insights about the real voltage that this layer is subjected. These results help to perform more precise experiments, being able to apply the correct potential that this layer is exposed in the normal operating conditions.

Despite of being on the cathode chamber, at low current densities, the probe positioned at the GDL yielded positive potential values. One explanation for this result, is that the reduction is indeed occurring in the catalytic layer of Pt/C also in the GDL, but only at higher current densities, despite GDL being a passive layer. So, at current densities from, approximately 0.4 A/cm2 the impact of the catalyst layer polarization is observed at the GDL probe position, demonstrating that there is reduction of the hydrogen ions on this passive layer. Because of that there is evidence that the activation parcel in the GDL has a big influence in the electrochemical behavior of the electrolyzer. Once the GDL is a passive layer, this result indicates that electrochemical reduction reactions occur at high current densities, demonstrating that is crucial to do experiments over time at specific current densities to evaluate the stabilization of the potential value at GDL and quantify the activation term.

The slopes of these probes, calculated and presented in the Table 12, highlight that the total slope of the electrochemical cell is strongly influenced by the cathodic layers, especially in the Pt/C layer, where the slope of the result of this probe does not differ much from the actual cell slope (85%). This result is in line with the discoveries from the article [15].

It is important to note that these results are in line with the findings reported in the literature [14-17], where the anodic chamber exhibits higher (in the absolute value) potential values, and the cathode potentials values are negative representing lower absolute potential values.

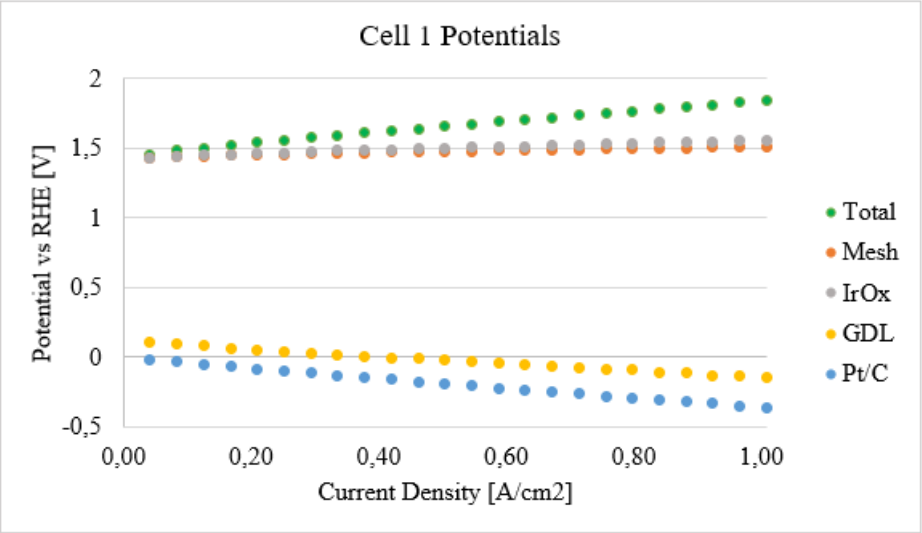

Figure 37 - Decomposition of the Cell 1 Potentials under Polarization curve

Table 12 - Slope of the polarization curve each probe position.

Slope [V/(A/cm2)]		
Probe Position	**Cell 1 Total (100%)**	**Probe**
Pt/C	0.49	-0.42 (**85%**)
GDL	0.51	-0.31 (**59%**)
Mesh	0.46	0.09 (**20%**)
IrOx	0.45	0.15 (**33%**)

b) Operating Currents (4A and 8.6A)

To analyze the behavior under normal operating currents, experiments were conducted following the same methodologies for each of the prototypes at 4A and 8.6A (temperature water supply at 60 ºC). Table 13 shows the potential influence at each of the probes in relation to the total potential of cell 1 (for example, the voltage reading of the probe positioned on Pt/C represents 7.11% of the total potential of cell 1).

The probes positioned in the anodic chamber have a greater influence on the total potential value, which is also evident in Figure 37. As the current increases from 4A to 8.6A, there is an increase of the potential influence caused by the layers of the cathodic chamber, and a consequent decrease of the influence caused by the anodic layers. This fact was also confirmed in Figure 37 since the slopes of the potential in the polarization curves of the probes positioned in the cathodic chamber have a higher slope in absolute value than those positioned in the anodic chamber.

All potential results at each of the probes stabilize rapidly at the values shown in Figure 38 (quick stabilization at 4A in the mesh probe experiment), except for the GDL probe. In this probe the potential starts negative and stabilizes at a positive value over

time and it is influenced by the lifetime of the electrolyzer, as demonstrated in the Figure 39. So, there is evidence that the operating hours are highly significant in achieving the stabilization of the potential of the probe located at the GDL. In all experiments, this phenomenon occurred, and instead of having a negative potential at 4A, the results showed that the potential stabilize at a positive current (representing approximately 10% of the total voltage of cell 1). In Figure 39, the results in different electrolyzers with the injection of 4A and different hours of operation are shown, where the electrolyzer with fewer hours of operation starts at a negative potential and increases over time. After 15 hours of operation, it stabilizes at approximately 0.16V, which corresponds to 10.08% of the cell 1. This result clearly indicates that at a 4A current level, there are significant resistances associated with this layer, and since the activation component is the only one with a reversed sign in the equation (subchapter 3.2), there is evidence that this term has a significant influence. At 8.6A, the potential remains positive but stabilizes at a value close to 2.3% of the total cell voltage. These results, both the positive potential value and the stabilization phenomenon, deserve special attention to study the physical phenomena behind this behavior since the compression of the GDL has a significant influence on improving the performance of this component. It is important to get a better understanding in the optimal operating conditions to reduce unnecessary resistances, especially in this layer that has a passive behavior in the electrochemical reaction.

Comparing the two probes on the anode side, the mesh probe exhibits a higher potential percentage at 4A and a lower one at 8.6A, which is not corroborated by the equations shown (subchapter 3.2). However, the differences between them are small.

Table 13 - Influence of each Probe Potential in the total potential of the cell 1

Potential Influence of the Cell 1 [%]		
Probe Position	**4A**	**8,6A**
Pt/C	7.11	13.68
GDL*	10.08	2.3
Mesh	93.73	85.27
IrOx	92.46	86.34

* - the probe positioned at GDL has a different behavior standard comparing to the other probes: the potential starts negative and stabilize on positive value over time (in 40minutes)

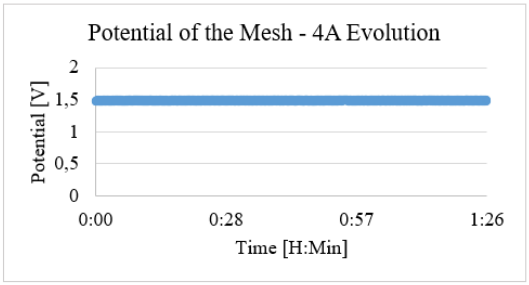

Figure 38 - Stabilization of the potential result on Mesh Prototype

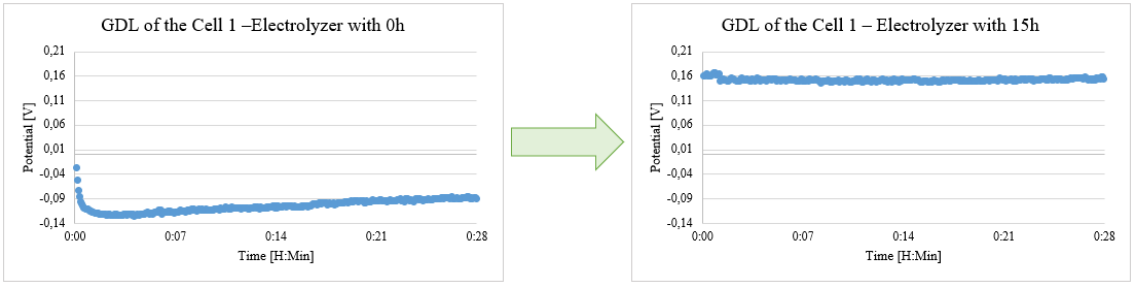

Figure 39 - Stabilization of the potential in the GDL Prototype (Comparison between electrolyzer lifetimes)

3.6.5. On/Off

The behavior of the electrolyzer was tested when it was stopped during its operation, i.e., when the current injection was discontinued – OCV (open circuit voltage). To do this, an analysis was conducted while maintaining the water flow, and in another analysis, the water supply was cut off.

a) Global Electrolyzer

Figure 40 presents a result of the On/OFF test with continuous water flow. The behavior in all experiments was very similar to the behavior shown below. This test is highly dependent on the activation level of the electrochemical cells and the tests conducted beforehand.

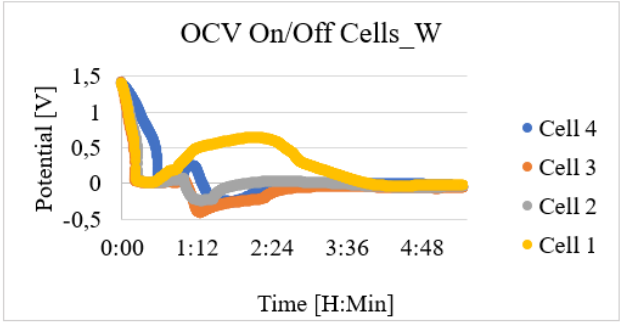

Figure 40 - Cells potential in On/Off experience with water flow at 60ºC

Figure 41 shows a result of an On/Off test without any water injection. In this test, there was significant variability among different experiments, and it was not obvious about the cell's reaction pattern to the cessation of current injection and water supply. After several hours, approximately 8 hours, there is stabilization of the potential each cell near to 0V, but before that it was always inconstant in every test conducted.

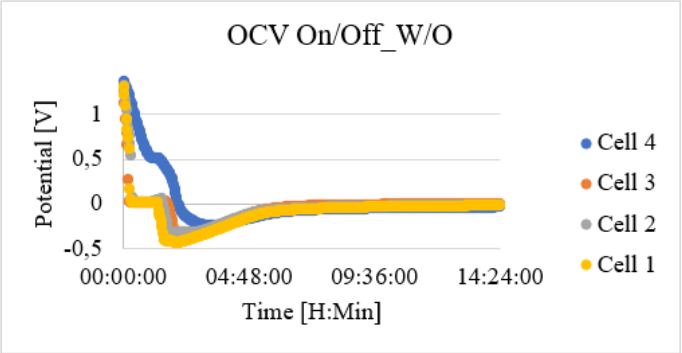

Figure 41 - Cells potential in On/Off experience without water flow

3.6.6. Influence of the Temperature

The electrolyzers were tested at temperatures of 25°C, 40°C, 60°C, and 80°C to quantify the temperature influence on the electrolyzer's operation. A polarization curve was conducted in each test, where the current was increased by 0.5A every 2 minutes (see **Annex 2.**). To analyze the results, an average of the last minute of each current step was calculated to ensure that the potential had stabilized. This procedure was followed for the different temperatures.

a) Cells

In Figure 42, it is possible to observe the potential results for each of the electrolyzer's cells. It is noticeable that the Cell 1 has a higher potential than the other cells. As the temperature increases, it is possible to recognize that the potential in each of the cells decreases, and the difference between them becomes smaller. The increase of temperature benefits the reaction of splitting water molecules by reducing resistances and requiring lower potentials for the electrolysis process.

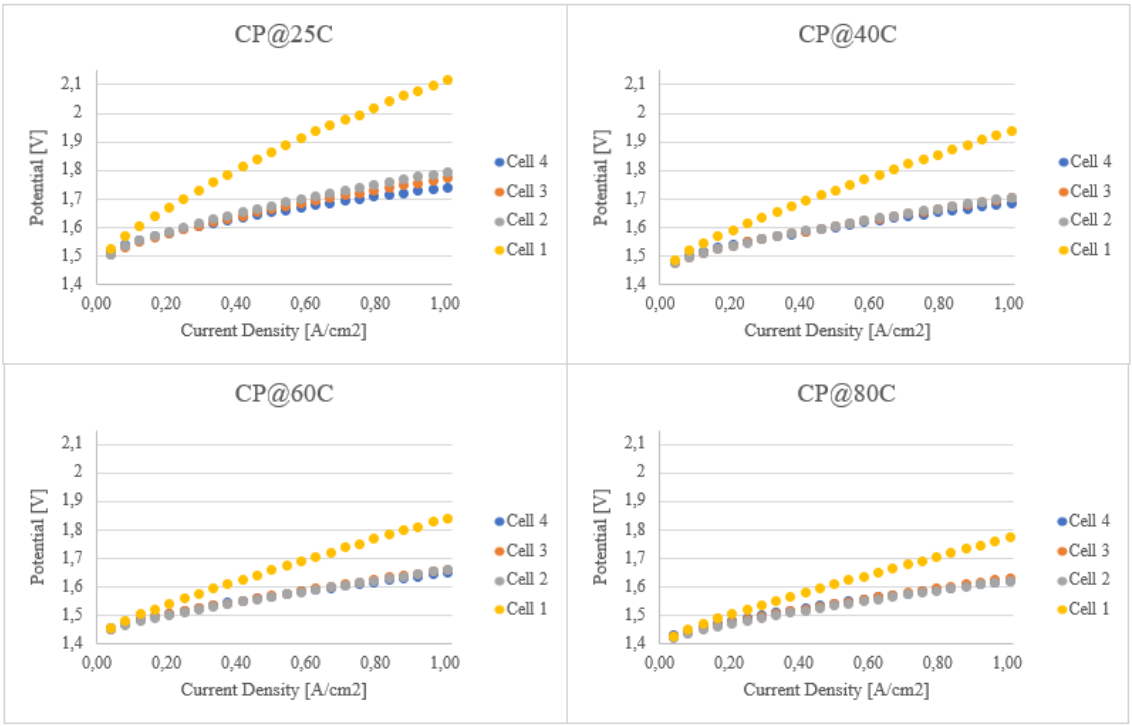

Figure 42 - Potentials of the electrolyzer cells due different water temperatures supply at polarization curve experiment.

b) Probes

Figure 43 presents the results that compare all the potential measured in each of the electrochemical probes with temperature variation. The y-axis indicates the percentage of potential obtained relative to the total voltage of Cell 1, and the x-axis corresponds to the current density of Cell 1. Across all the graphs, it is evident that with an increase in current density, there is a growing influence of the cathode chamber and a consequent decrease in the influence of the anode chamber. It is also noticeable that there is a larger potential difference between 25°C and 40°C compared to the other temperatures.

Analyzing the Pt/C probe's result, it becomes apparent that as the temperature increases, this layer gradually exerts less influence on the total cell voltage. With this observation, it is evident that, despite the improvement in the kinetics of the electrolysis reaction with the increase in temperature, there are also two phenomena that increase the resistance of the system: the creation of more gaseous hydrogen and the creation of more gaseous oxygen. This increased production causes resistances capable of considerably affecting the efficiency of the process, and through this result, it is possible to estimate that there are more resistances on the anodic side compared to those created on the

cathodic side. Examining the GDL probe's result, there is a phenomenon captured between 60°C and 80°C, where it deviates from the pattern observed in other temperature increases. This probe also shows the phenomenon of positive voltage at low current densities, as explained earlier. In the graph of the IrOx probe, it is possible confirm the decrease of the probe influence due higher current densities. When the temperature increases there is bigger influence of this probe on the cell potential. The same trend is observed in the mesh probe, where these potentials exhibit slightly less influence on the total cell voltage than the IrOx probe.

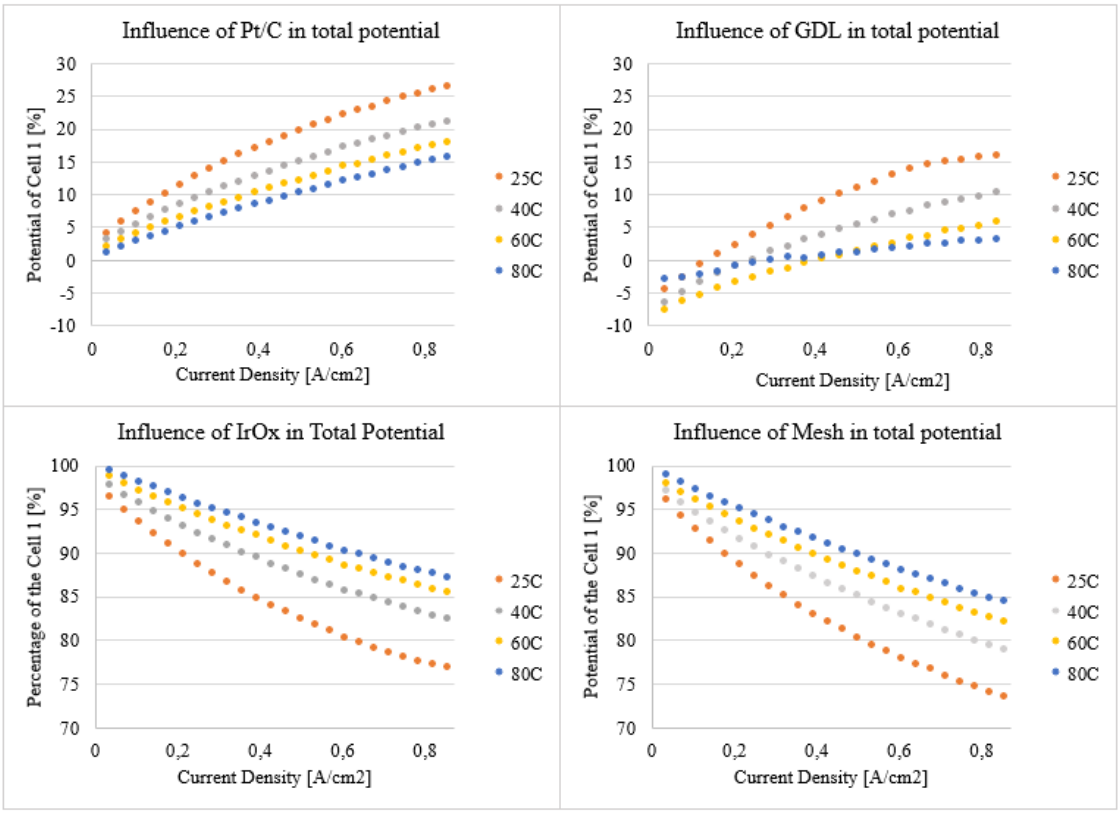

Figure 43 - Influence of the Probe potential in total cell 1 potential due different water temperature supply at polarization curve experiment

3.6.7. Cyclic Voltammetry (CV) of the Pt/C probe

It was possible to obtain cyclic voltammetry (explained in the **Annex 2.**) curves in Pt/C catalyst layer to evaluate electrochemical areas at different speed test, testing to a temperature water supply of 60 ºC. The cyclic voltammetry obtained in the experimental tests shown in the Figure 44 is identical to the Pt/C curve obtained by the scientific experiment [14], validating the accuracy of the results obtained in a less controlled environment.

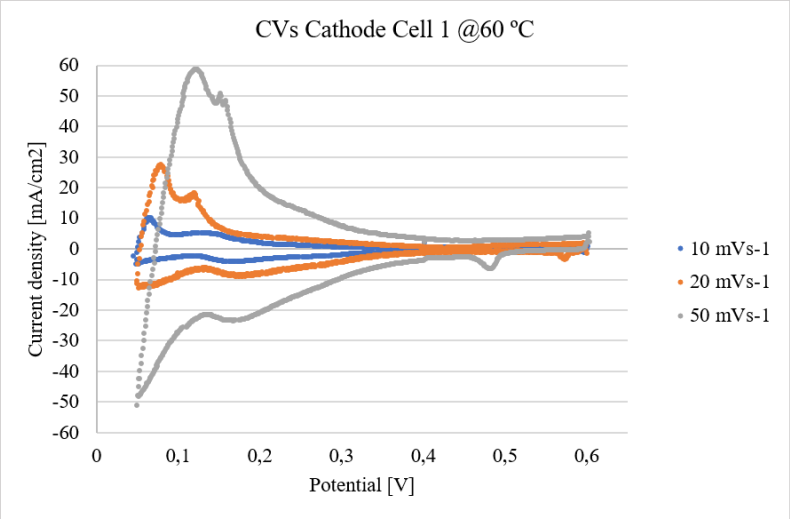

Figure 44 - Cyclic Voltammetry experience in the Pt/C Prototype

3.7. Conclusions on Electrochemical Instrumentation

Through the implementation of this in-situ electrochemical instrumentation, all proposed objectives have been successfully achieved. The primary goal of creating and applying the necessary methodologies and procedures to develop the presented prototypes has been accomplished. The results from different prototypes have been validated to ensure their reliability and correspondence to the actual operation of the electrolyzer, without any anomalies. This provided a better understanding and characterization of the electrolyzer's operation, highlighting the importance of this instrumentation.

Regarding the results, it has been possible to decompose the potentials of cell 1 into the different contributions from each layer. Additionally, by referencing the literature that also applied a *Nafion* tube for ionic conduction, it was confirmed that the results align with existing literature and equations. This work has underscored that the cathodic chamber's influence increases with higher current levels, and temperature significantly impacts the electrolyzer's voltage values. An irregular phenomenon in the behavior of the probe positioned in the GDL has been discovered, which deserves further investigation to improve this component and identify areas for improvement.

As future work, it would be highly interesting to conduct similar analyses using different components in the various layers and assess the positive or negative impacts of these changes. Another suggestion is to apply this same instrumentation to other cells within the electrolyzer to analyze their behavior and identify trends for each cell.

4. Temperature In-Situ Instrumentation

4.1. Applications

The objective of this instrumentation is to assess and characterize the temperature profile inside the flow-field of the anodic chamber of the electrolyzer. As elaborated in Chapter 2, this component plays a critical role in uniformly distributing water to all electrochemical cells and evacuate the produced oxygen + water from the electrolysis process out of the anodic chamber. This in-situ instrumentation is of utmost importance to understand the actual temperature to which each electrochemical cell is exposed and to determine whether there is a uniform distribution across the four electrochemical cells or if there is a significant temperature difference between electrochemical cells and/or within the same electrochemical cell. Ideally, each electrochemical cell would be subjected to the same temperature and operate under identical operational conditions.

To obtain this type of reading, it is essential to create a prototype that allows the placement of thermocouple (**Annex 3.**) in specific positions within the anodic flow-field, enabling temperature measurements at defined points. For this purpose, two different instrumentation approaches were employed to determine which type of prototype yields more reliable and trustworthy results for subsequent analysis:

1. Using empty space between UPP and enclosure
2. Doing a hole in the electrolyzer components

To monitor the inlet and outlet temperatures of the anodic chamber and the outlet of the cathodic chamber, three thermocouples were installed, and these sensors and setup were employed in both in-situ instrumentations. In this chapter will be explained the definition, assembly, validation process and test procedures of the thermocouples for both instrumentations.

4.2. Outline Thermocouples

4.2.1. Characterization

Through this setup, it becomes possible to characterize the inlet and outlet temperatures of the water in the anodic chamber, as the temperature of the hydrogen

exiting the cathodic chamber, as shown in the Figure 45. It is imperative to accurately define and calibrate these sensors to ensure that the values recorded in each experiment correspond to the actual fluid temperature values, thereby ensuring the reliability of the results. This chapter will present the methodology, calibration, and precautions taken during the installation of these sensors, which were utilized in both different in-situ instrumentations conducted.

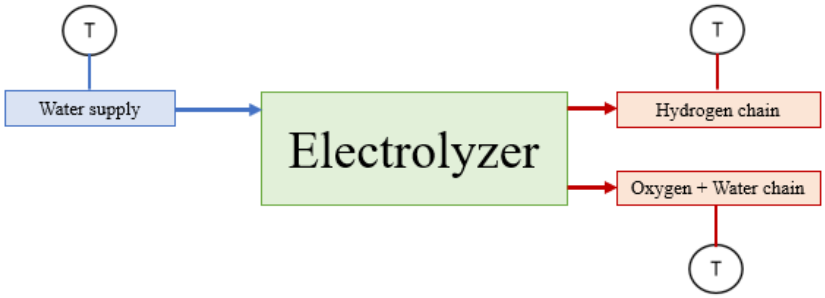

Figure 45 - Schematic about the position of the thermocouples in the outline circuit

4.2.2. Calibration Process

Prior to their integration into the circuit, all three sensors underwent a calibration process to ensure accurate temperature readings. The equipment Agilent 34970A was employed for connecting to Type K thermocouples used in this process.

The thermocouples were placed in the same container with initially room-temperature water, along with a properly calibrated thermocouple, as shown in Figure 46. It was recorded the differences that each of the three thermocouples had compared to the reference thermocouple. After the calibration at room temperature, the water was heated to approximately 50°C, and the differences between the thermocouples were recorded, which were found to be identical to those from the previous calibration.

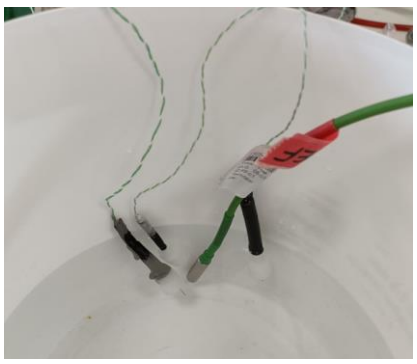

Figure 46 – Calibration of the thermocouples

In this process, the polarity of the electrical connections of the thermocouples to the Agilent equipment was also tested to ensure that the thermocouples respond effectively to temperature increases or decreases.

4.2.3. Circuit assembly

To assemble the circuit, we opted to position the thermocouples as close as possible to the inlet and outlet points. This choice ensures that we can obtain the most accurate temperature readings with minimal thermal losses. Additionally, to prevent thermal losses, we insulated the pipes using insulating tubing before the water or hydrogen passed through the sensors. The Figure 47 represents the external circuit built and used in all conducted tests.

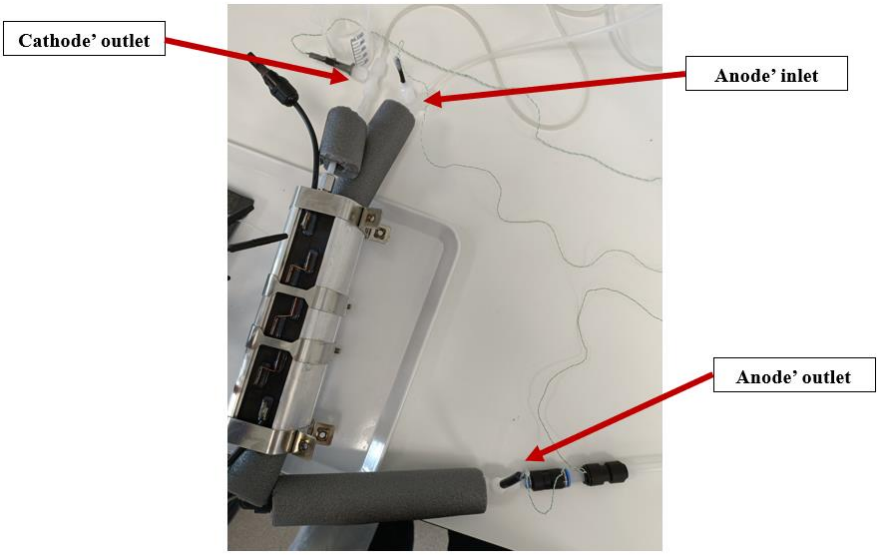

Figure 47 - Outline circuit created.

4.3. UPP Instrumentation

4.3.1. Characterization

In this instrumentation approach, the gaps between the "plastic" casing and each of the UPPs of the electrochemical cells were employed. In a standard electrolyzer this empty space is filled with a silicone, which, in turn, has the objective of preventing the water within the anodic chamber from escaping to the exterior of the electrolyzer. Therefore, through this instrumentation, the aim is to insert the thermocouple before

applying the sealant and thereby position the temperature sensor's tip within the defined flow-field channel to obtain the water temperature at that location, as shown in Figure 48.

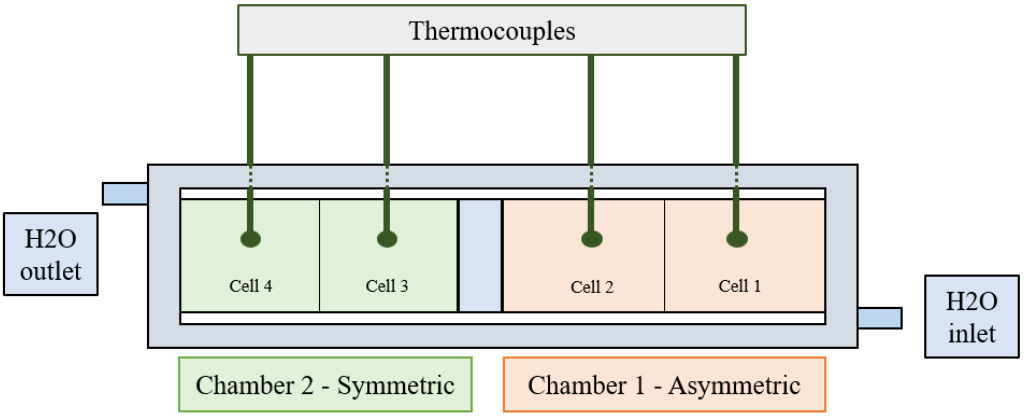

Figure 48 – Schematic about the position of each temperature probe

Initially, several challenges were anticipated during the implementation of this instrumentation, including:

- Water leaks
- Short circuit between the thermocouple and UPP
- Damage to the thermocouple wire
- Adhesion of the sealant to the thermocouple wire
- Proper placement of the thermocouple within the flow-field channel
- Variation in assembly pressure

This type of instrumentation can lead to significant pressure variations within the components. The insertion of the thermocouple creates a thickness that is unavoidable in this type of instrumentation, which can potentially impact the electrochemical core, as illustrated in Figure 49.

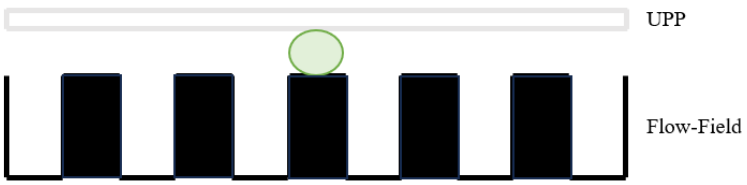

Figure 49 – Schematic about the compression problem

4.3.2. Summary of the Prototypes

To create the prototypes, specialized assembly methodologies were developed to make their construction feasible, and various precautions were taken to anticipate potential issues. All prototypes underwent the validation tests described in Chapter 3.6.3., and if they did not pass the test, they were disassembled and reassembled to satisfy the standard operating requirements. The potential of each electrochemical cell was followed using the Kolibrik and the Agilent equipment was used to measure the temperatures.

First, and to validate this type of instrumentation, it was made a prototype where only one thermocouple was inserted – in the middle of the cell 1. Next, one thermocouple was inserted for each electrochemical cell (as show in the Figure 50), and care was taken to ensure that each thermocouple was positioned in the last three channels of each electrochemical cell to reduce the effect of pressure variation and minimize the phenomenon demonstrated in Figure 49. Being in the last 3 channels, the thermocouple wires offer less resistance to the compression of the electrolyzer, improving the instrumentation. The main goal was to insert the thermocouples in the same electrochemical area of each cell to gain a better confidence about the comparison between the temperature reading. However, due the assembly methodology applied, there were always an uncertainty about the location of the thermocouples, which is represented in the schematic.

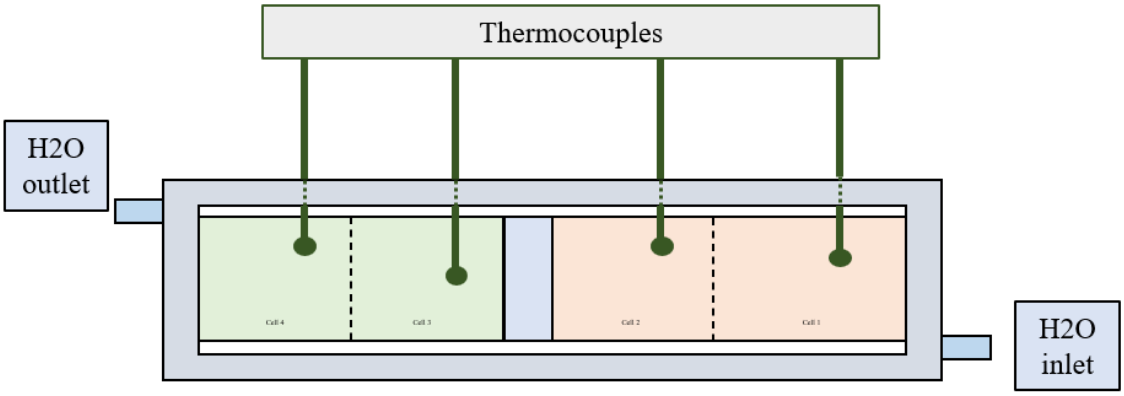

Figure 50 – Schematic about the real position of the thermocouples

The Figure 51 shows the Prototype 1 under experiment. The Table 14 provides a summary of all the prototypes, detailing the distinctive features of each one.

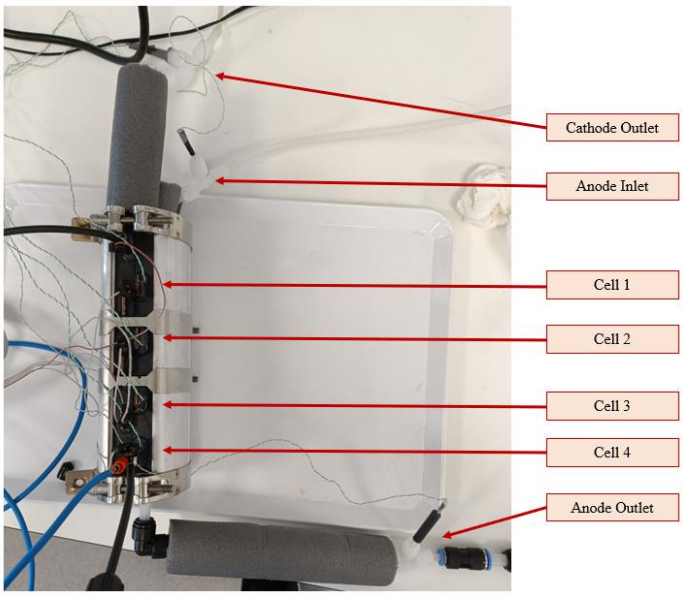

Figure 51 – Protype 1 under experiment

Table 14 - Summary of the Prototypes done using the UPP Gap instrumentation.

Prototype number	Observation
1	Insertion of each thermocouple in the middle of each cell
2	Insertion of each thermocouple in the last three channels of the cell
3	Same conditions of the Prototype number 2
4	Same conditions of the Prototype number 2
5	Same conditions of the Prototype number 2

4.3.3. Results and Discussion

In this subchapter, we will first analyze the inlet and outlet temperatures of the electrolyzer when water is introduced at different temperatures and subjected to a polarization curve (see **Annex 2.**). The results of the last two prototypes, which achieved greater consistency between them, will be discussed.

4.3.3.1. Outlet Circuit

The electrolyzer was exposed to various inlet temperatures during a polarization curve test. The inlet temperatures at the anode and the outlet temperatures at both the anode and cathode were recorded for each experiment.

Figure 52 displays the results of the 60 °C polarization test. Additionally, after completing the test, water inflow into the electrolyzer was maintained to observe the temperature evolution under these conditions, which represent the electrolyzer's normal operational parameters. It can be concluded that:

- The results indicate that high current densities result in lower observed temperature differences between inlet and outlet at the anode side.
- At low current densities, the difference represents about 15% of the inlet temperature and at higher current densities represents 8%.
- The energy dissipation due to water temperature has more influence than the heat generated by the chemical reaction. The results show that at higher current densities there is a tendency to equalize the heat loss and the heat generated by the chemical reaction transforming this difference to 0 ºC.
- Without any current it is possible to observe the real heat' dissipation at 60 ºC. Represents a substantial difference - around 10 ºC.

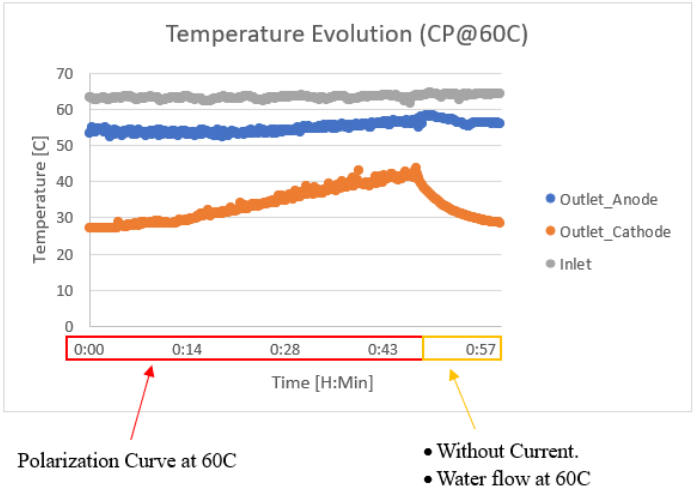

Figure 52 - Outlet Temperature Evolution under polarization curve experiment

Figure 53 displays the results of the four tests conducted at four different water inlet temperatures, all with the same flow rate of 20 mL/min (standard). From these results, we can draw the following conclusions:

- Only at 25 ºC the temperature of the anode' inlet is lower than the temperature of the anode' outlet.

- At 45 ºC the temperature' difference between inlet and outlet of the anode is close to 0 ºC at high current densities; Seems that the energy' dissipation of the electrolyzer is almost equal to the heat produced by the chemical reaction at higher current densities.
- Evidence that at higher temperatures the dissipation of energy has more influence than the energy produced by the chemical reaction.

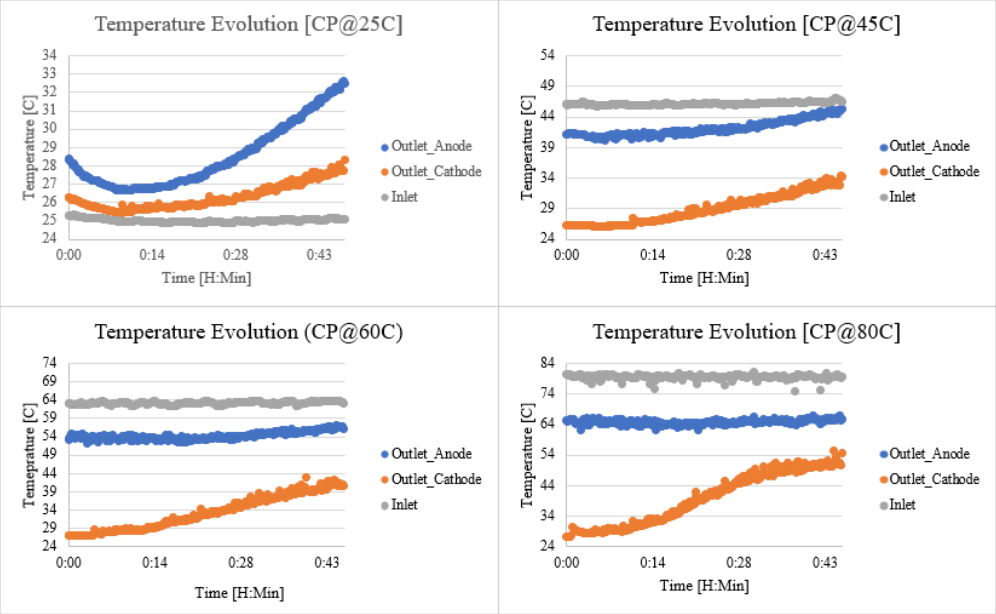

Figure 53 - Outlet circuit temperature evolution under different water supply temperature (polarization curve experiment)

The graphic represented in the Figure 54 illustrates the differences between the water temperature at the anode's inlet and outlet, allowing us to discern the heat dissipation or heat gain produced by the electrolyzer. It is evident that:

- The temperature differences between the inlet and outlet of the anode only increase at 23 ºC once the chemical reaction produce heat.
- The anode temperature differences are higher at higher temperature conditions. Can be explained by the heat transfer of the electrolyzer to the environment that has more influence than the heat produced by the electrochemical reaction.

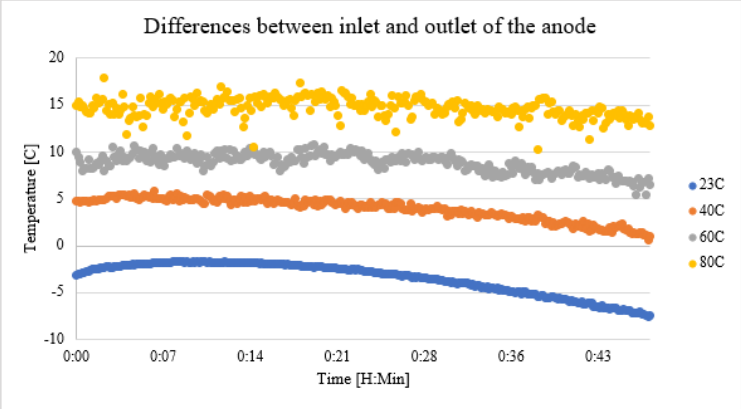

Figure 54 - Differences between inlet and outlet of the anode at different water supply temperature under polarization curve experiment

4.3.3.2.Potential Analysis

Now, to assess whether this type of instrumentation affects the normal behavior of the electrolyzer, the potentials of all cells in the electrolyzer were monitored. In Figure 55, we compare the potentials of a standard electrolyzer with the potential of the 5th prototype created using this type of instrumentation. It is possible to understand that this type of instrumentation has a significant influence on the overall behavior of the electrolyzer since the potentials of the cells behaves differently from the standard and only the Cell 4 remained constant over time. This phenomenon can be explained by the different compression to which these prototypes are subjected, as the insertion of the thermocouples creates a thickness that affects the compression of the electrochemical core and, consequently, the distribution of water in the flow-field.

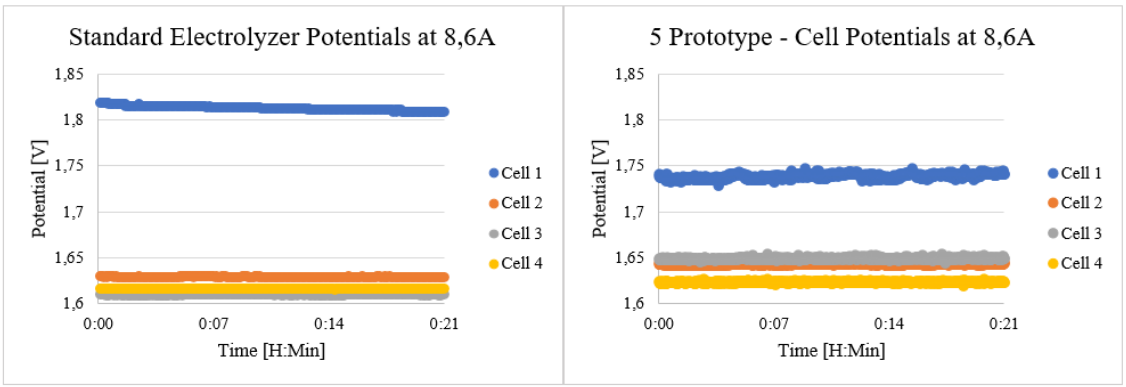

Figure 55 - Comparison between Cell Potentials in a Normal and 5 Prototype under 8.6A

4.3.3.3.Temperature Analysis

In Figure 56, it is possible to evaluate the temperature readings obtained from each of the thermocouples in prototypes 4 and 5, where no current is applied, and temperature water inlet of 60°C. This analysis allows us to assess the positioning of the thermocouples. First, it is noticeable that the inlet and outlet temperatures in both experiments are very similar. However, in both prototypes, the water temperature in the fourth cell showed values below the outlet temperature. These results may be influenced by imperfect compression caused by the interference of the thermocouple wires with the compression.

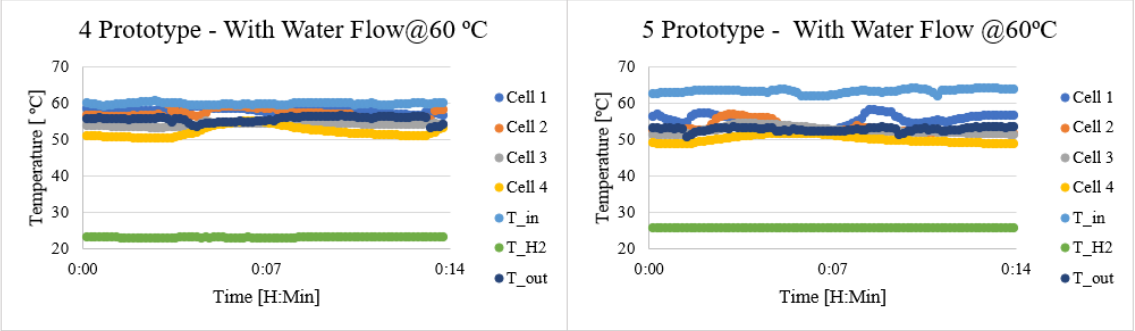

Figure 56 - 4 Prototype and 5 Prototype temperature probe results due water inlet at 60 ºC.

Figure 57 shows the temperature readings when the electrolyzer is operating with a current injection of 8,6A. It is evident that the temperatures in cell 1 are significantly higher than the inlet temperature of the electrolyzer. In all cases, there was inconsistency in the temperature readings of cell 1, whereas the temperatures in the other cells remained relatively stable within a range between the inlet and outlet temperatures. This high temperature in cell 1 may be attributed to the proximity of the UPP to the thermocouple or the positioning of the thermocouple, where there is lower flow in this cell and a concentrated heat source near the temperature probe. This type of instrumentation is not reliable for the intended purpose due to the significant influence of the imperfect compression of the electrochemical core caused by the insertion of thermocouple wires.

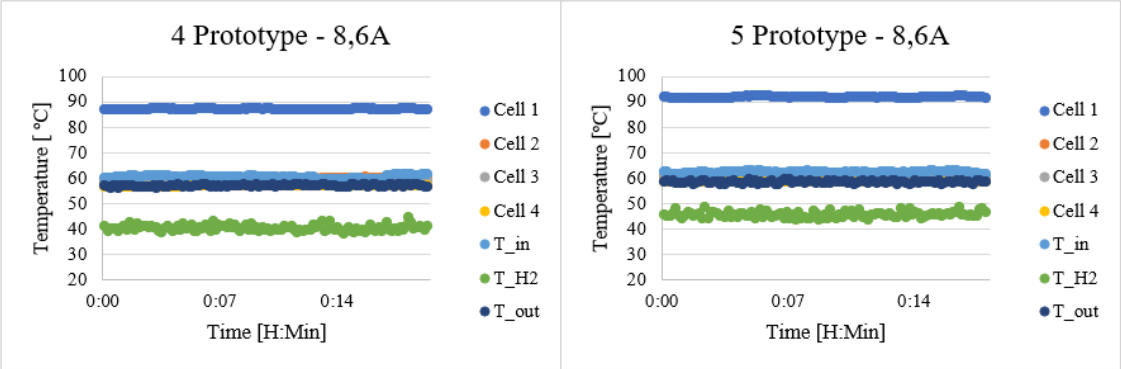

Figure 57 - 4 Prototype and 5 Prototype temperature probe results due water inlet at 60 ºC and 8,6A current.

4.4. Flow Field Hole

4.4.1. Characterization

In this instrumentation approach, holes were created in the electrolyzer components to allow placement of the thermocouple terminal in one of the flow-field channels, thus capturing the temperature readings in the electrochemical cell. To achieve this, a drilling methodology for the necessary components had to be developed, while also anticipating several potential issues that could arise from this in-situ instrumentation. Some of the anticipated problems in this instrumentation include:

- Water leakage
- Thermocouple dislodgment from the designated position
- Thermocouples short-circuit with the UPPs
- Adjustment of clearances for the drilled component holes
- Non-linearity in the alignment of holes across various components

Several measures were taken to prevent these potential issues. Among them, thermal tubing was glued to protect the two thermocouple wires as they pass through the holes, as it is possible to observe in Figure 58. Additionally, one of the components was secured with super glue after assembly to ensure the sensor remained in place.

Figure 58 - Thermocouple with thermic tube

First, using the model of the electrolyzer in software *Siemens SolidEdge*, the hole positions in each of the components were defined to ensure that the thermocouple was positioned in the central channel of each of the electrochemical cells. Figure 59 illustrates the drilling process of the flow-field after the locations were determined.

Figure 59 - Drill process of the Flow-Field chamber 1

After drilling all the components, the thermocouples were inserted, and the electrolyzer prototypes was assembled, as shown in Figure 60. Due to the insertion of the thermocouples, it was not possible to ensure a standard clamping force because of the inability to place the press on the electrolyzer. This could have an impact on the results, which will be discussed.

Figure 60 - Assembly process of the 2 Prototype

4.4.2. Summary of the Prototypes

The summary of experiments conducted using this type of instrumentation is presented in Table 15. Two prototypes were tested: one with one thermocouple monitoring the water temperature in cell 1, and another with one thermocouple for each electrochemical cell (as shown in Figure 61). Each of the prototypes underwent the validation tests presented in Chapter 3.3.5. After passing these tests, they were subjected to experiments where the potentials of each cell and the temperatures readings from each of the inserted thermocouples were monitored. Initially, the electrolyzer was only subjected to water supply at 60 °C, and then an injection of 8,6A was added to simulate the normal operation.

Table 15 - Summary of the Prototypes done using the Flow-Field Hole instrumentation.

Prototype number	Observation
1	One sensor positioned at Cell 1
2	One sensor for each electrochemical Cell*

* - Cell 2 experienced a cut in one of the thermocouple wires, and as a result, there is no data for this cell

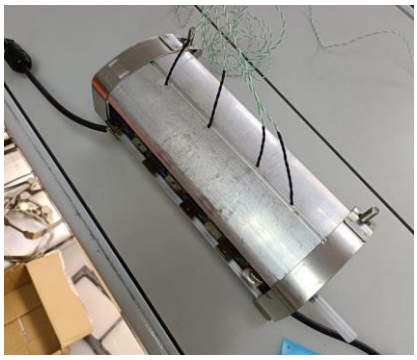

Figure 61 - Prototype 2 (one thermocouple for each electrochemical cell)

In the first prototype, it was possible to close the electrolyzer using four clamps, ensuring that the electrolyzer is compressed normally. Figure 62 represents the four clamps and the positioning of the thermocouple in the first prototype.

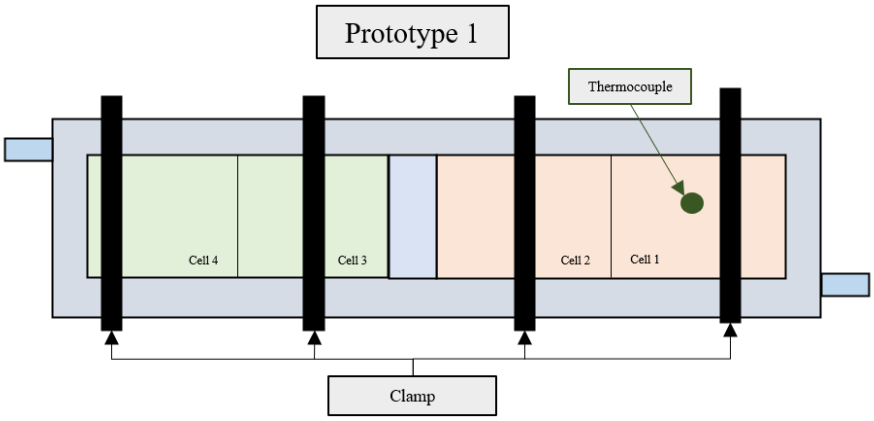

Figure 62 - Schematic about the instrumentation of the prototype 1

In the second prototype, it was only possible to close the electrolyzer using two clamps due to the particularity of the instrumentation and the inability to use all four clamps, utilized in a standard electrolyzer. Figure 63 shows the two clamps and the positioning of the four thermocouples in the second prototype.

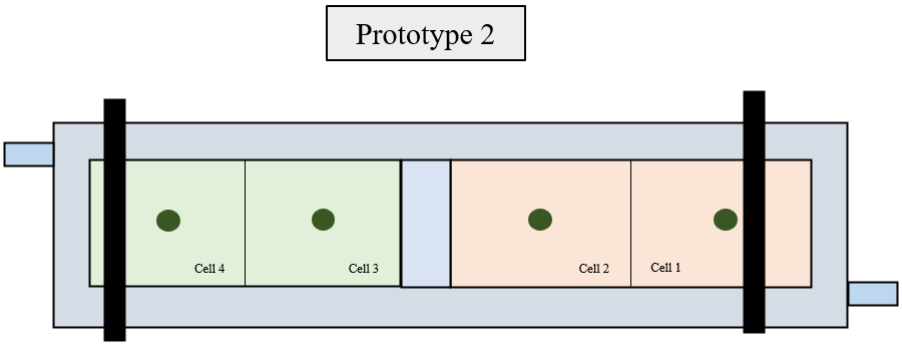

Figure 63 - Schematic about the instrumentation of the prototype 2

4.4.3. Results and Discussion

In this subsection, the results obtained in the two created prototypes will be analyzed.

a) Cells Potential

Figure 64 represents three graphics that shows the potential evolution over 10 minutes of operation at 8.6A for a standard electrolyzer, the 1st Prototype, and the 2nd Prototype. These results suggest that this type of instrumentation significantly impacted the electrolyzer's performance.

The 1st Prototype, with only one thermocouple in cell 1, allowed for the typical compression achieved during electrolyzer assembly, using four clamps (shown in the Figure 62). Consequently, the potential results are closer to the standard performance, suggesting that this type of instrumentation moderately affect the normal operation. The differences observed are explained by the components of the electrolyzer lifetime distinctions.

However, it is crucial to note that the 2nd Prototype was not adequately compressed during assembly due to the constraints of the instrumentation, using only two clamps instead of four (shown in the Figure 63). This explains the presented results and raises doubts about the readings of each thermocouple since the electrolyzer is not operating under normal conditions. A potential improvement of this instrumentation would involve finding a solution for better compression of the electrolyzer, a task that can be addressed.

Despite these results lacking some confidence in thermocouple readings, they were analyzed because this instrumentation ensures that the components are compressed in the same manner. This enables drawing conclusions based on the acquired temperature probe results.

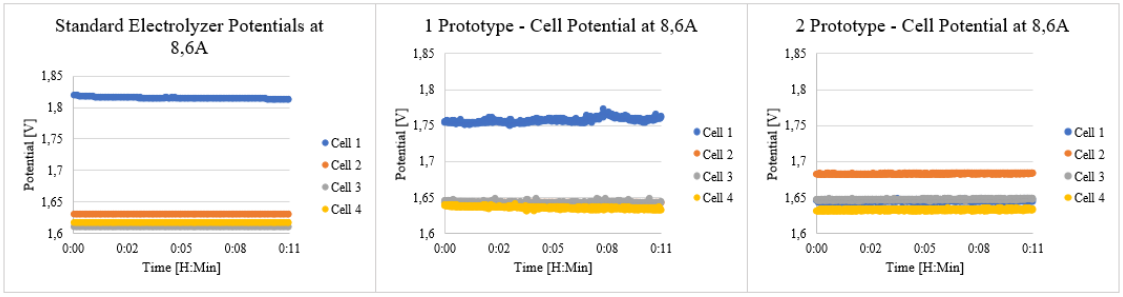

Figure 64 - Comparison between potentials of a standard electrolyzer and the prototypes

b) Temperature Probes

Figure 65 shows the analysis of thermocouple readings when no current is injected, and temperature water supply of 60°C. Firstly, it is noticeable that the thermocouples placed in the external circuit (inlet and outlet of the anode and cathode) indicate the same values both experiences, which validates the comparison made.

The first prototype exhibits highly realistic results, with cell 1 showing a temperature below the electrolyzer's inlet temperature. Furthermore, it demonstrates remarkable stability without any fluctuations, confirming the precise positioning of the thermocouple.

In the second prototype, there is some fluctuation observed in cells 1, 3 and 4, with cell 4 being the most stable. All four cells register values within the inlet and outlet temperature range of the anode, which is generally acceptable, except for the observed fluctuations. These fluctuations may be attributed to suboptimal component compression due to the assembly methodology employed.

The cell 4 exhibits temperature values very similar to the cell 1, which can be explained by the results obtained in the CFD simulation chapter. In that chapter, it was demonstrated that these two cells are supplied with a higher flow rate than the others. This difference in flow rate could lead to a temperature imbalance. Further prototypes and a resolution to the compression issue of the electrolyzer are necessary to provide a

more comprehensive and confident analysis of the data obtained through this type of instrumentation.

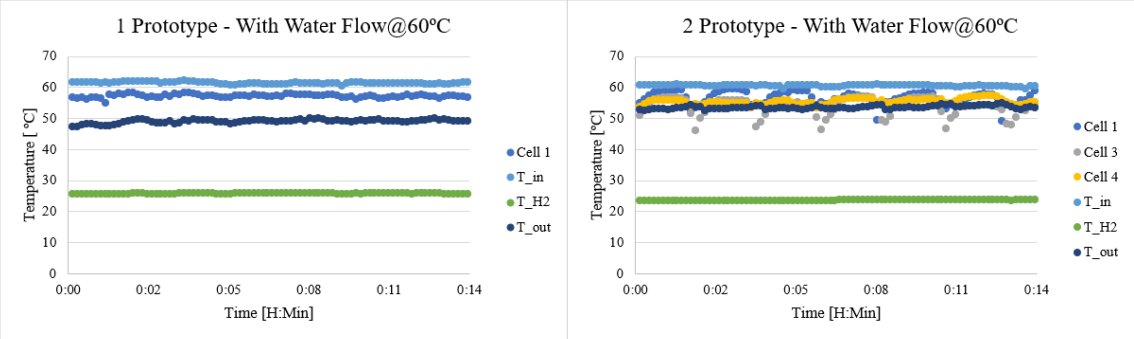

Figure 65 - Temperature probe results for each prototype

In the Figure 66, the readings of the thermocouples were analyzed while the electrolyzer was operating with a stable current of 8.6A. Comparing the values from the external circuit of both experiments, it is noticeable that in the second prototype, the outlet temperatures of the anode and cathode are slightly lower than those in the first prototype. This difference can be attributed to variations in the compression and, consequently, discrepancies in the operation of the electrolyzer.

Regarding the temperature results within the cells, the first prototype showed the temperature in cell 1 very close to the inlet temperature of the electrolyzer. In the second prototype, the cell temperatures stabilized due to the electrochemical reaction and the increased uniformity of the water during the formation of the biphasic fluid (water + oxygen). The values fall within the range between the inlet and outlet of the electrolyzer, demonstrating an average temperature difference of 4 degrees between cell 1 and cell 4. Further prototypes are required to validate these results more comprehensively, but there is evidence that the cell 1 experience higher temperatures that the other electrochemical cells.

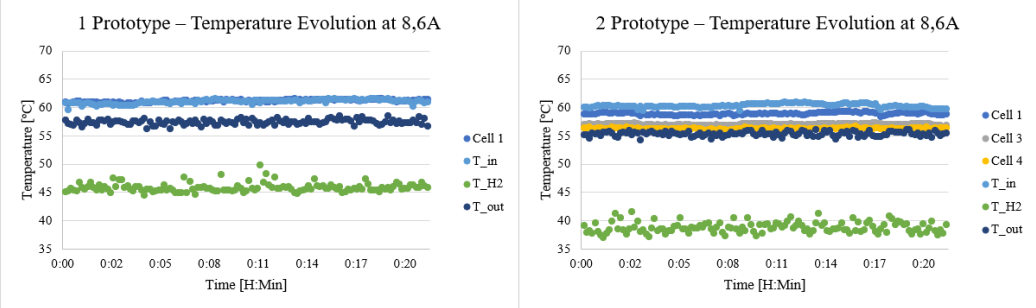

Figure 66 - Temperature probe results each prototype at 8,6A and water supply at 60 ºC

4.5. Conclusions on Temperature Instrumentation

Two different methods for in-situ instrumentation using thermocouples to analyze the temperature distribution within the anodic Flow-Field of the electrolyzer have been demonstrated.

Instrumentation utilizing the interstice of the UPP does not yield optimal results due to the issue of wire thickness influence on the compression of the electrolyzer. This type of instrumentation showed that temperatures either too high or too low were recorded in cell 1, likely influenced by the electrolyzer compression with this type of instrumentation. Therefore, it is concluded that this type of instrumentation is not the most suitable for the proposed objectives and raises significant doubts regarding the obtained readings.

Although it was not possible to achieve identical potential values in each cell, prototypes created using holes in the flow-field provided more reliable results. It is essential to produce additional prototypes to validate and improve the methodologies, especially regarding assembly to achieve an ideal compression of the electrolyzer. Enhancing this type of instrumentation will offer numerous benefits for a better understanding of this component. In the prototypes tested, it was possible to measure temperatures within the range of water inlet and outlet temperatures of the electrolyzer, despite the compression levels not aligning with the standard.

Therefore, the next steps would involve improving the methodology and finding a reliable compression method to avoid compression differences. It is also necessary to create more prototypes to validate the obtained data. However, through this work, it was possible to demonstrate that understanding temperature profiles within the electrolyzer is achievable, and this is a path to follow for further improving and gaining a better understanding of what is happening in the anodic flow field of the electrolyzer.

5. CFD

5.1. Introduction

In this chapter, the main objective is to characterize the water flow in the flow-field of the anode chamber. As explained in Chapter 2 the flow-field has a crucial importance in the overall performance of the electrolyzer. It is responsible to guarantee a uniform distribution of water to reach each electrochemical cell and allow the removal of the excess liquid water and gaseous oxygen (two-phase fluid) outside the electrolyzer. The flow analysis will allow to evaluate the current design and explore improvements opportunities to increase the overall performance of the electrolyzer.

Firstly, a simulation will be carried out to study the water flow distribution inside the chamber 2 – symmetric of the flow-field, represented in green in Figure 67, under normal operating conditions - laminar flow. Secondly, the same conditions will be used for the simulation of the chamber 1 - asymmetric, represented in the orange box in the same figure. Then, a simulation on the entire flow-field will be carried out (chamber 1 and chamber 2) with normal working conditions – laminar flow. Under normal operating conditions, in a laminar flow regime, the electrolyzer has an inlet flow rate of 20 mL/min, which is assured by the water supply system.

To finalize, the entire flow-field component will be tested at higher working conditions under laminar regime to predict the water mass flow distribution resulting from an increase in inlet water velocity. In summary, this simulation aims to forecast the electrolyzer's performance with an increased water supply, observing differences from the standard water mass flow distribution.

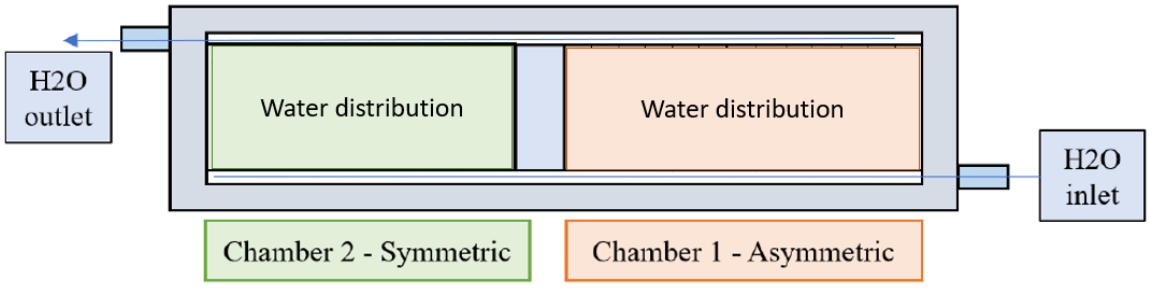

Figure 67 – Schematic about the two chambers at the anode of the electrolyzer

Multiple simulations were conducted to gain confidence in the model and evaluate the best properties to use in the simulations performed. In summary, four different simulations were performed. Table 16 summarizes all the simulations performed, knowing that numerous different configurations were tested throughout the experiments.

Table 16 - Summary of the valid simulations done.

Simulation	Type of Flow
Chamber 2 – Symmetric	Laminar (standard condition)
Chamber 1 – Asymmetric	
Chamber 1 + Chamber 2 - Together	
Chamber 1 + Chamber 2 - Together	Laminar (extreme condition)

To simplify the identification of each channel in the electrochemical cells, we chose to number them from the channel closest to the inlet (number 1) to the one closest to the outlet. Therefore, the numbering follows this logic for each simulated component.

In the model with the entire flow-field, chamber 1 (asymmetric) is the first component to receive the inlet water, and therefore, the numbering of each cell corresponds to the channels, as depicted in Table 17.

Table 17 – Channel numbering of each electrochemical cell of the entire Flow-Field component

	Channel number each electrochemical cell of the entire flow-field			
Electrochemical Cell	**Cell 1**	**Cell 2**	**Cell 3**	**Cell 4**
Channel	1 to 7	8 to 13	14 to 19	20 to 25

5.2. Models Equations and Simulation Methodologies

As previously mentioned, the aim is to simulate and gain a better understanding of the water flow distribution in the anodic chamber. In this chapter, we will describe the simulation processes, including the models employed and the boundary conditions imposed throughout all the conducted simulations.

5.2.1. Simulation Process

The CFD simulations involved the steps outlined and the software used:

- Solid Modeling – *Siemens Solid Edg*e

- Mesh generation – *Ansys Fluent Meshing*
- Boundary Conditions – *Ansys Fluent Meshing*
- Flow Simulation – *Ansys Fluent*
- Post Processing – *Ansys Fluent*

5.2.2. Fluid Flow model equations

Navier Stokes Equations

In this subsection, we will present the equations employed during the simulation. To simulate fluid flows, the Navier-Stokes equations were utilized, without the need for the energy conservation equation, as the conducted simulations are isothermal and incompressible.

The Navier-Stokes equations are fundamental equations in fluid dynamics that describe the motion of fluids. These equations play a pivotal role in understanding fluid behavior and have wide-ranging applications in various engineering applications. They consist of three equations: the continuity equation (1), the momentum equation (2), and the energy equation [18]. When solved together, they provide a comprehensive description of fluid behavior, including velocity, pressure, density, and temperature, in both incompressible and compressible flows. The energy equation will not be expressed once all the CFD simulation done were isothermal, without energy analysis.

1. **Continuity Equation (Mass Conservation)** [18]**:**

$$\nabla . \boldsymbol{u} = 0$$

- $\boldsymbol{u}$ is the velocity vector.
- ∇ is the nabla operator.

For incompressible flow the continuity equation states that divergence of the mass flux is conserved. In simpler terms, it enforces the conservation of mass within the fluid, indicating that mass cannot be created or destroyed, only redistributed through the flow.

2. **Momentum Equation (Conservation of Momentum)** [18]**:**

$$\rho(\frac{\boldsymbol{\partial u}}{\boldsymbol{\partial t}} + \nabla . (\boldsymbol{u} \otimes \boldsymbol{u}) = -\nabla p + \nabla . \tau$$

- ρ is the fluid density.
- $\boldsymbol{u}$ is the velocity vector.
- p is the pressure.
- τ is the deviatoric stress tensor (order 2)
- ∇ is the nabla operator.

The momentum equation represents Newton's second law for fluids. It describes how the velocity of fluid particles changes over time due to various forces. These forces include pressure gradients ($-\nabla p$) and viscous effects ($\nabla . \tau$). The convective term ($\nabla . (\boldsymbol{u} \otimes \boldsymbol{u})$) accounts for the advection of momentum by the fluid flow itself.

In the simulations conducted, it was determined that the fluid is incompressible due to the low flow rates of the electrolyzer operation. As a result, the equations are relatively simpler because the density does not vary throughout the flow. The effect of gravity was neglected since the geometry has a low height and does not influence the obtained results. Consequently, Navier-Stokes equation were simplified.

5.3. Solid Modeling

The software used was *Siemens SolidEdge* and it was necessary to treat properly the components to eliminate some features without interest for the CFD simulation to simplify the solid model without compromising the accuracy of the simulation's realism.

After that, the solid model was imported (.igs file) to the *Ansys SpaceClaim* and it was necessary to perform a procedure in each component, once the import process is not a direct operation. Then the negative volume of the geometry was taken, as shown in Figure 68. Only the fluid domain was used in all simulations since the primary goal is to assess and understand water distribution within the various channels of different components.

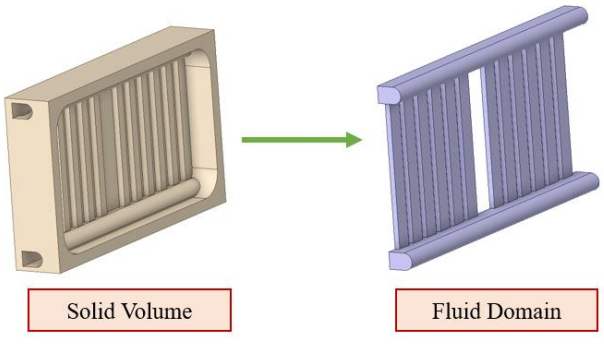

Figure 68 –Fluid domain in the chamber 2 (symmetric) component.

After the creation of the fluid domain, it was necessary to create planes to facilitate the pos-process analysis. A control area was created in the middle of each channel of the flow-field component, following an original procedure on *Ansys SpaceClaim*, as shown in the Figure 69 for the symmetric component.

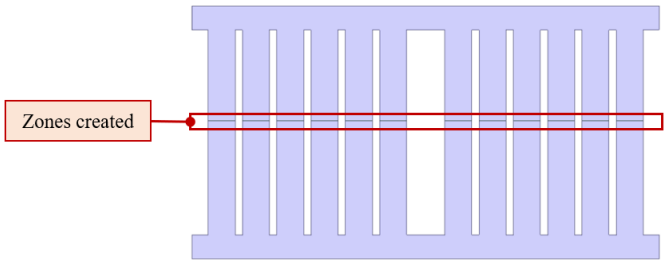

Figure 69 - Zones created in the chamber 2 - Symmetric.

Then it was necessary to create named groups to the area that corresponds to the inlet, outlet, the walls, and the surfaces created, explained in the next subchapter.

5.4. Boundary Conditions

To describe all the imposed conditions, we will provide an example for the simulation conducted in chamber 2 - symmetric of the flow-field. The same types of properties were considered for the rest of the simulations, with the model utilizing the complete flow-field involving both chambers in series.

In Figure 70, it is possible to observe the inlet channel, the outflow channel for water flow, as well as the walls imposed in the geometry. The surfaces have been numbered from 1 to 12, starting from the closest to the inlet and proceeding towards the outlet. This method of numbering scheme was maintained for all the channels in the simulations.

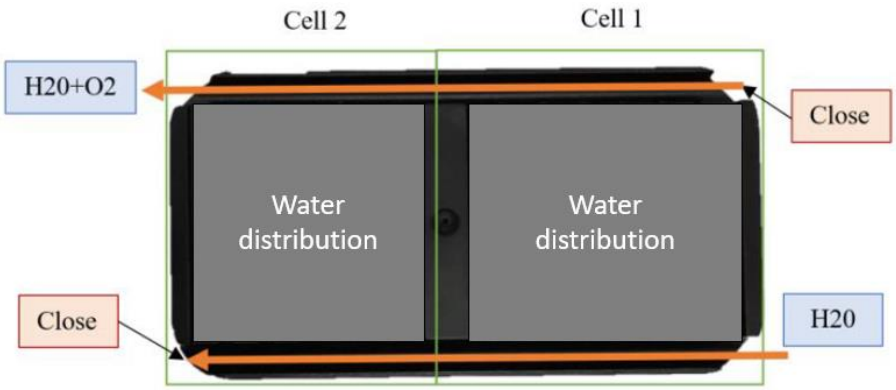

Figure 70 - Boundary conditions defined in the chamber 2.

A mass flow rate was defined for the inlet in each of the simulations, along with an outlet pressure that correspond to the environment pressure, shown in the Table 14. The calculations for the inlet mass flow rate are explained in subchapter 5.5.

Table 18 - Inlet and outlet properties for each simulation

Type of Flow	**Simulation**	**Mass Flow Inlet** $[g/s]$	**Pressure Outlet** $[Pa]$
Laminar (standard)	Chamber 1	0,3322	0
	Chamber 2		
	Entire Flow-Field		
Laminar	Entire Flow-Field	3,985	

5.5. Dimensionless numbers

In this subsection, we will present the dimensionless numbers considered during the simulation process: Reynolds number and the y+ number and the calculations performed for the various simulations conducted.

Reynolds Number (Re)

The Reynolds number is a dimensionless parameter employed in fluid mechanics to predict the flow characteristics within a conduit like a pipe or channel. The Re measure the ration between inertial and viscous forces as is defined as [19]:

$$Re = \frac{\rho u L}{\mu} = \frac{u D_{eq}}{v} \tag{18}$$

Where:

- ρ is the density of the fluid $[kg/m^3]$
- u is the speed of the flow $[m/s]$
- D_{eq} is the characteristic length $[m]$
- v is the kinematic viscosity of the fluid $[m^2/s]$
- μ is the dynamic viscosity of the fluid $[kg/(m \cdot s)]$

Typically, these are the range of Reynolds Number for the different flow regimes [20]:

- < 2000 – Laminar Flow
- $2000 < 4000$ – Transition Flow
- > 4000 – Turbulent Flow

In the simulation was calculated the Reynolds number from the normal operating conditions to assess the nature of the flow under consideration. It is important to highlight that within the flow-field, there are two channels with different dimensions: the common channel and each of the channels that encompass the electrochemical cell.

Table 19 summarizes the known and obtained parameters for calculating the Reynolds number in the two types of channels with different dimensions that we have in chamber 2 of the flow-field. The yellow boxes are values that are known: flow rate is the operating water inlet, and the dimensions are taken from the *SolidEdge* model. The green boxes are values calculated using the equations below. It was defined that the water temperature is 300K to take the dynamic viscosity and density of the water. To calculate the velocity, the equation was followed:

$$Q = A.v \tag{19}$$

The equivalent diameter given the design D_{eq} is given by:

$$D_{eq} = 4 \times \frac{A}{P} \tag{20}$$

Table 19 - Summary about the Reynolds Number calculation of the laminar simulations

	Flow Rate $[mL/min]$	**Area** $[mm^2]$	**Perimeter** $[mm]$	**Velocity** $[m/s]$	D_{eq} $[m]$	**Reynolds Number**
Common Channel	20	22,28	18,28	0,01496	4,87	85
Channel 1-12	$\frac{20}{12} \cong 1{,}67$	4,55	10,55	0,00611	1,725	13

The Reynolds numbers in both cases are very low, confirming that the flow regime is laminar.

In the simulations involving higher inlet water, a different approach was taken. An inlet Reynolds Number of 1018 was defined for the entry of the flow-field, and the corresponding mass flow rate to satisfy this condition was determined. Therefore, the calculations are summarized in Table 20, using the same equations as previously shown, with the water temperature set at 300K. The mass rate was calculated using the equation:

$$\dot{m} = Q \times \rho = A \times v \times \rho \quad (21)$$

Table 20 - Summary about the mass flow rate calculation of the Re = 1018 simulation

	Mass flow rate [g/s]	**Area $[mm^2]$**	**Perimeter $[mm]$**	**Velocity $[m/s]$**	**D_{eq} $[mm]$**	**Reynolds Number**
Common Channel	3,985	22,28	18,2832	0,1789	4,874	1018

The mass flow rate of 3,985 g/s was defined in the Ansys Fluent.

5.6. Mesh generation

The mesh was generated using the software *Ansys Fluent Meshing*. In every simulation it was used polyhedral type of cells. The properties of every simulation are in the following tables. The conditions were taken in account the Ansys Fluent User' Guide 12.0 [21].

The student version of Ansys has a maximum limit of 512k cells. Therefore, it was decided to set a maximum of 256k cells for each individual chamber simulation, and then the simulations with the entire flow field would have approximately 512k cells. A transition boundary layer with a set of 3 layers was also chosen to improve the results close to the geometries boundaries, the definitions are represented in the Table 21. The mesh created to the entire flow-field simulations were the same in both laminar analyses, represented in the Table 24. In Figure 71 shows an example of the mesh created in the chamber 2, using a cut in the plane XOY in a section of this component where it is possible to observe the three boundary layers created in the sections of the component.

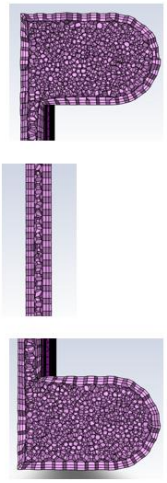

Figure 71 - Plane XOY of the mesh generated in the chamber 2.

Table 21 - Properties of the near wall region

Mesh parameter	Definition	Condition
Type	Smooth transition	-
Number of Layers	3	-
Transition ratio	0,272	-
Growth Rate	1,2	-

Table 22 - Mesh proprieties of the chamber 2 (symmetric) of Flow-Field simulation

Surface Diagnostics	Value	Condition
Total number of faces	41243	-
Maximum skewness	0,5863	< 0,89
Maximum aspect ratio	19,96	-
Volume Diagnostics	**Value**	**Condition**
Number of cells	252966	<256.000
Minimum orthogonal quality	0,2	>0,1
Maximum aspect ratio	17,97	<60

Table 23 - Mesh proprieties of the chamber 1 (asymmetric) of Flow-Field simulation

Surface Diagnostics	Value	Condition
Total number of faces	44361	-
Maximum skewness	0,5914	< 0,89
Maximum aspect ratio	19,58	< 35
Volume Diagnostics	**Value**	**Condition**
Number of cells	274214	<256.000
Minimum orthogonal quality	0,2005	>0,1
Maximum aspect ratio	22,28	<35

Table 24 - Mesh proprieties of the entire Flow-Field simulation

Surface Diagnostics	Value	Condition
Total number of faces	82553	-
Maximum skewness	0,5901	< 0,89
Maximum aspect ratio	19,92	-
Volume Diagnostics	**Value**	**Condition**
Number of cells	502367	<512000
Minimum orthogonal quality	0,2001	>0,1
Maximum aspect ratio	27,92	<35

5.7. Post-Processing

To assess the inlet and outlet pressure in each of the component's channels, control points were created to measure these values. In Figure 72 are shown the created points, as well as the previously established mid-surfaces of the chamber 2. Through this preprocessing step before running the simulation, we ensured that it was feasible to obtain the pressure values (absolute, dynamic, and total) at each of the control points. This process was applied to every modeled component (chamber 1, chamber 2 and in the entire flow-field) and it was necessary to discover and calculate the coordinate of each point to guarantee that are in the same relative position in relation to the channel.

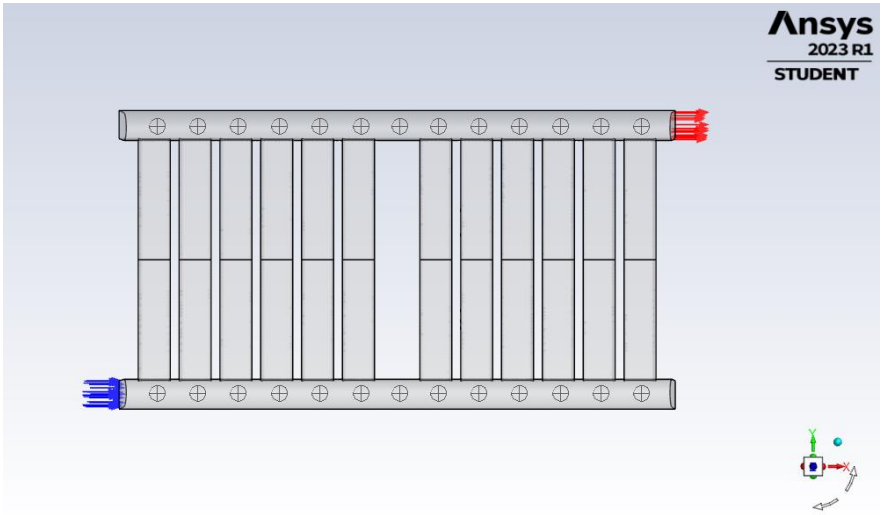

Figure 72 - Points created to obtain pressure values in the inlet and outlet of each channel in the chamber 2.

5.8. Numerical aspects

A hybrid initialization approach was chosen, involving 15 iterations to start the equations convergence. The simulations were set to run for 500 iterations, with no constraints imposed on convergence parameters. The values of the continuity equation residuals were less that 1×10^{-7} in every simulation showed in this report, so the simulation converged.

5.9. Results and discussion

This chapter is structured to present the results obtained from the simulations and discuss them. The mass flow rate distribution and the pressure distribution will be studied for each component under laminar flow conditions and then the entire flow-field under higher inlet water velocity at the laminar regime. The statistics used in the analysis are listed and explained in **Annex 4**.

5.9.1. Mass Flow Rate Analysis

In this subchapter, the mass flow rate results for each of component simulated will be analyzed and a comparison between them will be made.

a) Standard Laminar Flow

Chamber 2 – Symmetric

Figure 73 illustrates the mass flow distribution with an inlet flow rate of 20 mL/min. The component has an average flow rate of 27.32 mg/s on each channel, represented by the black dash line, with slight mass flow rates variations among channels. The channel 1 has the highest flow rate: 31.17 mg/s, while channel 9 has the lowest one: 25.91 mg/s. So, the channels closest to the inlet of the chamber 2 seem to have a slightly higher mass flow rate than the channels closest to the outlet. It is possible to observe that the first cell, corresponding to channels 1 to 6, has a slightly higher average flow rate than the second cell represented by channels 7 to 12. This difference is not significant, as indicated by a relative standard deviation of 5.61%, as shown in Table 25.

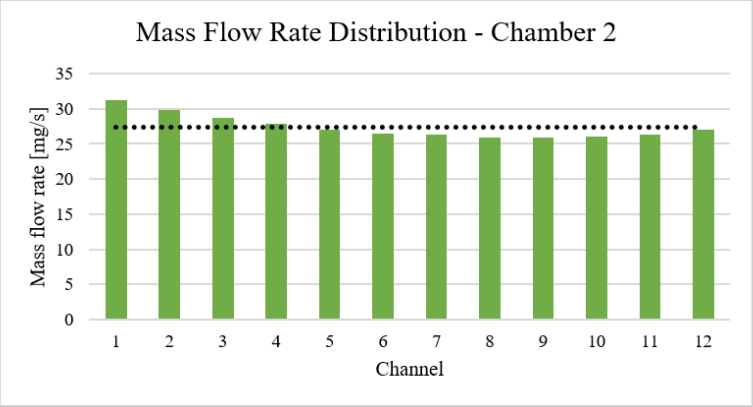

Figure 73 - Mass flow rate distribution in the chamber 2

Table 25 - Average and relative standard deviation of the mass flow distribution of chamber 2

Average	Relative Standard Deviation
27,39 mg/s	5,61 %

Chamber 1 – Asymmetric

In this component, as shown in Figure 74, it is evident that the channel with the highest mass flow rate is the one closest to the outlet, which is the channel 13 with a value of 29.6 mg/s. The channel with the lowest mass flow rate is the channel 5, where the value is 23.99 mg/s. These results contrast with the trend observed in chamber 2, where the closest cell had a higher average mass flow rate. In contrast, in this simulation, the cell closest to the outlet has higher values. This demonstrates that the component's lack of symmetry significantly influences the water flow behavior. Additionally, since this chamber has an extra channel, it would be expected a lower average mass flow rate, as demonstrated. However, the relative standard deviation increased (5.61% to 6.96%), indicating that the differences between channels increased significantly with this variation.

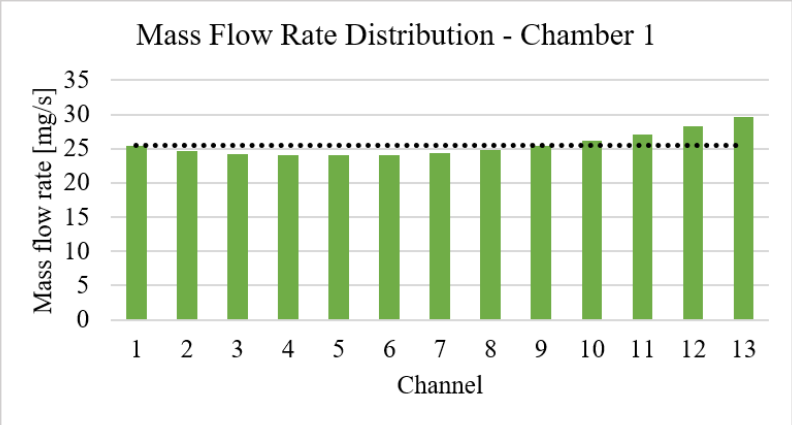

Figure 74 - Mass flow rate distribution in the chamber 1

Table 26 - Average and relative standard deviation of the mass flow distribution of chamber 1

Average	Relative Standard Deviation
25,55 mg/s	6,97 %

Entire Flow-Field Component

For the case of the entire flow-field, the distribution of mass flow rates for the channels in this component can be observed in Figure 75, along with an average mass flow rate of 13.23 mg/s. The channel with the highest mass flow rate is the channel 25 (closest to the electrolyzer outlet) with 19 mg/s, while the channel with the lowest flow rate is the channel 12 (corresponding to cell 2 of the electrolyzer) with a flow rate of 10.97 mg/s. The difference between the maximum and minimum channels is significant, resulting in a relative standard deviation of 17% compared to the average flow rate (presented in the Table 27). As shown in Table 28, there is a greater difference between the highest and lowest channels in electrochemical cell 1 and cell 4. This observation highlights a flawed distribution of channels within the electrochemical cell and variations in flow between electrochemical cells.

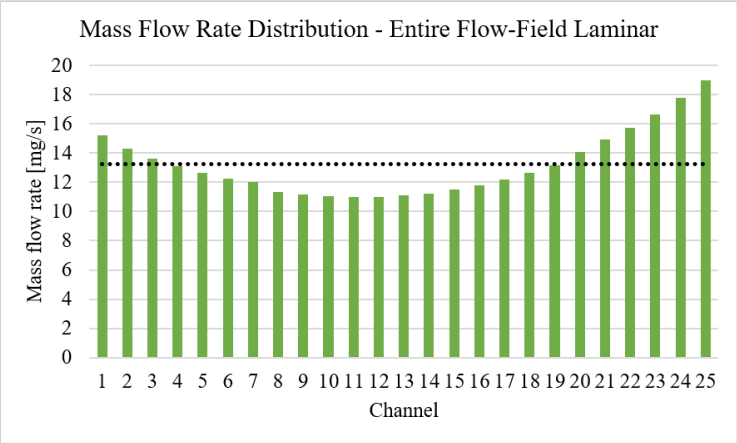

Figure 75 - Mass flow rate distribution in the entire Flow-Field (laminar flow)

Table 27 - Average and relative standard deviation of the mass flow distribution of entire Flow Field (laminar flow)

Average	Relative Standard Deviation
13,23 mg/s	17,01 %

Table 28 - Differences between maximum and minimum each cell (laminar flow)

Differences between the higher and lower Mass flow rate each electrochemical cell [mg/s]			
Cell 1 [1-7 channel]	Cell 2 [8-13 channel]	Cell 3 [14-19 channel]	Cell 4 [20-25 channel]
3,23	0,41	1,95	4,9

b) Laminar Flow (Re = 1018)

Figure 76 shows the water distribution in the entire flow-field with laminar conditions (Re = 1018), and there is a significant difference between channels, especially in the channels corresponding to the last electrochemical cell (closest to the electrolyzer outlet) that it is represented by the channels [20-25]. In these cells, it is evident that a much higher average flow rate passes through compared to the cells in chamber 1. The maximum flow rate corresponds to channel 25 with 422 mg/s, while the channel with the lowest flow rate is channel 8 with 79 mg/s, resulting in a considerable disparity between the highest and lowest channels. Represented in the Table 29, this simulation exhibits a relative standard deviation of 59,9%, confirming the poor distribution of this geometry under these more extreme laminar conditions.

This simulation highlights an inadequate water distribution, which could pose a problem when the electrolyzer is in operation and affect the performance of the electrochemical cells.

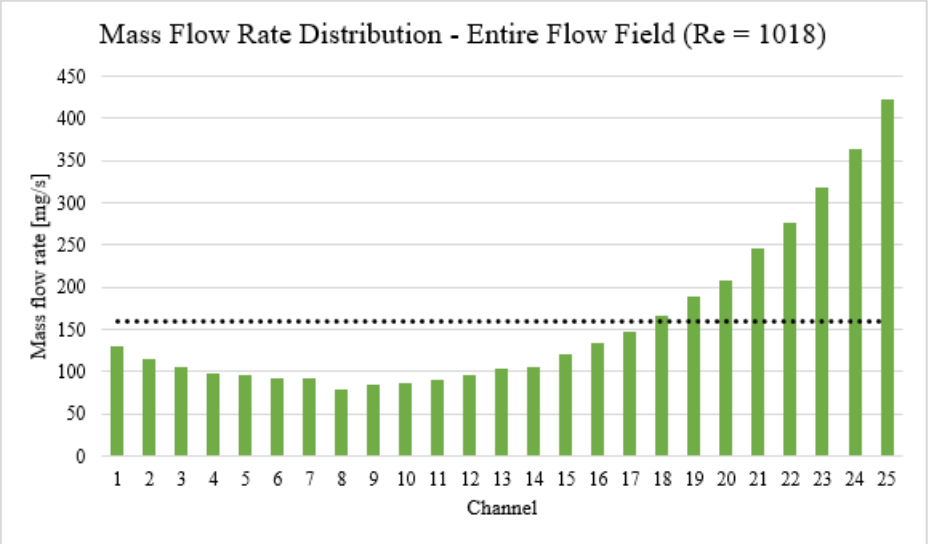

Figure 76 - Mass flow rate distribution in the entire Flow-Field (Re = 1018)

Table 29 - Average and relative standard deviation of the mass flow distribution of entire Flow Field (Re = 1018)

Average	Relative Standard Deviation
158,85 mg/s	59,95 %

5.9.2. Pressures Analysis

We analyze the pressure inside each chamber to characterize the flow according to the pressure read. It is important to mention that the total pressure at a point is determined by Bernoulli's equation, neglecting the component associated with altitude difference once the height of the component is negligible and in the $\rho g z$ formula the value is insignificant.

$$P_{total} = P_{static} + P_{dynamic} = P_{static} + \frac{1}{2}\rho v_{water}^2 \quad (22)$$

a) Laminar Flow

Chamber 2 - Symmetric

Initially, the influence of dynamic pressure in this flow regime was evaluated. As shown in Figure 77, there is evidence that the dynamic pressure generated by the fluid velocity has minimal impact on flow behavior, and the pressure distribution is mainly due to the geometry of the chamber. As the flow moves further from the inlet, it experiences higher pressures, reaching a maximum of approximately 2.5 Pa in the last channel near to the outlet. It is important to remember that each of these values was extracted from the plane corresponding to the middle of each channel, representing the average pressure of the created surface.

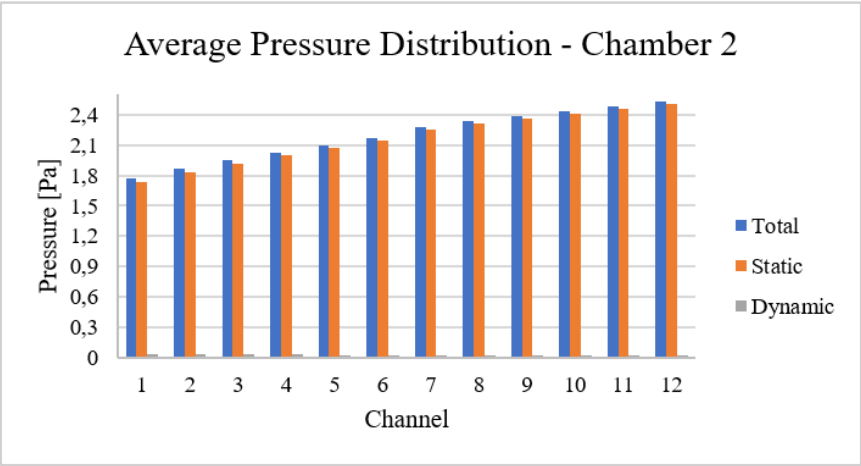

Figure 77 - Average pressure distribution of the middle of each channel of the chamber 2.

It is possible to obtain the total pressure values at the inlet and outlet for each of the channels through the created points. These points are shown in Figure 78, with point 6_7 specifically representing the transition point between the channels corresponding to cell 1 and cell 2.

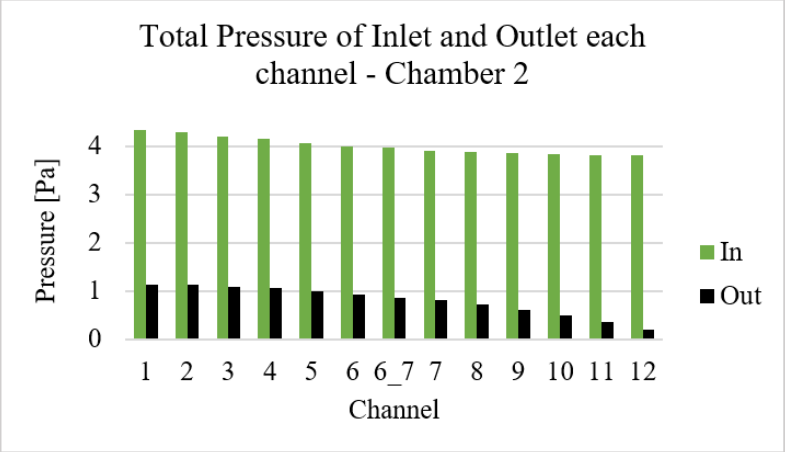

Figure 78 - Total pressure of inlet and outlet each channel of the chamber 2.

The difference between inlet and outlet of each channel correspond to the pressure drop caused by each of the channels individually, and it is presented in Figure 79. The difference between maximum and minimum value isn´t significant since channel 12 has a pressure range of 3.6 Pa, and channel 5 has 3 Pa. It exhibits a relative standard deviation of 5.23%, with an average pressure drop of 3.2 Pa in each of the channels. The pressure demonstrates be evenly distributed, with minimal variation among the channels.

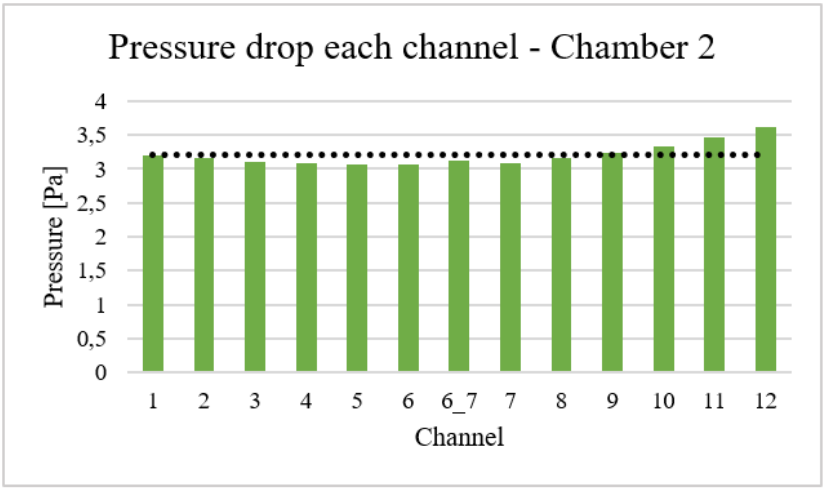

Figure 79 - Pressure drop each channel of the chamber 2.

Chamber 1 - Asymmetric

Figure 80 shows the inlet and outlet pressures of each channel in the chamber 1. It is evident that both the inlet and outlet pressures decrease as the flow approaches the electrolyzer outlet.

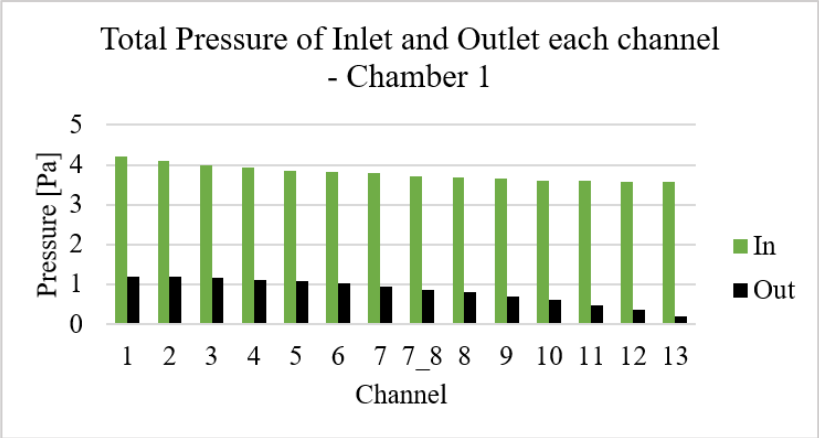

Figure 80 - Total pressure of inlet and outlet each channel of the chamber 1

The difference between inlet and outlet pressure of each channel is presented in Figure 81, showing an average total pressure loss of 2.96 Pa, slightly lower than in chamber 2 (as expected, once there is an additional channel). It exhibits a relative standard deviation of 5.9% in relation to the average pressure, indicating a slightly more spread-out distribution of pressure compared to the chamber 2. These results demonstrate that the component's geometry slightly affects the pressure distribution, although the difference is minimal.

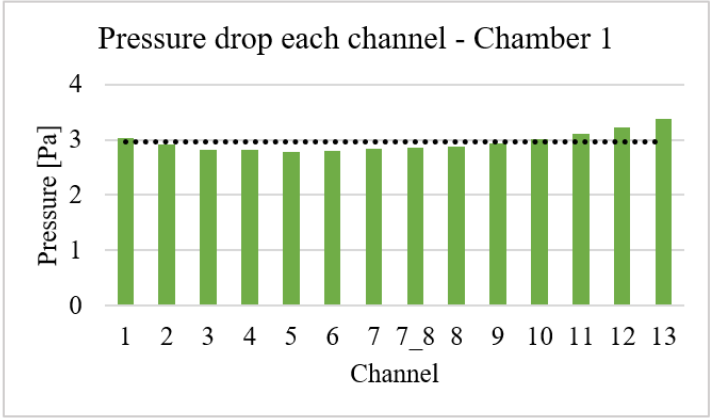

Figure 81 - Pressure drop each channel of the chamber 1.

Entire Flow-Field

Figure 82 illustrates the inlet and outlet pressures of each channel. Once again, the results follow the same pattern as in the other chambers, with a gradual decrease in total inlet and outlet pressures along the geometry until the electrolyzer outlet.

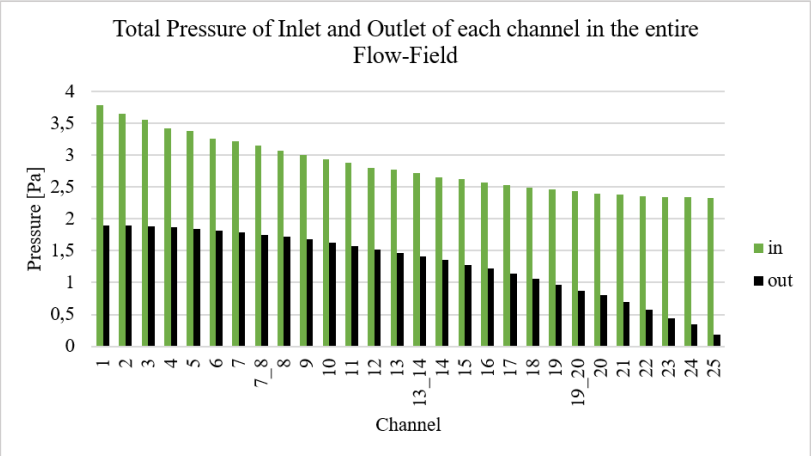

Figure 82 - Total pressure of inlet and outlet each channel of the entire Flow-Field (standard laminar)

The pressure difference between inlet and outlet is shown in Figure 83, where the average pressure loss in each channel is 1.53 Pa, with a relative standard deviation of 15.5% relative to the pressure average. The results indicate that the first and last electrochemical cells have pressure loss values with a significant range between the maximum and minimum range. The difference of the highest (channel 25) and lowest (channel 12) pressure drop value is approximately 0.85 Pa, showing that there is disparity once the goal is to guarantee an equal pressure drop in the entire flow-field.

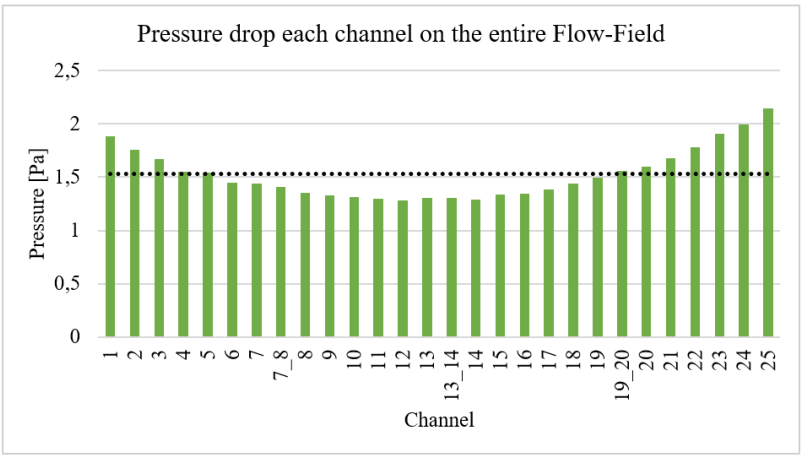

Figure 83 - Pressure drop each channel of the entire Flow-Field (standard laminar)

b) Laminar flow (Re = 1018)

Entire Flow-Field

In Figure 84 is presented the inlet and outlet pressure of each channel, in the laminar regime with water inlet Re of 1018. It is possible to observe that the pattern of pressure distribution seems to follow the pattern of the previous simulation.

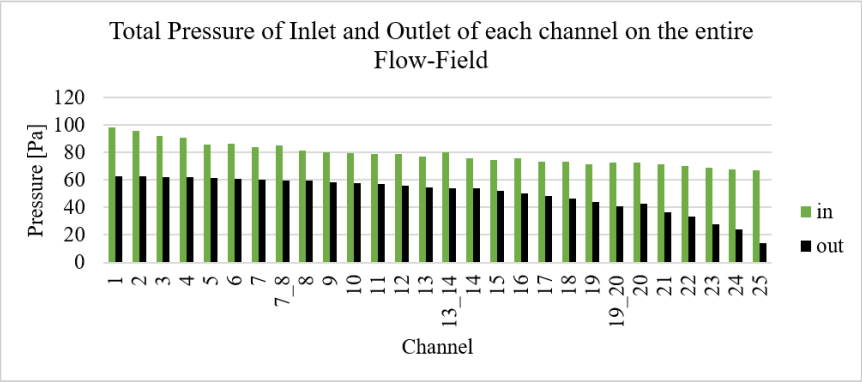

Figure 84 - Total pressure of inlet and outlet each channel of the entire Flow-Field (Re = 1018)

In Figure 85, it is possible visualize the representation of the pressure drop in each of the channels. The average pressure drop is approximately 28.84 Pa, and the results have a relative standard deviation of 15.6% from the average (very similar to the standard laminar regime). The difference between channels is very similar to the flow behavior in the standard laminar regime, which justifies that the type and velocity of the flow influence does not have a crucial impact in the flow behavior. The geometry of the component is the main responsible for the difference in inlet and outlet pressure in each channel.

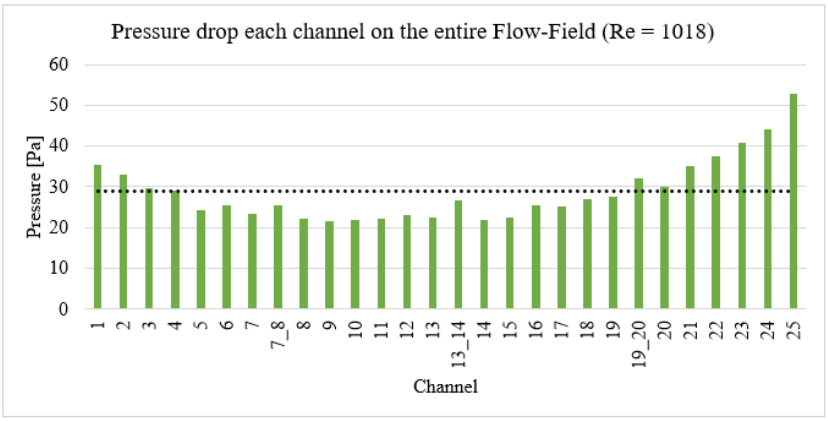

Figure 85 - Pressure drop each channel of the entire Flow-Field (Re = 1018)

5.10. Conclusions on CFD

Through these simulations, a general understanding of water flow distribution was achieved and serves as a starting point for a better understanding of this component, which is fundamental for the proper operation of the electrolyzer.

Firstly, when analyzing the entire flow-field in the standard laminar regime, it became evident that there is a heterogeneous distribution in this simulation that closely resembles the actual behavior of the electrolyzer when electrochemical reactions are not taking place, with a relative standard deviation of 17%. It was concluded from this simulation that improvements can be made in the design of the flow-field since it is demonstrated that cells 1 and 4 have a higher average flow rate than the others, and there are considerable differences between channels from the same electrochemical cell. Since the electrolyzer operates by applying the same electric current to each of the cells, assuming that conditions are equal in all four cells, this heterogeneous distribution can lead to different operation in each of them. Therefore, it would be interesting to test and evaluate different flow-field geometries to ensure better distribution in each cell. It was important to understand the distribution caused by each of the chambers individually to quantify the influence of the component's symmetry on water flow distribution. The simulation in higher Reynolds Number laminar regime indicates that there is a very significant variation between the channels of electrochemical cell 4, which can negatively influence the electrolyzer operation. The relative standard deviation of 60% indicates a highly heterogeneous distribution indicates the need for a more in-depth study of this component in relation to the production of the resulting two-phase fluid from water electrolysis.

For future work topics, it is recommended to continue the study to simulate the real operation of the flow-field and improve its design with alternative solutions. To achieve this, the variation in water temperature in the laminar regime can be evaluated to quantify the water temperature in each of the channels and, consequently, the electrochemical cell. This simulation will be of great interest since electrolyzer typically operates at temperatures around 60°C, and possibly exists variations in the water temperature during operation, which can influence water flow distribution, and potentially causing uneven distribution of the electrochemical cells. Another suggestion is to analyze the two-phase fluid formed in each of the electrochemical cells.

6. Conclusion

The global objectives of this work have been successfully achieved, as it has gathered numerous results that improve the understanding of the electrolyzer operation and, consequently, pinpoint areas for improving the performance.

The successful implementation of in-situ electrochemical instrumentation has demonstrated its potential for a detailed characterization of the electrochemical potentials within the electrolyzer. It was observed that the cathode chamber has a significant influence at high current levels, and it is responsible for the observed potential slope in the overall cell performance. As a future research topic, it is proposed extend the application of this instrumentation to other cells within the electrolyzer to facilitate result comparisons and uncover differences and their underlying causes. Ideally, having real-time visualization alongside the probes would be invaluable for capturing phenomena that may impact the electrolyzer performance.

The in-situ temperature sensor instrumentation provided a starting point for conducting such experiments, utilizing two different techniques to assess which one provided better results. The use of interstices in the UPP created an artefact during the electrolyzer normal operation, affecting the compression of the electrochemical core, as evidenced by the results obtained. Creating a hole in the flow-field allowed a better control of the compression issue and ensured more reliable results. Finding a way to compress the electrolyzer while accommodating the sensor insertions remains a challenge which can be overcome. In this type of instrumentation, only a few prototypes were created, and more would be needed to validate with more confidence the results obtained.

The CFD simulation of the anodic flow-field contributed to a better understanding of the water distribution in each of the electrochemical cells. It was concluded that the component's geometry significantly influences flow distribution, and there is room for improvement in the anodic flow-field geometry to achieve uniform distribution across all electrochemical cells. As a future research topic, I suggest conducting the same analysis on different geometry designs and, in a more advanced stage, examining the contribution of the two-phase fluid and influence of the temperature in the water distribution.

References

[1] L. Vidas and R. Castro, "Recent Developments on Hydrogen Production Technologies: State-of-the-Art Review with a Focus on Green-Electrolysis," MDPI, 2021.

[2] J. Chi and H. Yu, "Water electrolysis based on renewable energy for hydrogen production," Chin. J. Catal, 2018.

[3] Euro Parlament, 2023. [Online]. Available: https://www.europarl.europa.eu/news/en/headlines/society/20210512STO04004/renewable-hydrogen-what-are-the-benefits-for-the-eu. [Accessed 20 08 2023].

[4] C. M. Kalamaras and A. M. Efstathiou, "Hydrogen Production Technologies: Current State and Future Developments," in *Hindawi Publishing Corporation*, Nicosia, Cyprus.

[5] H. Souto and T. Nogueira, "O Hidrogénio como Vetor Energético do Futuro," Lisboa, 2015.

[6] S. H. Joo and B. Tansel, "Novel technologies for reverse osmosis concentrate treatment: A review," Journal of Environmental Management, USA, 2014.

[7] W. Xie, Y. Dai, R. Wang and K. Sumathy, "Concentrated solar energy applications using Fresnel lenses: A review," *Renewable and Sustainable Energy Reviews,* 2010.

[8] D. Bessarabov, H. Wang, H. Li and N. Zhao, PEM Electrolysis for Hydrogen Production: Principles and Applications, Taylor & Francis Group, LLC, 2016.

[9] A. Godula-Jopek, Hydrogen Production by Electrolysis, Wiley-VCH, 2010.

[10] Y. Naimi and A. Antar, Hydrogen Generation by Water Electrolysis, Morocco: IntechOpen, 2018.

[11] M. Chatenet, B. G. Pollet, D. R. Dekel, F. Dionigi, J. Deseure, P. Millet, R. D. Braatz and e. all, "Water electrolysis: from textbook knowledge to the latest scientific strategies and industrial developments," Royal Society of Chemistry, 2022.

[12] M. Carmo, D. L. Fritz, J. Mergel and D. Stolten, "A comprehensive review on PEM water electrolysis," International Jounal of Hydrogen Energy, Germany, 2013.

[13] V. S. Bagotsky, "Fundamentals of Electrochemistry," Wiley, Moscow, 2006.

[14] E. Brightman, J. Dodwell, N. v. Dijk and G. Hinds, "In situ characterisation of PEM water electrolysers using a novel reference electrode," Electrochemistry Communications, United Kingdom, 2015.

[15] L. V. Buhre, S. Bullerdiek, P. Trinke, B. Bensmann, A.-L. E. R. Deutsch, P. Behrens and R. Hanke-Rauschenbach, "Application and Analysis of a Salt Bridge Reference Ectrode Setup for PEM Water Electrolysis: Towards an Exted Voltage Loss Break Down," Journal of the Electrohemical Society, Hannover, Germany, 2022.

[16] Z. Kang, H. Wang, Y. Liu, J. Mo, M. Wang, J. Li and X. Tian, "Exploring and understanding the internal voltage losses through catalyst layers in proton exchange membrane water electrolysis devices," Applied Energy 317, China, 2022.

[17] H. Becker, L. Castanheira and G. Hinds, "Local measurement of current collector potential in a polymer electrolyte membrane water electrolyser," Journal of Power Sources, United Kingdom, 2019.

[18] G. Galdi, "An Introduction to the mathematical theory of the Navier-Stokes Equations," Springer, London, 2011.

[19] N.Rott, "Note on the history of the Reynolds Number," Annual Reviews, 1990.

[20] ANSYS, Inc., "Ansys Fluent Theory Guide," USA, 2021.

[21] Ansys, Inc, "Ansys Fluent Guide 12.0," 2023.

[22] V. S. Bagotsky, Fundamentals of Electrochemistry, Moscow, Russia: John Wiley & Sons, Inc., 2006.

[23] N. Perez, Electrochemistry and Corrosion Science, Puerto Rico: Springer, 2016.

[24] P. M. V. Raja and A. R. Barron, Physical Methods in Chemistry and Nano Science, Rice University: LibreTexts, 2023.

[25] J. Mo, "Fundamental Studies of Electrochemical Reactions and Microfluidics in Proton Exchange Membrane Electrolyzer Cells," *University of Tennessee, Knoxville*, 2016.

[26] T. Engel and P. Reid, Physical Chemistry, Pearson, 2013.

[27] J. Wu, "A Basic Guide to Thermocouple Measurements," *Texas Instrument*, 2023.

[28] Omega, [Online]. Available: https://www.omega.com/en-us/resources/how-thermocouples-work. [Accessed 2 9 2023].

[29] F. Menter, R. Lechner and A. Matyushenko, "Best Practice: Generalized k-omega (GEKO) Two-Equation Turbulence Modeling in Ansys CFD Version 1.01," Ansys, Inc., 2021.

Annex 1. Validation Data Acquisition

To validate the voltage's readings on the Kolibrik equipment, they were compared with the potentials measured in an operational electrolyzer under various injection currents using the Agilent 34970A. The following Figure illustrates the comparison conducted for one of the cells, with similar comparisons performed for the other cells. In the following table displays the absolute errors between the readings obtained from the Kolibrik and those obtained from the Agilent 34970A for each of the cells.

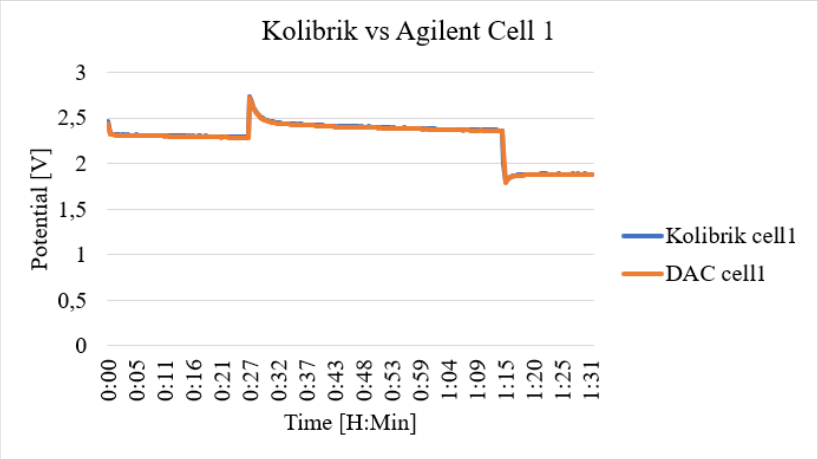

	Electrolyzer 1			
	Cell_1	Cell_2	Cell_3	Cell_4
Absolute Error [V]	0,0061	0,0001	-0,0002	0,0059

Annex 2. Electrochemical Chapter

The electrochemical phenomena and processes are useful for the quantitative and qualitative chemical analysis of various substances and media, including liquids, gases, and solids. The high accuracy of the electrochemical methods of analysis derives from the fact that they are based on highly exact laws (e.g., Faraday equations) [22]. In this annex will be presented the techniques used along the electrochemical experiments [23].

The hardware was connected to Bio-Logic software, EC-Lab

Three Electrode Systems

This setup is essential for conducting various electrochemical measurements, including cyclic voltammetry, impedance spectroscopy, and polarization curves applying the in-situ instrumentation. The three electrodes are:

- Working electrode is responsible for the electrochemical reaction of interest that is under experiment. It is the site where either oxidation or reduction occurs, depending on the experiment's requirements. The working electrode is connected to the Potentiostat and provides the measured current response.
- Counter electrode: has the main function of conduct the electric current flow to or from the working electrode (depends on the reduction or oxidation experiment definition).
- Reference electrode: it is essential for maintaining a stable and known electrode potential. It serves as a reference point against which the working electrode voltage is measured. The reference electrode used in the experiments was a standard hydrogen electrode that was properly calibrated.

All of them need to be submerged in an electrolyte solution during operation. The following image exemplify the three-electrode system [24]:

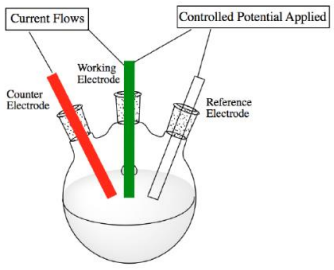

This system offers a precise control of electrochemical conditions. Applying a known potential between the working and reference electrodes allows the study of a substance's electrochemical behavior, current measurement, and analysis of properties. So, this three-electrode system was employed to obtain the electrochemical potential reading of the layer where the terminal of the electrochemical probe was inserted. The electrochemical probe, in turn, establishes an ionic connection with the layer under study and an electrolytic solution (H2SO4) containing the reference electrode. The experiments were done in the cell 1 of the electrolyzer, so the WE and CE from the Potentiostat were connected in the cathode and anode electrode of the electrochemical cell, considering the probe position. The following image shows the real three-electrode system configuration in the probe located in the anode chamber.

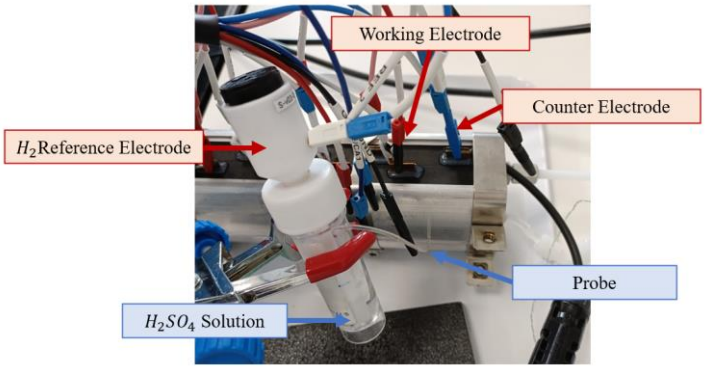

Polarization curve

Polarization curves are the relation of the cell voltage against the current density from the experiments [25]. In this test, using the Potentiostat, a current of 0,5A was initially imposed into the electrolyzer for 2 minutes, and the voltage in each of the cells was recorded, along with the reading from the electrochemical probe through the three-electrode system. Subsequently, the same data recording was performed, with current injection of 1A and so forth, incrementally up to 12A. This is a crucial test for comprehending the behavior of electrochemical cells and the probe at varying electric current values to which they may be subjected. These results provide a more detailed characterization of the electrolyzer normal operation, and the in-situ electrochemical probe yielded valuable insights into the potentials across each of the studied layers.

Cyclic Voltammetry

Cyclic voltammetry is a fundamental electrochemical method that, among its various applications, can be utilized to investigate the kinetics of oxidation-reduction reactions in electrochemical systems. Specifically, data collected with cyclic voltammetry can be used to determine the rate of reaction and this technique requires a three- electrode system using a reference and a Potentiostat [24].

The electrode potential is varied linearly with time and then the potential is changed in the opposite direction and returned to the initial value. As the potential is varied, the electrode current is measured. cyclic voltammetry provides a way to identify regions of potential in which significant amounts of charge are transferred to or from the electrode. These are the regions in which electrochemical reactions proceed [26].

Annex 3. Thermocouple Principles

Thermocouples function as temperature measurement sensors, generating a voltage that changes in response to temperature fluctuations. Consist of two wire leads composed of dissimilar metals, which are joined together to form a junction [27]. When the temperature fluctuates along the wire leads from the junction to the extremities, a potential is generated at the junction, called the seebeck voltage. By uniting dissimilar metals with distinct seebeck voltages at a temperature sensing junction, a thermocouple voltage is created, and this thermocouple junction can be exposed, grounded or ungrounded [27]. The following image exemplifies the working principle of a thermocouple [28]:

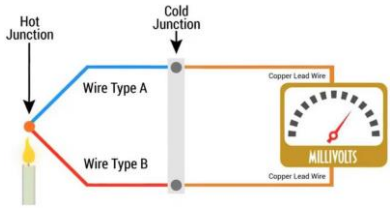

Mixing various metals results in a range of voltage responses, giving rise to various types of thermocouples tailored for specific temperature ranges and levels of precision. The following table shows the typical thermocouple type as the material of each metal [27]:

Thermocouple Type	Lead Metal A (+)	Lead Metal B (–)	Temperature Range (°C)
J	Iron	Constantan	–210 to 1200
K	Chromel	Alumel	–270 to 1370
T	Copper	Constantan	–200 to 400
E	Chromel	Constantan	–270 to 1000
S	Platinum and 10% Rhodium	Platinum	–50 to 1768

It was selected a type K thermocouple because it covers the temperature range intended for measurement, and the materials comprising the cables pose no risk of corrosion in any of the applications in which thermocouples were used.

Example of thermocouple used.

Annex 4. Statistics

To analyze the results obtained, it was essential to acquire some understanding of statistics. Formulas employed:

Standard Deviation

$$S_x = \sqrt{\frac{\sum_{i=1}^{n}(x_i - \bar{x})^2}{n-1}}$$

Where:

n – number of data points

x_i – each value

$\bar{x}$ – mean of x_i